ELSEVIER
SAUNDERS

Neurosurg Clin N Am 16 (2005) 1–64

NEUROSURGERY
CLINICS
OF NORTH AMERICA

Basic principles of magnetic resonance imaging

Wendell A. Gibby, MD

Riverwoods Imaging Center, 280 West Riverpark Drive, Provo, UT 84604, USA

The discovery of nuclear magnetic resonance (NMR) by Purcell et al [1] and Bloch et al [2] first revolutionized analytic chemistry and then medical imaging. NMR imaging has taken us to yet another dimension of diagnostic imaging in which superior contrast resolution; multiplanar capabilities; and imaging of physiologic processes, such as blood flow, perfusion, diffusion, cortical activation, metabolite concentrations, and motion, have provided an entire new world of insight into the nervous system. It is an ironic historical curiosity that the name NMR imaging was changed to MRI because of the public's perceived fear of nuclear devices, because MRI uses no ionizing radiation.

The fundamental interaction of atomic particles and radiofrequency (RF) energy allows us to create spectacular MRI scans on a routine basis. Through recent discoveries in physics, we know that one of the most fundamental particles in nature is the quark [3]. A basic property of subatomic particles is that they possess spin and angular momentum. Within the proton, there are two quarks that spin parallel to each other and a third that spins opposite, giving a net unopposed spin. We also know that a proton has a net +1 positive charge. A moving charge produces a magnetic field. In fact, magnetism is defined by the force created by a specific quantity of moving charge. A tiny magnetic dipole is then created. Not only protons but any atom that has an odd number of protons or neutrons has a net unbalanced nuclear spin, and thus a nuclear magnetic moment. Electrons also possess spin and charge, and thus have a magnetic dipole associated with them. Elements containing unpaired electrons, that is, those in which the electrons are not paired in outer orbitals and in which spins are not canceled, also have an effective magnetic moment. The magnetic moment associated with an electron is approximately 1000 times greater than that of a proton.

In this article, no attempt is made to define rigorously with mathematic techniques the interactions of the nuclei with each other and with external energy. Rather, an attempt to explain these concepts through the use of simple physical models that speak a universal language is made. Of course, no physical model is able to explain the nature of subatomic particles completely, just as no single mathematic equation currently explains the dual nature of matter. A number of earlier articles on the basics of MRI [4–10] are included within the references for the interested reader. I recognize that this article may go into far more detail than the typical reader requires. Nevertheless, for those few brave, intrepid, and curious souls who really wish to know what is going on in the mysterious insides of an MRI scanner, I have tried to make this model as complete as possible. Having a basic understanding of these principles allows one to optimize image quality, reduce error, and improve conspicuity of pathologic findings. A cookbook approach gives mediocrity at best.

We are all familiar with the property of a magnet, which when placed within a magnetic field, aligns itself in such a way that its interaction with the magnetic field creates the lowest steady-state energy. For example, a compass aligns its "positive" pole with the South Pole of the earth, with opposites attracting. A compass can have any orientation with respect to an external magnetic field, and with it, any energy of interaction from zero to the maximum. Things are not quite as simple at the atomic level. By quantum theory, only certain energy states are allowed, which are discrete in value. The hydrogen nucleus having a spin quantum number of positive $\frac{1}{2}$ and negative $\frac{1}{2}$ gives dipole vectors that point 35.26° with and

E-mail address: wgibby@novarad.net

1042-3680/05/$ - see front matter
doi:10.1016/j.nec.2004.08.017

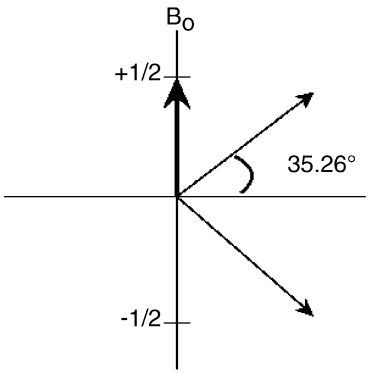

$$\text{Nuclear Moment} = \sqrt{(S+1)S} = \sqrt{(1/2+1)1/2} = \sqrt{3/4}$$

$$\sin\theta = \frac{y}{R} = \frac{1/2}{\sqrt{3/4}} = 35.26^\circ$$

Fig. 1. Hydrogen nucleus with spin quantum numbers of positive ½ and negative ½. The magnetic dipoles reside in energy states pointing with and against the magnetic field. The vectors pointing against the magnetic field are in a higher energy state.

against the magnetic field [5] as illustrated in Fig. 1.

Precession

When first placed in a magnetic field, the off-axis proton dipoles begin to precess at a rate known as the Larmour frequency. The often-used analogy of a spinning top precessing under the force of the earth's gravitational field is illustrated in Fig. 2. An important point to remember is that the motion of the precessing magnetic dipole and the motion of the atom are completely independent. The small spinning dipole within the nucleus maintains its orientation relative to the magnetic field in spite of rapid molecular tumbling and translational motion caused by thermal energy within the lattice of the molecular structures.

There are only two things that influence the precessional rate (angular velocity) of the spinning dipole. Each different element, be it a single proton, a nucleus composed of many protons and neutrons, or an electron, has a different angular momentum, and thus a different precessional rate

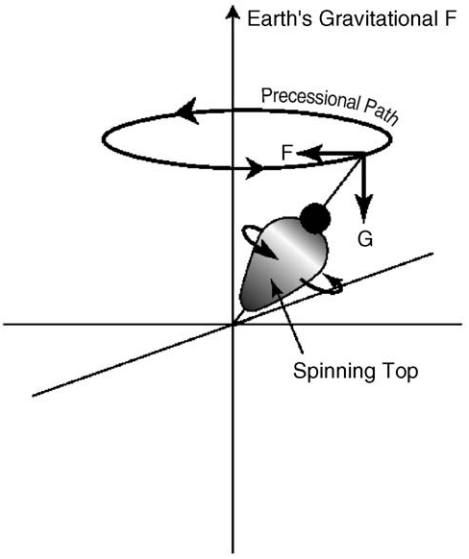

Fig. 2. A spinning top oriented off-axis with earth's gravitational field experiences two forces: the gravitational field, G, tending to pull the top toward the earth and an opposing centrifugal force, F, from the spin of the top. The result is a wobbling or precessional motion around earth's gravitational field. A similar motion occurs with spinning magnetic dipoles when placed within a magnetic field.

for a given magnetic field strength [5]. The precessional frequency of hydrogen in a magnetic field at 1.5 T is 63.866 MHz, whereas that for phosphorous is 25.876 MHz [11].

The second critical element in determining how fast a proton precesses is the net magnetic field that it experiences. A top that is precessing on the moon precesses at a different velocity than if it were spinning on the earth because of a difference in the gravitational force. Likewise, protons spinning in different magnetic field strengths precess at different velocities. This is given by the relation: Frequency = $\gamma \cdot \beta$, where γ equals the gyromagnetic ratio (for hydrogen, $\gamma = 2.6751978 \times 10^8 s{-}1T^{-1}$) and β equals the field strength in tesla [12]. Our model now describes an ensemble of precessing magnetic dipoles with their vectors pointed in the direction of the magnetic field.

Fig. 3. (*A*) The vectors oriented with B_0 spin in an opposite direction than those oriented opposite the magnetic field. Most of these cancel each other out. We are left with net vectors precessing around the *z*-axis oriented with the magnetic field (approximately 1 of 100,000 vectors). (*B*) The nuclear dipoles exchange energy with the surrounding molecular lattice. There is only a tiny energy difference between the up and down states, leaving a small net fraction of dipoles in the lowest energy state (pointing up).

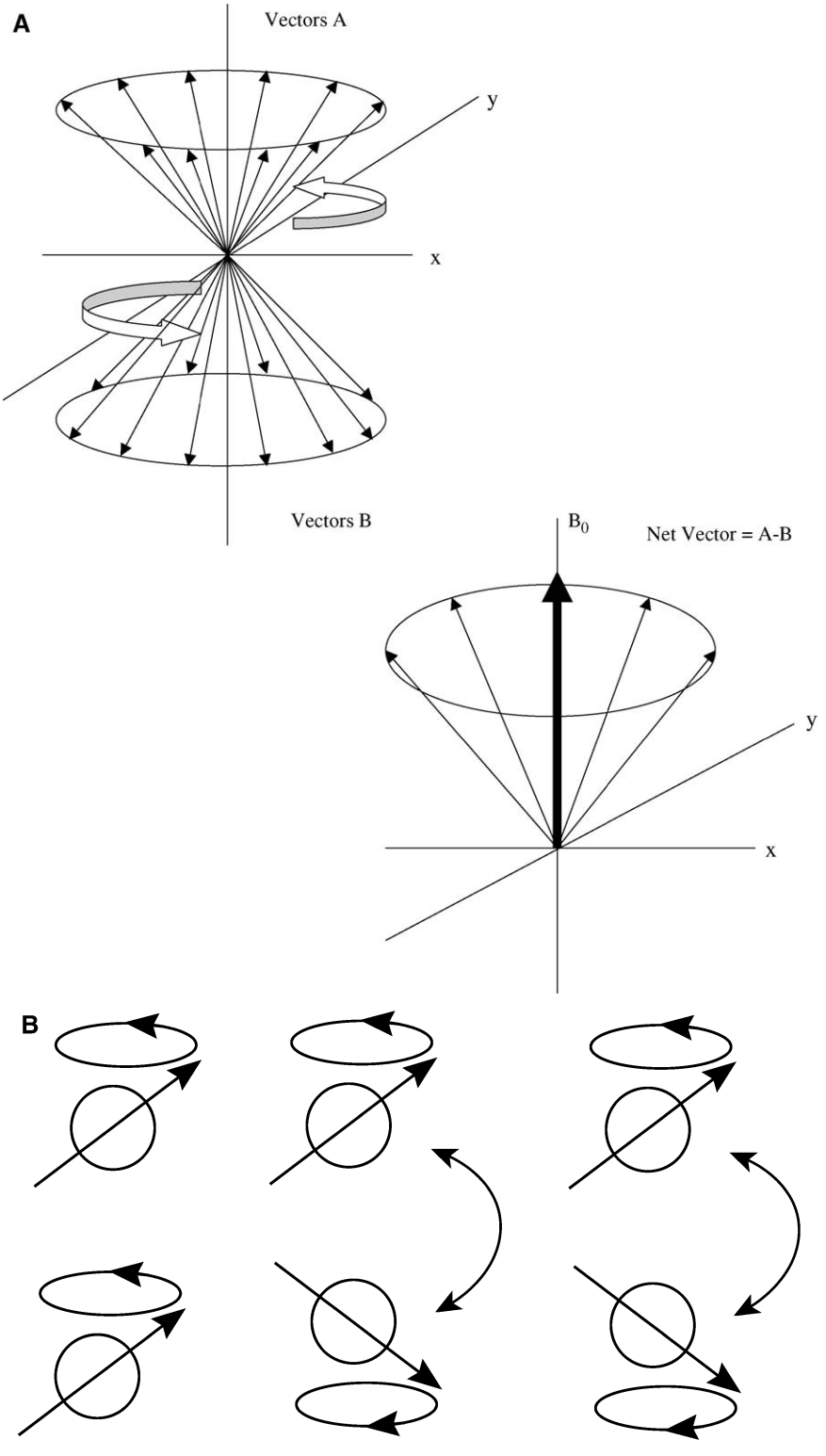
A
Vectors A
y
x
Vectors B
B0
Net Vector = A-B
y
x
B

Thermal motion

The second factor that causes important changes in our model is the effect of thermal motion. The energy difference between the two states (ie, for or against the magnetic field) is small compared with other energy transitions. For example, a typical x-ray produced by the deceleration of an electron into a tungsten anode is on the order of 100,000 electron volts. The energy from the transition of electrons from outer orbitals to inner orbitals, producing light, is on the order of 4 electron volts. The energy transition for a small proton dipole pointing for or against a magnetic field at 1.5 T is only 2.6×10^{-7} electron volts, a trillion-fold difference from x-rays. This corresponds to energy in the RF range. Energies in this range are ubiquitous in the environment because of thermal motion. The low energy of these transitions accounts for the safety of MRI. It also requires that the detection apparatus be extremely sensitive, however. It is a system that is noise limited.

Thus, each of the little dipoles in our model is influenced by the rapid exchange of thermal energy with the surrounding molecular lattice. As the dipole absorbs energy, it is raised to an excited state. As the relaxation process occurs, this energy is exchanged with the environment and the dipole is aligned in a lower energy (ground) state. Because of the thermal energy available, the proton dipoles undergo rapid shifts between orientations with and against the magnetic field. If the energy of the lattice were not available, relaxation would be extremely slow. At a given time, only a tiny net fraction is oriented with the magnetic field [12]. The distribution at room temperature is given by the Boltzmann equation:

$$\frac{N+}{No} = e^{-\frac{\Delta E}{kT}}$$

which with a Taylor's expansion, simplifies to

$$\frac{N+}{N-} = 1 + \frac{\Delta E}{kT} \text{ or } \frac{N+}{N-} = 1 + \frac{h\gamma B}{2\pi kT}$$

where k = Boltzman's constant (1.38066×10^{-23} J K^{-1}); T = Absolute temperature; B_o = Field strength in Tesla; h = Planck's constant (6.062608×10^{-34}) J sec; $\omega = \gamma B_o$ in rad sec^{-1}; $\nu = \gamma \frac{B_o}{2\pi}$ where $\gamma = \frac{\omega}{2\pi}$ in hz; $E = h\nu$; $\Delta E = h\nu = h\gamma B_o = \frac{h\gamma B_o}{2\pi}$; γ = gyromagnetic ratio (2.6751978×10^{-8} s^{-1} T^{-1}) for hydrogen.

This is field (B_o) dependent; thus, at 1.5 T, 9.88 of 1,000,000 are oriented with B_o, giving a larger fraction of nuclei available for excitation than at 1.0 T, which has only 6.59 of 1,000,000 oriented with B_o. This is why image quality is better at higher field strengths; more protons are available for excitation.

Because the vectors that are oriented against the magnetic field spin in an opposite direction, they cancel out any vectors precessing with the magnetic field. For the purposes of our model, we only need to consider the difference between the two, that is, the small fraction of nuclei that represent the difference between the two populations (Fig. 3A). We now have protons precessing at a specific frequency in a magnetic field, which are undergoing rapid up and down transitions, leaving only a tiny net magnetic vector, as is illustrated in Fig. 3B.

Phase coherence

The next element of our model is that of phase. Phase is a measure of the relative position of an object or vector; usually measured with an angle ϕ over a given time for a periodic function. A simple analogy may help to clarify this point. If we take two wheels, place a dot on one edge of them, as shown in Fig. 4, and spin them both with the same velocity, they remain spinning synchronously over time. If one wheel spins slightly faster than the other, however, the dots no longer align over time. They are said to be out of "phase" with each other. A similar process happens with nuclear spins.

Although the small dipoles are placed in a strong "homogeneous" magnet, the magnetic field that they sense is slightly different than that of their neighbors. This can be a result of several factors:

1. Although the magnetic field is homogeneous by technical criteria, it may still contain an inhomogeneity of approximately 1 part per million (ppm) [7]. This translates into a frequency difference of 63 Hz at 1.5 T. A dipole sensing a 1.5-T magnetic field spins slightly differently than an adjacent proton that experiences a magnetic field of 1.500001 T. In 8 milliseconds, protons in the same voxel sensing a difference of 1 ppm magnetic field inhomogeneity are 180° out of phase and cancel out each other's signal.
2. There are many local disturbances to the magnetic field ranging from the molecular level up through the tissue level. For instance,

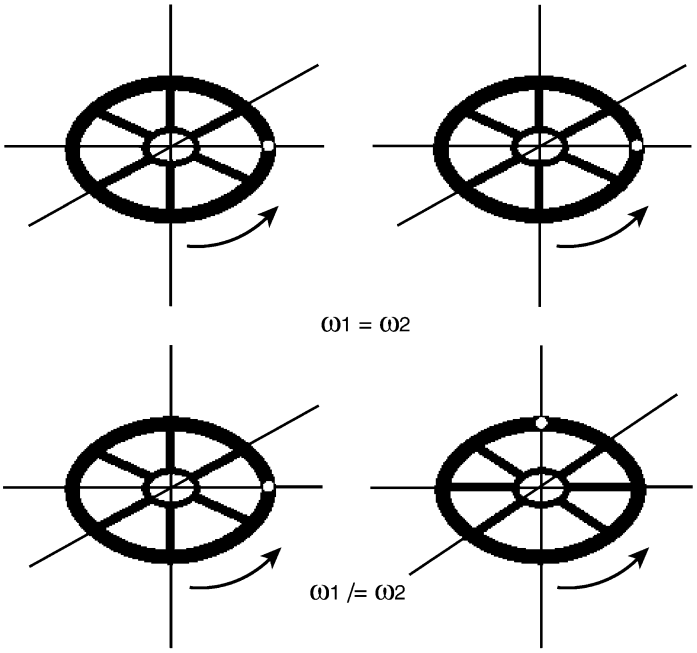

Fig. 4. A dot is placed on a spinning wheel. In the first case, the angular velocity of the two spinning wheels is equal and the dots stay synchronized with one another. They are said to be "in phase." In the second instance, the velocity of the first wheel is different from that of the second wheel. Over time, the relative position of the dots drifts "out of phase."

oxygen atoms, by their nature, are highly electronegative and tend to attract more of the shared electron cloud around themselves than does the adjacent hydrogen atom in a molecule like water. This causes the hydrogen nucleus to have less of a screening effect from the overlying electron cloud. It experiences a stronger local magnetic field than a proton attached to a fat molecule in that the protons are more shielded by valence electrons. Therefore, the spins of water hydrogen nuclei precess at a slightly greater frequency than those of fat.

3. Different substances have different permeabilities to the magnetic flux and can thus distort magnetic field lines. Most materials are diamagnetic, meaning that the magnetic flux lines would rather go through a perfect vacuum than through that substance. For example, at an air-bone or bone–soft tissue interface, the magnetic flux lines are distorted. Some materials, such as iron, are ferromagnetic and concentrate magnetic flux lines. All these make the local magnetic field different for adjacent nuclei, causing them to precess at slightly different rates. Because they precess at slightly different frequencies, they rapidly become out of phase with respect to each other, and coherence is lost.

Our model now consists of small nuclear magnetic dipoles rapidly precessing in space, each with a slightly different angular velocity, out of phase with respect to adjacent dipoles, and rapidly exchanging energy with the environment such that their dipole orientations are flipping back and forth in restricted quanta of energy for and against the magnetic field. One may then wonder how any useful information can be extracted from these weak signals, precessing at different velocities and completely out of phase with each other.

Net vector

At this point, a short diversion is necessary to understand signal generation. Each of the individual spinning nuclear dipoles can have only one of two orientations with respect to the magnetic field. If we average the orientations of these, we can obtain a net vector that can have any orientation with respect to the magnetic field. This averaging of the individual directions is illustrated in Fig. 5. This net vector can be thought of as a larger single dipole. For example, if sufficient RF energy is given

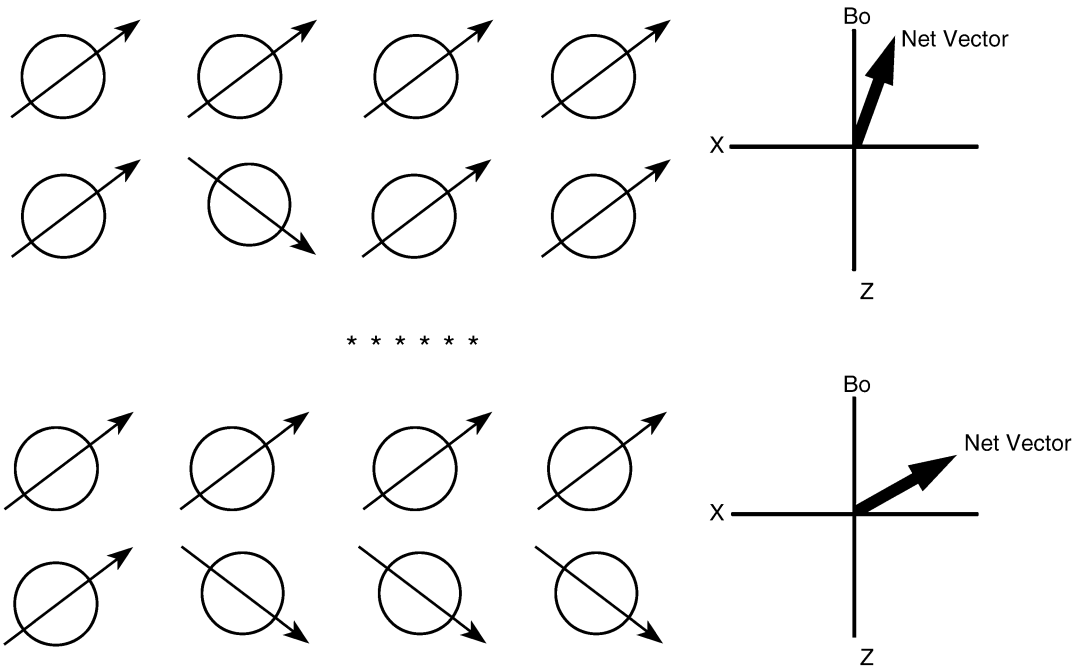

Fig. 5. The concept of a net vector. Each of the individual nuclear dipoles is added. Now, rather than pointing at 35.3° for or against the magnetic field, the net vector is the sum of the positions of all the vectors.

to a sample of spinning hydrogen nuclei, a fraction of them can be rendered into the excited state and the net vector tipped from 0° through perhaps 90°. This would reflect a 90° RF pulse. By convention, the axes used in MRI are *x*, *y*, and *z*. The *z*-coordinate is taken along the main magnetic field, and the protons process around *z* in the *x*-*y* plane. We remember that if a magnetic dipole spins, an electrical current can be induced in a coil oriented perpendicular to this, just as the converse is seen with a coil-conducting current that induces a magnetic field. This is shown diagrammatically in Fig. 6.

Signal formation

The key to obtaining any useful information from the precessing protons is to establish coherence, that is, having a large portion of the dipoles all spinning together with a net vector precessing in the *x*-*y* plane, where signal can be generated in a suitably oriented coil. How then is phase coherence established and signal generated? RF waves are electromagnetic radiation that have time-varying magnetic fields propagated through space. These time-varying magnetic fields can interact with the oscillating magnetic field of the spinning hydrogen dipole.

To understand how phase coherence is achieved, we must first understand the B1 field created by the transmitting RF coil. In Fig. 7, a loop of wire is fed an oscillating RF current. As we remember from our basic college physics, current flowing through a wire induces a magnetic field perpendicular to the flow of current according to the right hand rule. If the current is oscillating, as occurs with a RF pulse, a sinusoidal oscillation of the B1-induced magnetic field of the

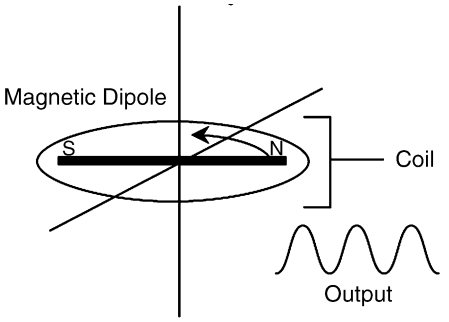

Fig. 6. An electromagnetic pickup coil oriented perpendicular to the spinning dipole acts as a tiny generator in which an oscillating electrical current is created.

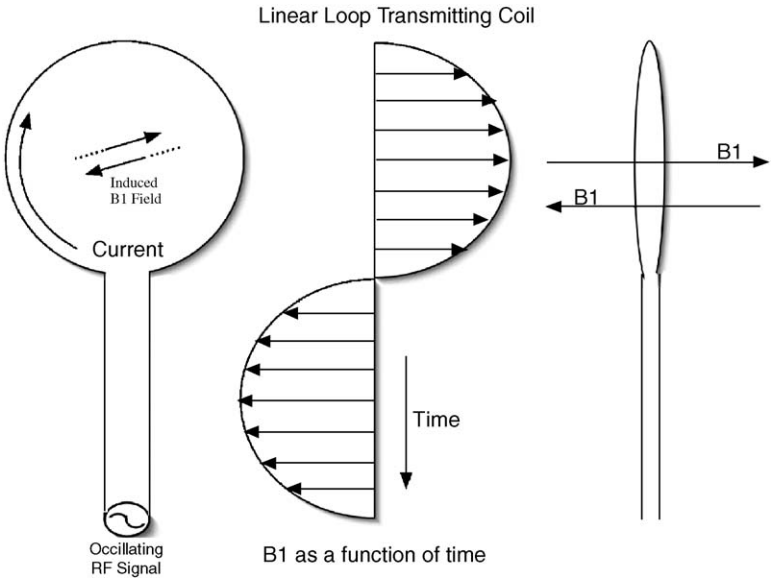

Fig. 7. Passing an oscillating current through a coiled wire creates an oscillating magnetic field (B1) perpendicular to the coil that moves in and out perpendicular to the face of the coil as a function of time.

coil is created. The transmitting coil creates a magnetic vector perpendicular to its face, which increases and decreases and then reverses over time as a function of the RF oscillation. If one thinks back to our spinning wheel analogy, the magnetic vector would be going in and out over time along the axis of the spokes (Fig. 8). Most RF transmitters use a circularly polarized transmitting coil, which creates a wave of an oscillating B1 magnetic field that rotates around the sample with a B1 vector going in and out perpendicular to the *z*-axis (Fig. 9).

The next thing to understand is spin locking. If we looked at only the vectors in the *x*-*y* plane from our net vector in Fig. 3B, it would look like Fig. 10. The vectors are precessing in the *x*-*y* plane all out of phase with respect to each other.

Spin locking or synchronization of the vectors occurs as the spin dipoles are "pushed" together by the synchronized B1 field of the RF transmit coil. Some authors use a rotating frame of reference, a mathematic trick in which the observer rotates around the vectors to describe a classic model of the interaction with the spinning vectors. I prefer to view this from a more linear approach. In Fig. 11, the circular motion of a given vector of the spinning nucleus observed from one point of the transmit coil can be viewed as a series of vectors of increasing and then decreasing sinusoidal intensity over time. In other words, the vector pointing at the coil is doing exactly the same thing that the oscillating transmitted RF wave is doing by creating a vector that goes in and out perpendicular to the *z*-axis. Think of the component of the vector facing the coil as something like a piston that oscillates in and out perpendicular to the axis of a fly wheel. The B1 vector acts like a piston opposing or reinforcing the motion of the spinning hydrogen vector (Fig. 12). The B1 vector created by the oscillating magnetic field of the RF wave quickly brings the vector of the nucleus into synchronization; however, this does not occur instantly. The time constant for this process is called $T1_{rho}$. If we think of an ensemble of nuclei spinning in a voxel in different phases, the B1 vector moves coherently in a circularly polarized fashion around the spinning nucleus, with all the B1 vectors in phase from the oscillating RF transmit coil. This quickly synchronizes all the opposing vectors, bringing them into coherence much like independent pistons working with or against a large coherently operated crank shaft with synchronized pistons (Fig. 13).

Thus, with the tiny individual magnetic dipoles in phase, we can add each of them together, giving a large single magnetic dipole. With coherence now established and a net dipole vector precessing in the *x*-*y* plane, a signal is generated in the coil or antenna. This signal represents a free induction

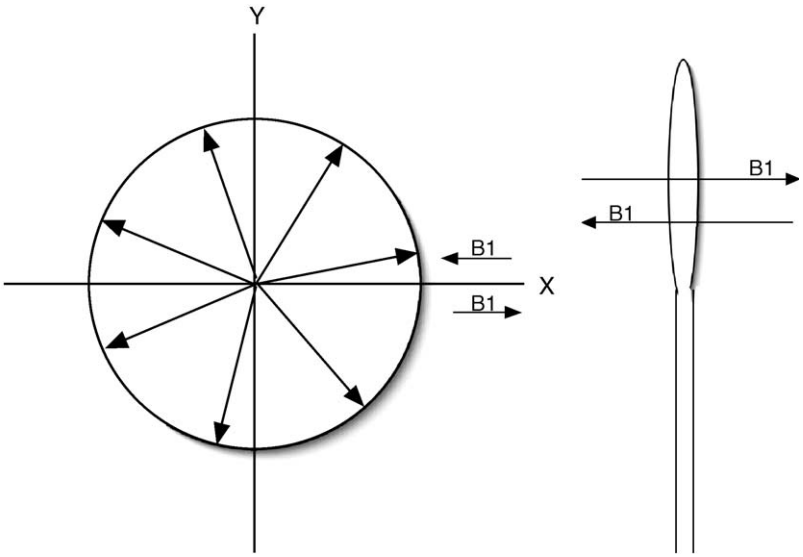

Fig. 8. The transmitting coil creates an oscillating B1 field over time that moves in and out perpendicular to the spokes of the turning wheel, which would be the representation of the precessing vectors in the *x*-*y* plane.

decay (FID). Of course, this does not last long. Because the precession rate for the nuclear dipoles varies with magnetic field differences, phase coherence is lost and the signal rapidly decays, as demonstrated in Fig. 14. The length of time the signal persists is a measure of how rapidly phase coherence is lost.

By applying RF energy, a two-part change has occurred within the system. First, a certain fraction of the nuclei were inverted into the excited state against the main magnetic field, giving us a net magnetic vector that is not oriented with the longitudinal *z*-coordinate. Second, phase coherence that had not previously been present was established. Over time, the system returns to its natural random state.

T1 relaxation

The rate at which the proton dipoles relax back into the aligned state with B_o (lowest energy) is constant over time for a given substance at a given field strength. As more of the protons relax, however, a smaller percentage of nuclei are in the excited state; thus, fewer are available overall to relax. This describes a typical exponential relaxation curve, as illustrated in Fig. 15. At a time of 1 T1, 64% of the longitudinal

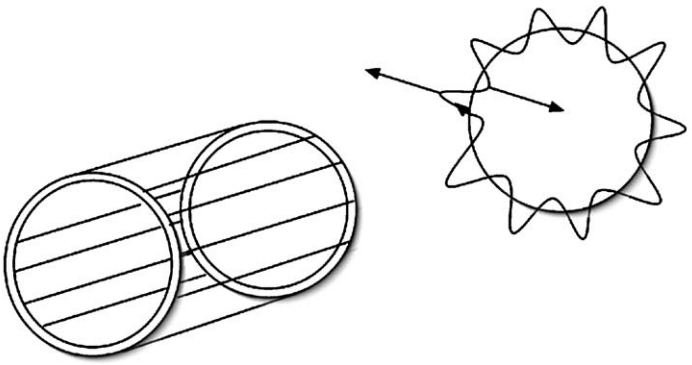

Fig. 9. A circularly polarized transmit coil creates an oscillating B1 field that moves in and out perpendicular to the *z*-axis that rotates around the sample.

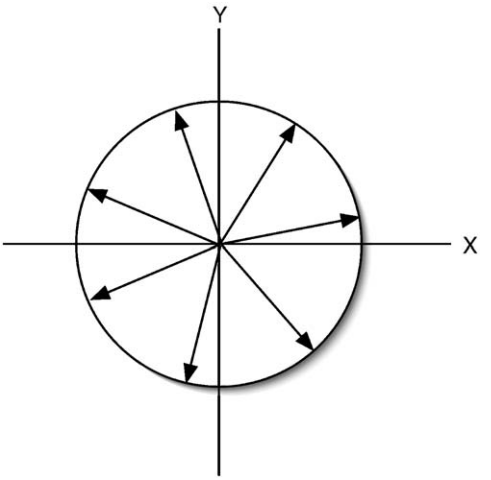

Fig. 10. Top down view of Fig. 3 demonstrates the precessing *x-y* component of the vectors spinning around randomly completely out of phase with respect to each other.

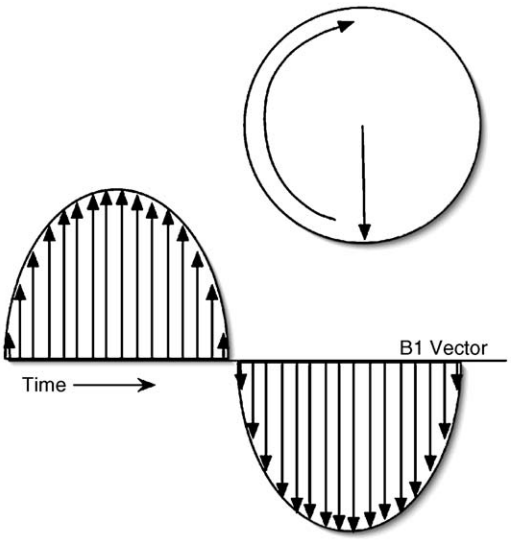

Fig. 11. If one stands at a given vantage point watching the precessing nuclear dipole, the vector increases and then decreases in a sinusoidal oscillating function over time.

magnetization has recovered. By four T1, 98% of the longitudinal magnetization vector has been recovered. The process of changing from an excited to a nonexcited orientation in the magnetic field involves an energy exchange, the energy of which is precisely equal to the Larmour frequency of the spinning nuclear vector. What MRI is really seeing inside the body is energy—the energy of precessing nuclear dipoles.

As previously noted, these energies of exchange can be obtained from molecular motions and vibrations in the molecular lattice. For this reason, T1 is commonly referred to as the "spin lattice relaxation time." From quantum theory, only a discrete energy value is allowed to induce this transition. Energy is related to frequency, υ, by the equation $E = h\nu$, where h is equal to Planck's constant [13]. An important concept is that the excited magnetic dipole can relax only if it can transfer its discrete energy into the surrounding molecular lattice. These molecular energy states are present in the form of rotational and vibrational motions of the molecules. Certain types and structures of molecules are far more efficient in accepting these energies, because their vibrational and rotational energies correspond more closely with the Larmour frequency. Frequencies that are too high or too low do not efficiently interact with the nuclear dipole; thus, T1 relaxation is slowed [14].

For example, water molecules are small. They rotate and vibrate quickly and have a relatively

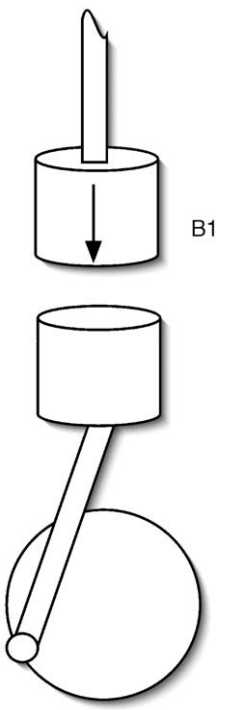

Fig. 12. The oscillating B1 vector exerts a force on the spinning proton nuclear vector much like two opposing pistons in a cylinder.

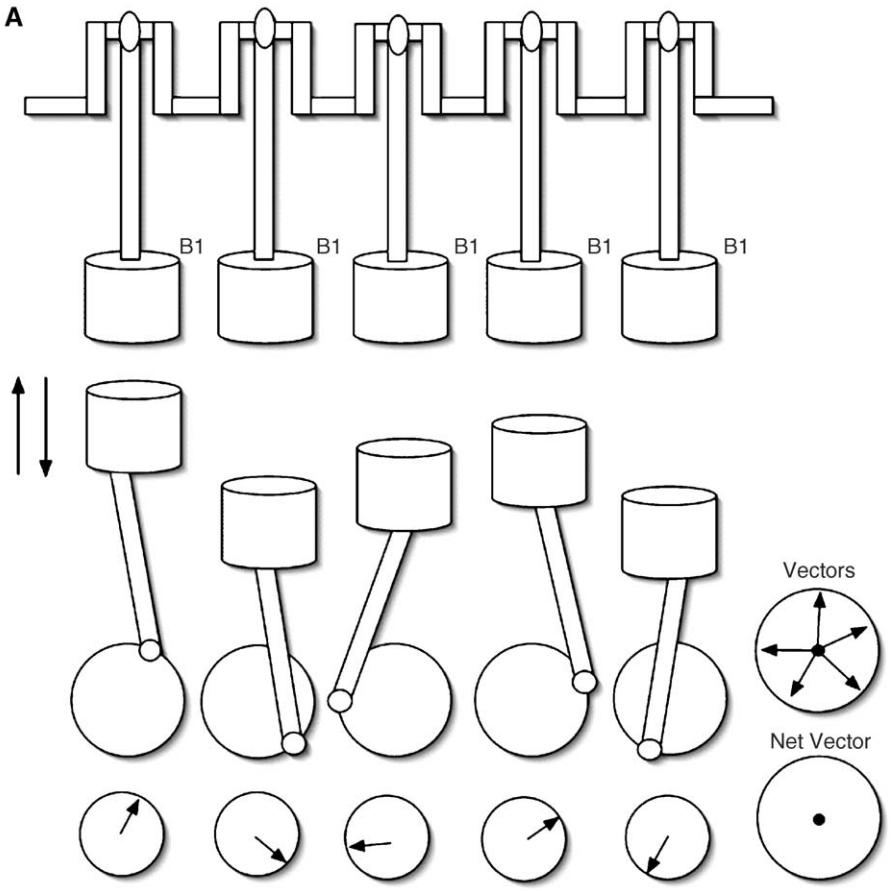

Fig. 13. (*A*) An assembly of pistons on the bottom row represents each of the different proton vectors at different phases, creating a net vector of zero. (*B*) With the application of the synchronized force of B1 represented by an array of pistons at the top of the diagram, the vectors of the precessing protons are rapidly brought into synchronization, giving a strong net vector.

higher spectral frequency of lattice energies. Pure water contains little of the spectral energy needed to induce T1 relaxation of the small nuclear dipoles. Conversely, fat molecules that tumble more slowly have a spectral energy more closely matched to the Larmour frequency and hence allow for more efficient relaxation. When the protons undergo faster T1 relaxation, more of their longitudinal vector is available for each succeeding pulse. Therefore, more signal is generated, because a larger vector is available to precess in the *x*-*y* plane. That substance appears relatively brighter. For this reason, fat is bright on T1-weighted (T1W) images (images that accentuate differences in the T1 of tissues) and water is dark (Fig. 16). Likewise, myelin, which has a slowing effect on the motion of adjacent water, is relatively bright on T1W sequences [15]. Nevertheless, this can be pushed too far. Extremely large solid-like structures, such as bone or proteins (eg, ligaments and other highly ordered proteins), have protons that are relatively immobile. They give little signal on T1W imaging, because the rotational and vibrational frequencies have been slowed to the point that they are no longer optimal for relaxation [12,16]. Similarly, protons on cholesterol and lipid membranes have relatively poor mobility and have longer relaxation times as opposed to adipose tissue (storage fat), which has molecules that are in an oil (liquid) state, are more mobile, and relax more quickly. Paramagnetic materials also improve T1 relaxation, as can nonparamagnetic calcium salts [17].

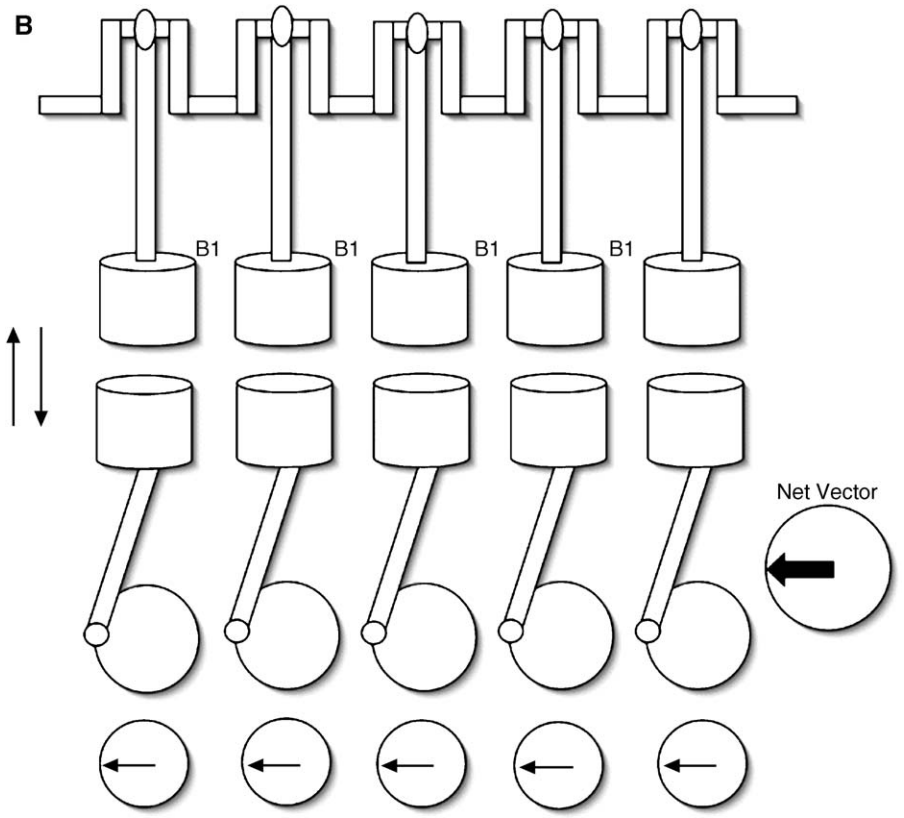

Fig. 13 (*continued*)

By the same token, the relaxation of biologic material is more or less efficient depending on the strength of the magnetic field. T1 relaxation is field strength dependent [18,19]. Table 1 gives data comparing T1 relaxation times of selected tissues at 24 and 2.5 MHz [105].

In general, T1 relaxation is more efficient for lower frequency (field strength is proportional to frequency) over the range of magnetic field strengths used clinically. Thus, shorter repetition times (TRs) can be used for a 0.35-T magnet versus a 1.5-T magnet to achieve equal T1 relaxation (and hence T1 contrast between tissues).

T1 relaxation is a thermodynamic process involving enthalpy, in that an energy exchange occurs. The surrounding lattice must be able to accept the precise quanta of energy emitted by the relaxing nuclear dipoles. The difference in relaxation between small, intermediate and large molecules is illustrated in Fig. 17. T1 can be measured by sampling the system at various time intervals to see how much longitudinal magnetization is present after a given amount of time. To measure T1 accurately, the TR (ie, the time before the system is re-excited) must span values above and below T1. The TR is varied, and signal intensity is plotted as a function of TR. The slope of the curve is related to T1: Signal = $M_o\ (1 - e^{-TR/T1})$ [20].

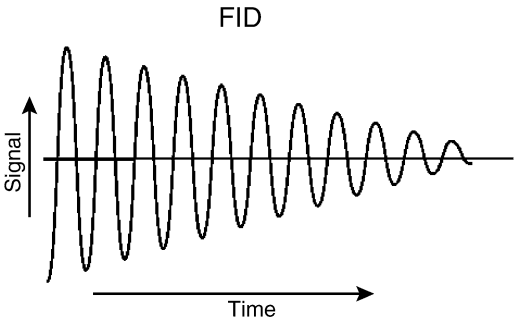

Fig. 14. When all the vectors are spinning in synchrony, the maximum signal intensity is generated in the coil. Over time, however, these vector dephase, and there is rapid loss of signal intensity. This represents free induction decay (FID).

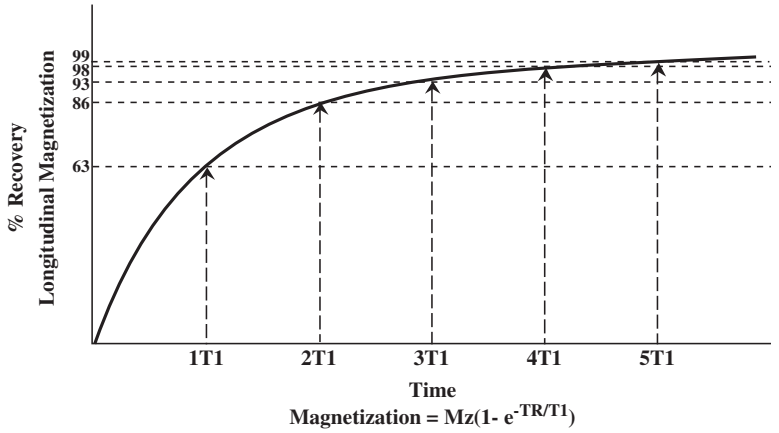

Fig. 15. Graphic representation of T1 relaxation. The exponential recovery of T1 demonstrates that at a time of 1T1, 63% of the signal intensity has recovered. By 5T1, 99% has recovered.

T2 relaxation

The other decay process that is occurring simultaneously with T1 relaxation is the loss of phase coherence. This is termed *T2 relaxation* or *spin-spin dephasing* (ie, one spin becomes out of phase with another spin). As opposed to T1 relaxation, the loss of phase coherence is not one that requires an exchange of energy. In chemical terms, it is a process involving entropy, or a disordering of an ordered state. This also occurs at an exponential rate [20] (there is more signal to dephase early on): Signal = $M_o e^{-(TE/T2)}$. As the spins dephase, the magnetic vectors precessing in the *x-y* plane gradually fan out. After a certain period, all phase coherence is lost and no more signal is generated. At a time of T2, 64% of the phase coherence is lost.

The loss of phase coherence is caused by only one thing—a slightly different magnetic field experienced by adjacent spinning proton dipoles. This slightly different magnetic field can be achieved by many different processes, however. These differences in magnetic field can be subdivided into two major categories.

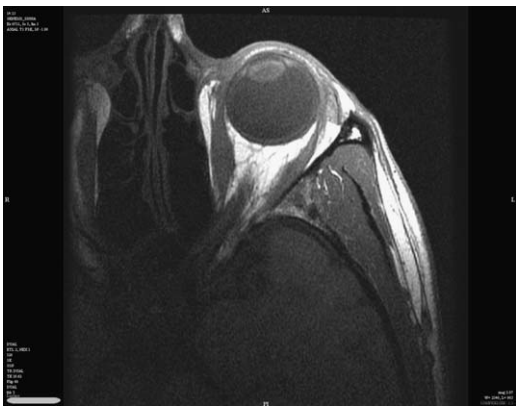

Fig. 16. Orbital MRI scan with T1 weighting. Fat is bright, bone is dark, muscles are low signal, and vitreous humor is dark. Note that the lens is slightly brighter than the vitreous fluid, because the water is bound to proteins, which slows its motion.

Static magnetic fields

Static magnetic fields vary in intensity over space but not over time during image acquisition. Examples of this would include magnetic field inhomogeneities by the magnet itself, perturbation of the local magnetic field by materials that have different magnetic permeability, such as bone, air, or stationary paramagnetic or ferromagnetic materials. Because these magnetic field

Table 1
T1 relaxation values

	24 MHz (milliseconds)	2.5 MHz (milliseconds)
Clotted white blood	867	404
Serum	1590	820
Gray matter	644	332
White matter	469	264

From Ling CR, Foster MA, Hutchison JMS. Comparison of NMR water proton T1 relaxation times of rabbit tissues at 24 MHz and 2.5 MHz. Phys Med Biol 1980;25:748; with permission.

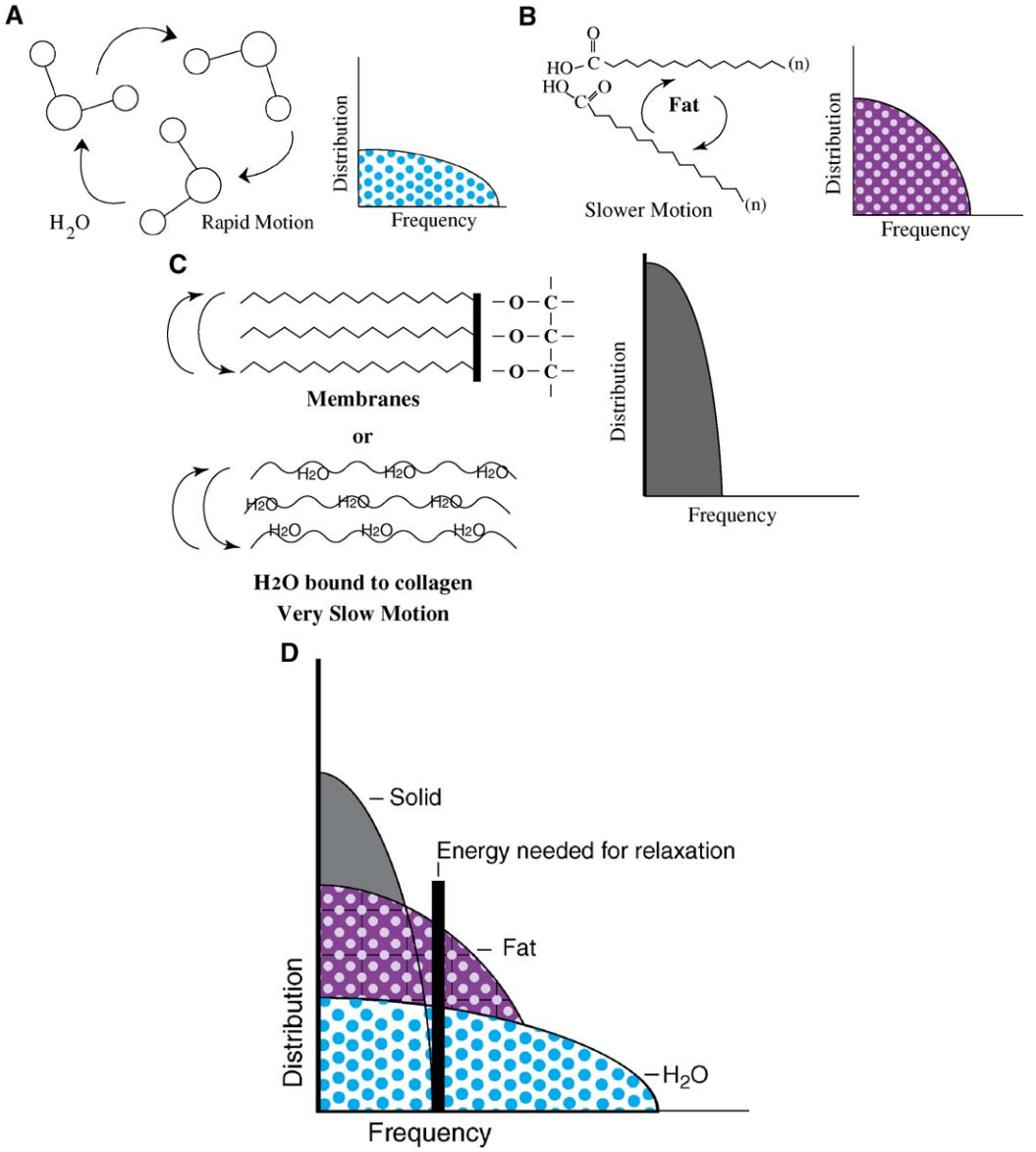

Fig. 17. (*A*) Water molecules tumble rapidly and have a large population of high frequency vibrational and tumbling energy states. As a result, T1 relaxation is inefficient. (*B*) Fat molecules, on the other hand have a larger proportion of motional states correlating with the energy needed for relaxation. (*C*) Complex molecules such as membranes or water bound to large protein molecules exhibit very slow motion resulting in low frequency components that are below the energy needed for relaxation. (*D*) A composite figure demonstrates that fat will have better efficiency at relaxation than eigher water or solid materials. This is the result of the quantum requirement for discrete energy transitions which can be supplied only with certain molecular vibrational and rotational states.

inhomogeneities are constant in time, the signal loss from dephasing can be recovered by the use of a second 180° pulse, which rephases the nuclear spins (more about this in the section on pulse sequences).

Time-varying magnetic fields

Water molecules, for instance, can move rapidly through space and across membranes and can randomly bounce around within and between

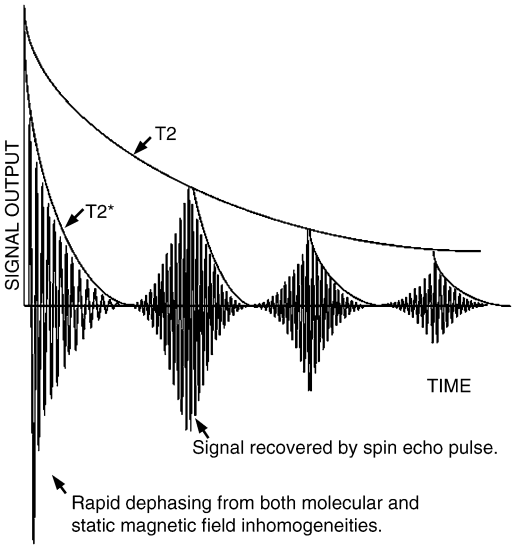

Fig. 18. T2 relaxation versus T2* relaxation. Phase loss occurs in two ways: reversible phase loss and irreversible phase loss. T2* is a combination of the phase losses of static (reversible) and nonstatic (irreversible) field inhomogeneities. Using a spin echo pulse technique, the signal loss induced from static magnetic field inhomogeneities can be recovered and the T2 relaxation measured. This figure graphically illustrates why the T2-weighted sequences always have greater signal intensity than a T2*-weighted sequence for a constant echo time.

adjacent voxels. The water molecule that moves into a new area of different magnetic field strength precesses at a slightly different rate and therefore becomes out of phase. Because it is not static, however, a reversal of its spin cannot bring it back into phase coherence, and this part of the signal is lost. T2* is the combined loss of phase coherence from static and time-varying magnetic field inhomogeneity. The difference between phase lost from static and time-varying magnetic field inhomogeneities is shown diagrammatically in Fig. 18.

Phase loss can occur not only between adjacent voxels or imaging points in our data set but within a voxel as well. For example, fat and water precess at slightly different frequencies. The hydrogen of a water molecule, being less shielded by the electron cloud of its oxygen neighbor, experiences a higher magnetic field strength and thus precesses at a faster rate. If a voxel contains equal quantities of fat and water, they are exactly out of phase with each other at certain times causing the signal to cancel.

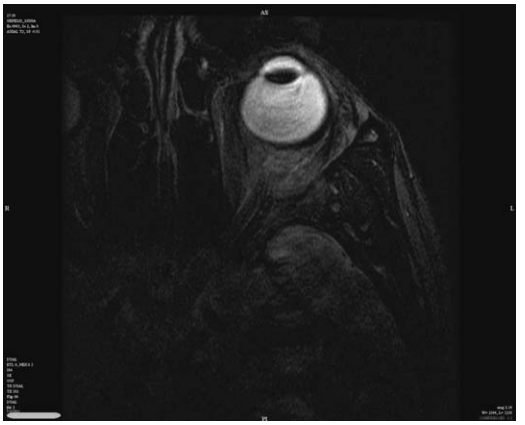

Fig. 19. Axial T2-weighted orbit image. Fat is darker, the lens is dark (complex protein), and the vitreous (water) is bright.

T2 relaxation is greatly augmented by having a distorted magnetic field. Different tissues have different T2 relaxation rates depending on their physiochemical constituents. Water tumbles rapidly in space. As it does, any magnetic field distortions are rapidly averaged out over time. Thus, adjacent water molecules all experience a similar magnetic field, and their nuclear dipoles dephase slowly. Let us suppose, however, that a protein or large polysaccharide molecule is introduced into the solution. The water molecules bound to the biologic polymer rotate more slowly than adjacent free water, and magnetic field inhomogeneities are averaged less well. Because of this, the water molecules in different hydration states experience different magnetic field strengths over the period of image acquisition. An excellent example of this is the lens of the eye. The rigidly held water molecules in proteins rapidly lose phase coherence, generate a small signal for imaging, and thus are dark on T2-weighted (T2W) images. Fat, being a much larger molecule than water, is held more rigidly in space over time and thus loses phase coherence more rapidly than free extracellular water; fat darkens relative to water with increased T2 weighting (Fig. 19).

If water molecules are adjacent to or within voxels containing materials that cause distortions of the magnetic field, they likewise rapidly lose phase coherence. For example, iron deposits in the basal ganglia destroy phase coherence, giving little signal on T2W images. Likewise, the injection of magnetite, a ferromagnetic substance that causes strong local field inhomogeneities,

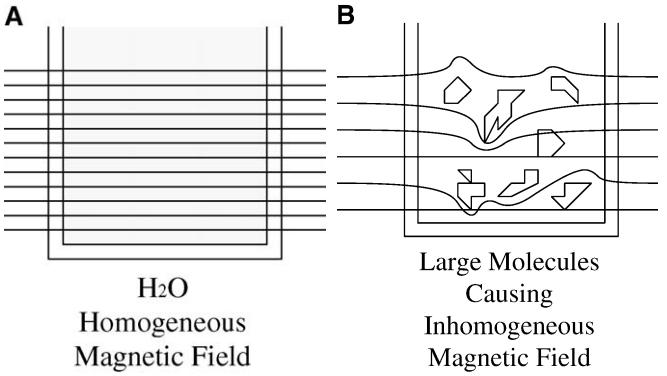

Fig. 20. Comparison of a small versus large molecules on magnetic field homogeneity. (*A*) The rapid tumbling motion of water molecules evens out micro magnetic distortions giving a homogeneous magnetic field. (*B*) Large solid or semi-solid molecules do not tumble as rapidly. Therefore, small perturbations of the local magnetic filed occur.

destroys phase coherence and gives dark signal on T2W images. Materials that are more solid move more slowly and thus have a more inhomogeneous local magnetic field. Fig. 20, illustrates how a semisolid material distorts the local magnetic field compared with a rapidly tumbling small molecule. For most substances, phase is lost much more quickly than restoration of proton dipole alignment with the *z*-axis (ie, T2 relaxation is much shorter than T1 relaxation). A comparison of various substances is given in a qualitative way in Table 2.

Table 2
T1-weighted and T2-weighted appearance of various body tissues

	Appearance on sequences	
	T1-weighted	T2-weighted
Rigid molecules		
Bone		
Fibrocartilage		
Ligaments	Dark	Dark
Scar		
Hemosiderin		
Watery substances		
Cerebrospinal fluid	Dark	Bright
Cysts		
Free water		
Intermediate molecules		
Fat	Bright	Intermediate
Proteinaceous material	Intermediate to bright	Intermediate to bright depending on water content
Hyaline cartilage	Intermediate	Intermediate to dark
Lens of eye	Bright	Dark

Recovery of magnetization vector to ground state (T1 relaxation)

Let us return to our model briefly. After an RF pulse is given, a magnetization vector is established that is precessing coherently in the *x*-*y* plane. Suppose that a sample contains a variety of substances that have different T1 relaxation values (A, B, and C for short, intermediate, and long T1s, respectively). Given a long enough time, all the magnetization vectors of the various substances return to an equilibrium position along the *z*-axis. If we excite the system at an intermediate time, those voxels with short T1s will have already relaxed, with their magnetization vectors oriented parallel to the *z*-axis before the next excitation. Tissues with longer T1s will be somewhere in between. Their relative positions are shown in Fig. 21. If the sample is given a repeat 90° RF energy pulse at this point in time, the entire vector of the short T1 substance labeled A can be rotated into the *x*-*y* plane and is available for generating signal. Those substances with intermediate and longer T1s (B and C, respectively) have less magnetization available to precess in the *x*-*y* plane and generate less signal in our receiver. Thus, maximum signal is obtained by waiting a longer period for full longitudinal magnetization recovery to occur or by speeding the T1 relaxation of the slower substances through the use of paramagnetic agents. Differential intensity between voxels of different T1s can be achieved by selecting a TR close to the T1 of the tissue of interest. To repeat, the brightest tissues on T1W pulse sequences are those that have the shortest T1 and thus have the most available longitudinal magnetization available for inversion into the *x*-*y* plane

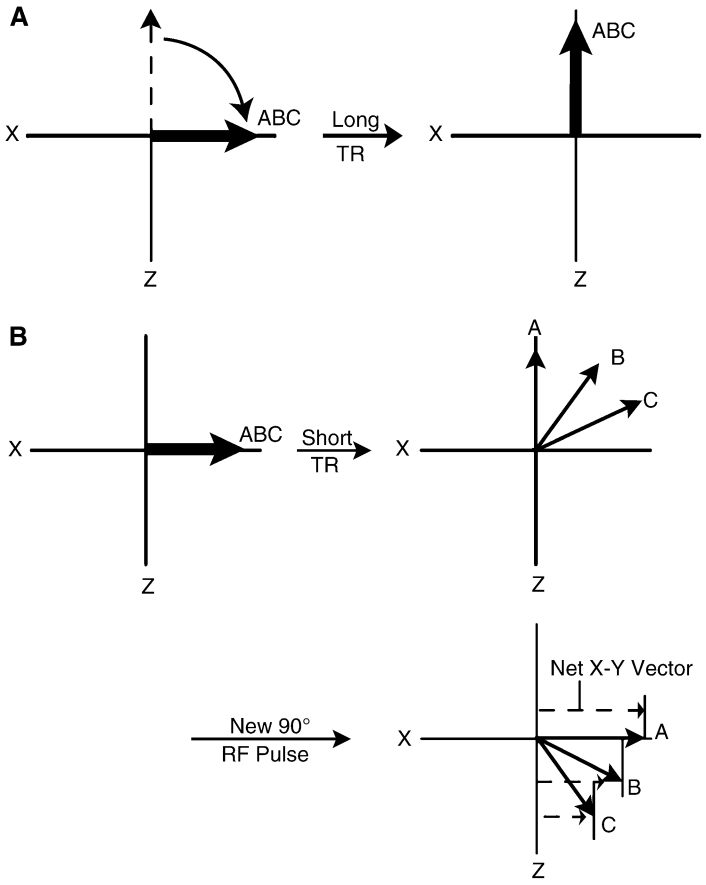

Fig. 21. Comparison of T1 relaxation between substances with short, intermediate, and long T1s. (*A*) In the first instance, vectors A, B, and C are excited into the *x-y* plane. A long time follows before the pulse is repeated. At such time, TR, repitition time, all the vectors will be back to their ground state and ready for full excitation into the *x-y* plane. (*B*) A similar experiment is performed, except that a short TR is used. At the time that a new 90° radiofrequency (RF) pulse is delivered, substance A with a short T1 will be tipped fully into the *x-y* plane, giving the largest signal. Its net vector is larger than that of a substance such as C, which has a long T1 relaxation time that has not fully relaxed before excitation, yielding a smaller net vector in the *x-y* plane.

at the beginning of each pulse repetition. Table 3 gives the values of T1 for various tissues. Remember, T1 relaxation is field strength dependent; therefore, it is not possible to use values obtained at high field strength to compare with low field measurements and vice versa. One should also know that there is considerable variability in the measurement of T1 between different instruments and different investigators. As such, the T1 relaxation of a tissue is not useful as an absolute comparison with other disease processes. Field strength, equipment type, temperature, selection of the sampling sequence, TR [21], and slice thickness all influence the obtained value.

How fast tissues lose coherence

Paradoxically, tissues that have a short T2 have the least signal. This is easily understood by the fact that as phase is lost, signal is destroyed and image intensity is decreased. Substances like free water, which maintain phase coherence for a longer period, have relatively greater signal than tissues with a short T2 if the data sampling (related to echo time [TE]) is taken at longer and longer times after excitation. Almost all pathologic processes (eg, tumors, inflammatory disease, infections, trauma) result in increased water content and edema. For this reason, they are best seen on

Table 3
T1 Relaxation values for various tissues

Brain	1.5 T	4.0 T
Gray matter	850 [21]–1023 [23]	1724 [77]
White matter	550 [21]–710 [23]	1043 [77]
Cerebrospinal fluid	3200 [21]	4550 [77]
Fat (adipose)	200 [106]	
Muscle	800 [106]	

T2W images. The optimum TE should be that closest to the T2 of the tissue of interest [22]. For instance, a cyst or area of edema may have long T2 times; sampling is best done at long TEs to distinguish the affected area from adjacent tumor tissues. If one wishes to distinguish between gray and white matter (Fig. 22), such long TEs are not advantageous, because a significant amount of signal is lost; the tissue is sampled long after the optimum difference between the signal intensities is observed. If one wishes to view only cerebrospinal fluid (CSF), a long T2 of 200 milliseconds provides a myelographic effect (Fig. 23). Such relative signal intensity for different substances as a function of TE is illustrated in Fig. 24. Table 4 gives T2 relaxation values for various biologic tissues and fluids. T2 relaxation, unlike T1 relaxation, is not field dependent. Equipment variances and differences in sampling techniques have led to wide variations in reported T2 values of different tissues. Again, these cannot be used to compare absolute values. However, on a given MRI machine, the reproducibility of T1 and T2 measurements is excellent, ranging from 5% to 9% variance [23].

Initially, it was hoped that different pathologic processes could be differentiated on the basis of characteristics T1 and T2 signatures [24,25]. Unfortunately, there is a wide overlap between benign and malignant processes [26–28], yielding

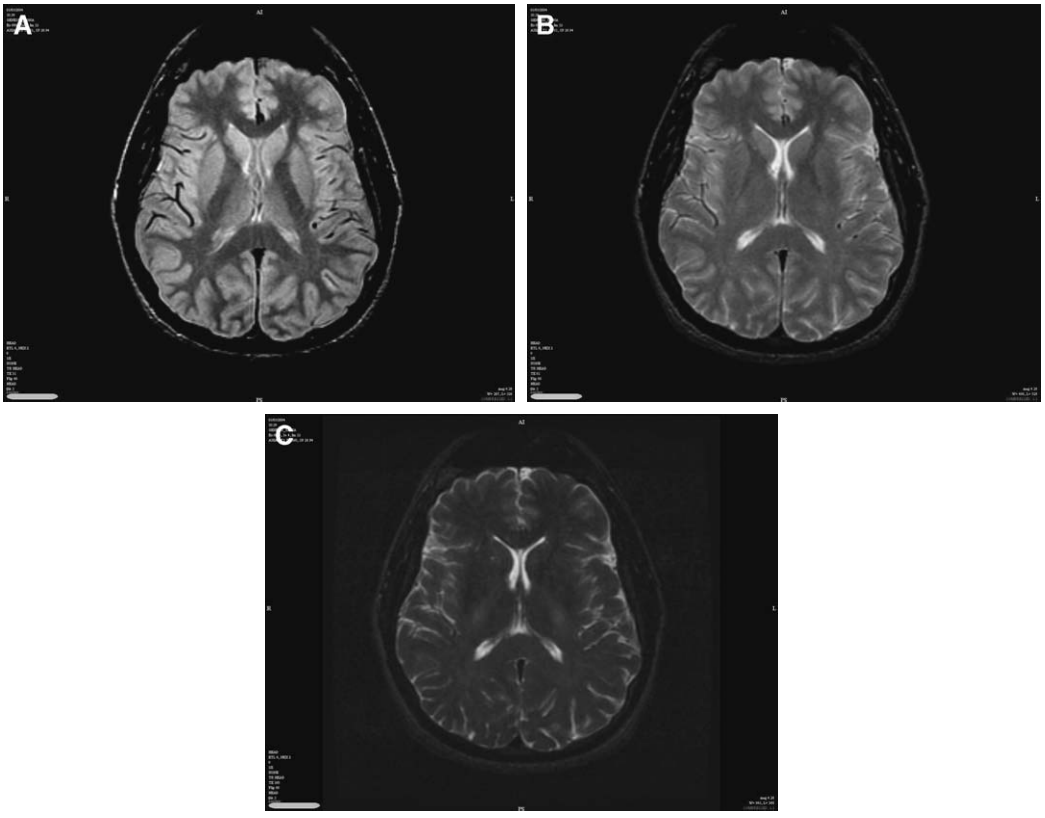

Fig. 22. A patient studied with Carr-Purcell-Meiboom-Gill sequence, multiecho, T2-weighted images with echoes at 31, 81, and 160 milliseconds. (*A*) At the lower echo time (TE; 31 milliseconds), the best gray/white differentiation is achieved. Notice that the white matter is relatively dark compared with the gray matter at a TE of 81 milliseconds (*B*) and 160 milliseconds (*C*). With an extremely long TE, however, the cerebrospinal fluid is prominently displayed, but there is loss of the gray/white differentiation.

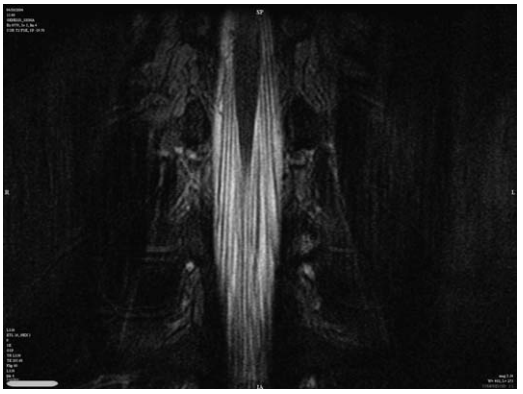

Fig. 23. Fast spin echo (FSE), heavily T2-weighted, coronal, lumbar MRI scan demonstrating excellent contrast between the cerebrospinal fluid of the subarachnoid space and the conus medullaris (*arrows*). All other structures are relatively dark. (FSE repetition time = 8000 milliseconds, echo train length = 16 milliseconds, echo time = 192 milliseconds, 24-cm field of view, 4-mm slice, 512 × 384 matrix, number of excitations = 2).

little benefit to measuring T1 or T2 of a given disease. Furthermore, the characterization of pathologic processes is complex by relaxation measurements and changes as the pathologic process develops [29].

Table 4
T2 Relaxation values for various biologic tissues and fluids

	T2	Frequency (MHz)
White matter	65 [106]–75 [23]	60
Grey matter	105 [106]–85 [23]	60
Cerebrospinal fluid	2000 [107]	25 [107]
Blood	250	20
Fat	200	60
Muscle	63	63

Data from different experiments and under different conditions.

From Bottomley PA, Foster TH, Argersinger, Pfeifer LM. A review of normal tissue hydrogen NMR relaxation times and relaxation mechanisms from 1–100 MHz: dependence on tissue type, NMR frequency, temperature, species, excision and age. Med Physic 1984;11(4): 425–48; with permission.

How much hydrogen is available to image

A third important parameter of signal intensity is that of the hydrogen spin density. Substances that contain more hydrogen atoms have more signal than those with fewer hydrogen atoms (eg, water versus bone). An obvious fact is that if the hydrogen atoms move out of the plane of interest

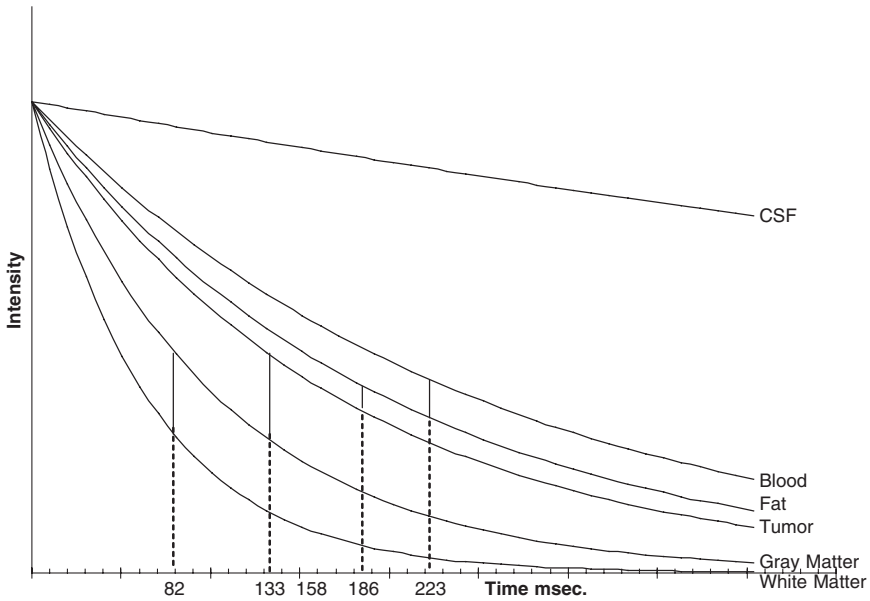

Fig. 24. Hypothetic T2 decay curves for various biologic substances, such as white matter, gray matter, cysts, and tumors. Notice that the best time to sample the data (echo time [TE]) depends on what one is looking for [ie, if one wishes to distinguish between gray and white matter, a TE of 65 milliseconds is chosen; if one wishes to distinguish between gray matter and cerebrospinal fluid, a TE of 145 milliseconds is chosen]).

during signal acquisition, signal is again lost. This can be illustrated by the flow void seen with flowing vessels.

We can combine these concepts into a single equation that should not be difficult to understand [22]. The signal intensity (I) for a given sample is related to the number of hydrogen atoms (ie, hydrogen spin density) given by S and to two exponential decay components: the T1 relaxation given by $1 - e^{-(\frac{TR}{T1})}$ and the T2 relaxation given by $e^{-(\frac{TE}{T2})}$; therefore, $I = S \times [1 - e^{-(\frac{TR}{T1})}]\ [e^{-(\frac{TE}{T2})}]$. For signal to be acquired, the magnetization vector must precess within the *x-y* plane and must be coherent.

To summarize our model thus far, the spinning of small subatomic particles creates a small magnetic dipole. The energy of interaction with an externally applied magnetic field can exist only in discrete energy states (quantum levels). For the hydrogen proton, there are two allowed. In a magnetic field, these nuclear dipoles precess around the *z*-axis. A thermal equilibrium is established with populations of dipoles spinning with and against the applied magnetic field. When suitable energy is given in the form of RF, a small fraction of these hydrogen nuclei can be excited and brought into phase coherence, precessing in the *x-y* plane. Over time, their orientations re-establish equilibrium with the magnetic field (B_o) at a rate given by the exponential time constant T1. They lose phase coherence with an exponential time constant known as T2. Their precessional rate is only dependent on the net local magnetic field experienced by the nucleus. T1 relaxation is thus governed by how quickly the nuclei exchange energy with the lattice or surrounding molecules, and T2 relaxation is governed by local magnetic field inhomogeneities.

Basic pulse sequences

I have purposely been vague up to this point as to the exact pulse sequences and gradients that are needed to establish this. So far, we have only given the example of a 90° RF pulse causing an FID.

A "bewildering" array of pulse sequences is available for MRI [30]. Slight variations on these sequences have led to various acronyms. Some pulse sequences are nearly synonymous with or identical to others but have been given different names by different authors. Spin echo (SE), inversion recovery (IR), short time inversion recovery (STIR), gradient-recalled acquisition in the steady state (GRASS), steady-state free precession (SSFP), Carr-Purcell-Meiboom-Gill (CPMG) sequence, to name only a few, are included in the current literature. On top of that, with each new pulse sequence modified by variations of gradients and acquisition times, equipment manufacturers have coined acronyms for their own particular use (Box 1).

We now examine the standard SE sequence that is at the heart of most conventional MRI. Other pulse sequences, such as IR and fluid-attenuated inversion recovery (FLAIR), are explained. Gradient-recalled echo and limited flip angle techniques that are variations of the SE pulse are also introduced. I limit discussion of the pulse sequences in this article based only on their ability to discriminate different tissue signal characteristics, including T1 and T2 relaxation. The length of this primer does not allow one to cover the breadth of MRI pulse sequences. Modifications of these sequences are also used to measure flow, phase, diffusion, and perfusion as well as to reduce artifacts and perform functional imaging. The interested reader is referred to the textbook *Neuroimaging, Clinical and Physical Principles* [31].

Table 5 is a summary of some of the most common pulse sequences used in MRI today. A basic understanding of the pulse sequences used to generate signals in the NMR experiment is necessary, because this lies at the heart of the data recorded. The pulse sequence can be thought of in three phases:

1. A preparation pulse to excite the tissue. The manner in which the tissue is excited, whether it is a short flip angle or large flip angle, has a significant impact on T1 contrast.
2. A time interval between excitation of the tissue and acquisition of the data. This is the period during which dephasing (T2 relaxation) occurs. A longer time increases T2 effect.
3. The overall time between data sampling, or TR. A long TR allows samples to recover, minimizing T1 contrast, whereas a short TR accentuates T1 contrast.

Spin echo pulse

A SE sequence is established as follows. RF energy is given to the system at the Larmour frequency with enough intensity to flip the magnetic vector into the *x-y* plane. This is the so-called "90° pulse." The vector then precesses in

Box 1. Acronyms

3D FASTER	Three-dimensional field echo acquisition with a short repetition time and echo reduction
3D GRE	Three-dimensional gradient echo
3D MPRACE	Three-dimensional magnetization prepared rapid gradient echo
ADC	Apparent diffusion coefficient
BASE	Basis imaging with selective inversion-prepared
bEPI	Blipped echoplanner imaging
BMS	Bulk magnetic susceptibility
BOLD	Blood oxygenation level-dependent contrast
BOSS	Bimodal slice select radiofrequency pulse
BP MR	Biphasic MRI
BW	Bandwidth
CBF	Cerebral blood flow
CBV	Cerebral blood volume
CE-FAST	Contrast-enhanced Fourier acquired steady-state technique
CNR	Contrast-to-noise ratio
CP	Cross-polarization
CPMG	Carr-Purcell-Meiboom-Gill (measurements of T2)
CSF	Cerebrospinal fluid
CSMEMP	Contiguous slice multiecho multiplanar
DIGGEST	Direct imaging of local gradients by group echo selection tomography
DISE	Driven inversion spin echo
DMSSFP	Double-mode steady-state free precession
DOPING	Double pulse interfaced echo imaging
DPSF	Diffusion perfusion snapshot flash
DSC	Dynamic susceptibility contrast
DWI	Diffusion-weighted imaging
EPC	Echo phase correction
EPI	Echoplanar imaging
EPISTAR	Echoplanar imaging and signal targeting with alternating radiofrequency
ETL	Echo train length
FAcE	Free induction decay acquired echoes
FAISE	Fast acquisition interleaved spin echo (which is the same as fast spin echo)
FAST	Fourier-acquired steady-state technique
FATS	Fat-suppressed acquisition with echo times and real times shortened
FC	Flow compensation
FE	Field echo, frequency encode
FEER	Field even echo rephasing
FFE	Fast field echo
FFF	Fast Fourier flow
FFP	Fast Fourier projection
FID	Free induction decay
FIRFT	Fast inversion recovery Fourier transform
FISP	Fast imaging with steady-state precession
FLAG	Flow-adjusted gradients
FLAIR	Fluid attenuation inversion recovery
FLASH	Fast low-angle shot
fMRI	Functional MRI
FONAR	Field focusing nuclear magnetic resonance
FOV	Field of view

FR	Frequency encode
FSE	Fast spin echo (turbo spin echo)
FT	Fourier transform
FWHM	Full-width at half-maximum
G	Gauss
GARP	Globally optimized alternating phase Rectangular pulse
GATORCIST	Respiratory gated imaging
Gd	Gadolinium
GINSEST	Generalized interferography using spin echoes and stimulated echoes
GMN	Gradient moment nulling
GMR	Gradient moment rephrasing
GRASE	Gradient spin echo
GRASS	Gradient acquisition in steady state
GRE	Gradient echo imaging
GREAT	Ghost reduction by equalized acquisition triplets
GROPE	Generalized compensation for resonance offset and pulse length errors
HASTE	Half-Fourier acquisition single-shot turbo spin echo
IR	Inversion recovery
IR-EPI	Inversion recovery echoplanar imaging
IVIM	Intra voxel incoherent motion
LFA	Limited flip angle
MAST	Motion artifact suppression technique
MBEST	Modulus blipped echoplanar single-pulse technique
MBS-MRA	Minimum basis set magnetic resonance angiography
MEMP	Multiecho multiplanar
MESS	Multiple echo single shot
mFISP	Mirrored fast imaging with steady-state precession
MIP	Maximum intensity projection
MOTSA	Multiple overlapping thin slab acquisition
MPGR	Multiplanar gradient recalled
MPIR	Multiplanar inversion recovery
MPRAGE	Magnetization prepared rapid gradient echo
MR	Magnetic resonance
MRA	Magnetic resonance angiography
MRI	Magnetic resonance imaging
MS-EPI	Multishot echoplanar imaging
MSIT	Multiple slab imaging technique
MT	Magnetic transfer
MTC	Magnetization transfer contrast
MTR	Magnetization transfer ratio
MTSA	Multiple thin slab acquisition
NEX	Number of excitations
NMR	Nuclear magnetic resonance
NSA	Number of signal averages
PAIR	Partial volume-sensitized inversion recovery
PC	Phase contrast
PE	Phase encoding
PEDD	Proton-electron dipole dipole
PEG	Phase encode grouping
PGSE	Pulsed gradient spin echo
PIETIR	Prolonged inversion and echo time inversion recovery

(*continued on next page*)

POMP	Phase-ordered multiplanar
PPG	Peripheral pulse gating
PPM	Parts per millions
PRE	Proton relaxation enhancement
PRFT	Partially relaxed Fourier transform
PSIF	Mirrored fast imaging with steady precession
PT2	Preferential T2
QCSI	Quantitative chemical shift imaging
QMRI	Quantitative MRI
QUIPSS	Quantitative imaging of perfusion using a single subtraction
RACE	Real time acquisition and evaluation of motion
RAM FAST	Rapid acquisition matrix Fourier acquired steady-state technique
RARE	Rapid acquisition relaxation enhanced
RARE	Rapid acquisition with refocused echoes
RASE	Rapid acquisition spin echo
RBC	Red blood cell
rCBF	Regional cerebral blood flow
RF	Radiofrequency
RF-FAST	Radiofrequency Fourier-acquired steady-state technique
ROI	Region of interest
ROPE	Respiratory ordered phase encoding
RUFIS	Rotating ultrafast imaging sequence
SAAV	Simultaneous acquisition of artery and vein
SAR	Specific absorption rate
SAT	Saturation pulse
SD	Standard deviation
SE	Spin echo
sEPI	Spiral echoplanar imaging
SIMUSIM	Simultaneous multislice imaging
SIP	Saturation inversion projection
SMART	Simultaneous multislice acquisition using rosette trajectories
SmaRT	Simulataneous multislice acquisition with arterial-flow tagging
SMI	Simulataneous multislice imaging
SNR	Signal-to-noise ratio
SPACE	Spatial and Chemical-shift encoded excitation
SPAMM	Spatial modulation of magnetization
SPECT	Single photon emission computed tomography
SPGR	Spoiled gradient recalled (spoiled gradient acquisition in steady state)
SPIR	Selective population inversion recovery
SS	Slice select gradient
SSFP	Steady-state free precession
SSP	Section-sensitivity profile
STE	Stimulated echo
STIR	Short tau (inversion time) inversion recovery
STREAM	Suppressed tissue with refreshment angiography method
T	Tesla
T2 FFE	T2 fast field echo
T2 PEDD	T2 proton electron dipole dipole interaction
T2 PRE	T2 proton relaxation enhancement
TCF	Time correlation function
TD	Trigger delay
TE	Time delay between excitation and echo maximum

TEI	TE interleaved
TFE	Turbo field echo
TI	Time following inversion pulse
TMR	Topical magnetic resonance
TOF	Time of flight
TONE	Tilt optimized nonselective excitation
TOSS	Total suppression of sidebands
TPPI	Time-proportional phase incrementation
TR	Time to repetition
TRICKS	Time-resolved imaging of contrast kinetics
TSE	Turbo spin echo
TSR	Total saturation recovery
Turbo FLASH	Turbo fast low-angle-shot
URGE	Ultra rapid gradient echo
USPIO	Ultra small superparamagnetic Iron oxide
VAS	Variable angle spinning
VEMP	Variable echo multiplanar
VENC	Velocity encoding value
VIGRE	Gradient echo
VINNIE	Velocity encode cine imaging
VOI	Volume of interest
VPS	Views per segment
WATERGATE	Water suppression pulse sequence
WEFT	Water-eliminated Fourier transform

the *x*-*y* plane in a coherent fashion. Over a short period, the individual nuclei comprising the net vector drift out of phase. The signal rapidly decays as an FID. If the receiver coil were turned on at this time, a sinusoidal wave of rapidly decreasing intensity would be produced (ie, an FID). A certain time later (1–100 milliseconds in imaging), a second RF pulse is given, which now corresponds to a 180° pulse. The vectors are inverted, which causes them to spin in the opposite direction. Fast-spinning protons are now behind the slower protons, and phase coherence can be re-established for those protons that became out of phase because of static magnetic field inhomogeneities. Fig. 25 displays the SE pulse sequence in which the magnetization is deflected into the *x*-*y* plane, loses phase coherence and is then inverted by a 180° pulse, changes rotational direction, and is rephased. Over a period equal to the time between the 90° and 180° pulses, phase coherence is re-established and signal is generated as an echo. The data are then acquired. The total elapsed time from the 90° pulse to the echo is called the TE, or "time to echo." This is the prototype SE, or Hahn echo [32], described only a few years after the discovery of NMR.

The entire pulse sequence is repeated many times in a typical experiment. Several averages or number of excitations (NEXs) may be obtained to increase the signal-to-noise ratio. Multiple phase-encoding steps are taken to achieve spatial localization. The time for which the pulse sequence is repeated is called the TR, or "time of repetition." Fig. 26 shows the entire pulse sequence. Image contrast is a function of the timing parameters chosen, TE, TR, and tissue-specific properties [33–35]. All image contrast has some effects from T1, T2, and proton density; therefore, sequences are designated as being "weighted" toward a given parameter.

Proton density weighting

Consider first the consequences of altering the TR. Assume that the TE is taken to be as short as possible to reduce T2 or dephasing effects. If a long TR is used, all the magnetization will have returned to the *z*-axis. At the start of the next pulse train, it will be available for deflection into the *x*-*y* plane. This gives maximum signal, and the relative signal intensities of tissues are based not on the relative T1 relaxation characteristics but on how much hydrogen there is (ie, proton density),

Table 5
Common pulse sequences used in MRI

Acronym	Pulse sequence	TE	Range	TR	Range	Flip	TI	Contrast effect
SE	Spin-echo	Short	5–20	Long	200–600	90°	None	T1W
		Short	10–20	Short	2000–4000	90°		Proton
		Long	40–200	Long	2000–4000	90°		T2W
CPMG	Multi-echo	Short	20–60	Long	2000–4000	90°	None	Proton and T2W
		Long	80–200	>2000 milliseconds				
GRASS	Gradient echo	Short	2–20	Short	10–50[a]	45°	None	Proton/steady state
		Long	5–40	Short	10–50	<20°		T2*W/steady state
		Short	5–10	Long	400–800	45E–90°		T1W
SPGR	Spoiled grass	Short	2–10	Short	5–500[a]	45–90	None	T1W
IR	Inversion recovery	Minimum	10–20	Long	2000–4000	180°	Medium	Heavy T1W
		Short		>2000 milliseconds			600 milliseconds	
STIR	Short time inversion recovery	Long	50–120	Long	2000–4000	180°	170 milliseconds	T1W and T2W
				>3000 milliseconds			Short	are additive, suppresses fat
FLAIR	Fluid-attenuated inversion recovery	Long	80–200	Very long	4000–8000	180°	2000 milliseconds	T2W with
		150 milliseconds		6000 milliseconds			Long	attenuation of free water

[a] Depends on flip angle.

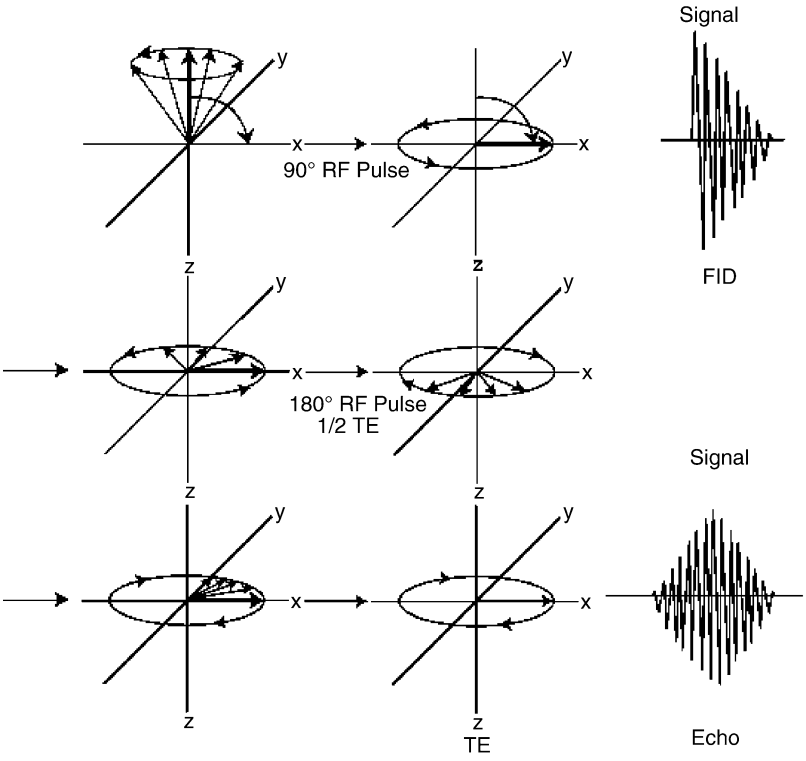

Fig. 25. Magnetic vector diagram of standard spin echo sequence. The incoherent precessing vectors are brought into coherence, and the net vector is tipped into the *x*-*y* plane. A free induction decay (FID) occurs. After a short time, the vectors begin to dephase. A 180° radiofrequency (RF) pulse is then applied, inverting the vectors and reversing their direction. After a period of time has elapsed (echo time [TE]), the vectors rephase and an echo is produced.

as illustrated in Fig. 27. Proton density contrast is often misunderstood or ignored. Wehrli et al [36] demonstrated that most of the contrast seen between gray and white matter on T2W SE sequences can be ascribed to differences in proton density: gray matter has more water protons than white matter. Furthermore, to achieve maximum tissue contrast, the selection of pulse sequence to be used is highly dependent on hydrogen spin density. As the ratio of spin densities increases between two substances, SE becomes a better pulse sequence than IR [37].

T1 weighting

Suppose, however, that only a short time is allowed for the magnetization to recover to the *z*-axis. Only those substances that have extremely short T1s will have achieved their full potential magnetization before being pulsed with a repeat pulse, as illustrated in Fig. 28. The pulse sequence then becomes T1W, allowing for differential intensities to be observed between substances that have differing T1 values. The equation describing just the recovery of longitudinal magnetization as a function of time is: Magnetization = Mz $(1 - e^{-TR/T1})$, where Mz is the total net magnetic vector in the *z*-axis before 90° excitation, TR is repetition time, and T1 is a constant for each tissue. The time for complete relaxation is infinity. For 99% recovery, one must wait 4.6 times T1, as shown previously in Fig. 15. Obviously, most of the relaxation occurs within the first 2.0 times T1. Different tissues and substances have characteristic relaxation rates specific to that individual material. Furthermore, as was discussed earlier, T1 relaxation is also dependent on magnetic field strength. To optimize tissue contrast between voxels containing elements of different T1 relaxation values, one should thus know what the relaxation rate for a given tissue is. In Fig. 29, a family of curves of tissues with

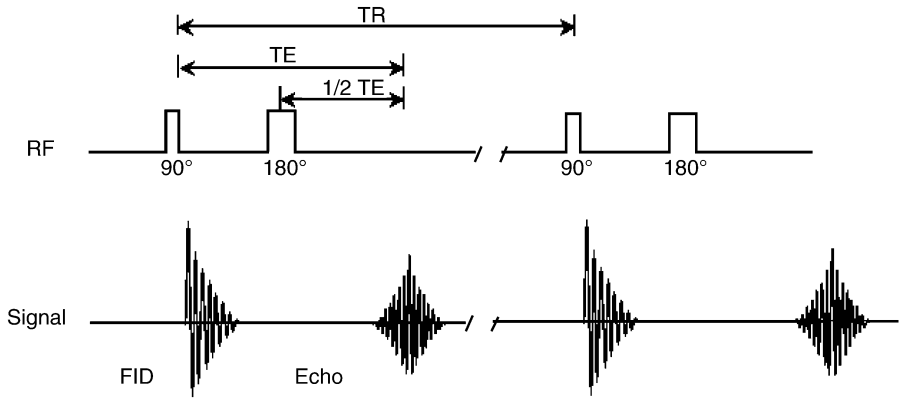

Fig. 26. Standard spin echo (SE) timing diagram. This figure demonstrates the radiofrequency (RF) pulse timing and associated signal from a standard SE sequence. A 90° pulse is given, followed by a 180° RF refocusing pulse at ½ echo time (TE). A period of time (repetition time [TR]) then elapses, and the entire process is repeated. An FID (free induction decay) occurs after the 90° pulse but the signal is actually acquired at the echo.

different T1 relaxation values is illustrated to discriminate between fat and white matter which have short T1s, a short is used. To achieve maximal contrast between tumor and CSF, then a longer TR would be best. In general, one should select a TR close to the T1 value of the tissue of interest. This ensures the widest possible separation between tissues with close T1 values.

T2 weighting

The SE sequence can also be used to acquire T2W data. In this instance, the TR between pulses is set quite long so that as much of the longitudinal magnetization as possible can recover (ie, no T1 effects). The time before data acquisition is now lengthened, however. The 180° pulse is given at a much later time, allowing for increased dephasing to occur. Only those tissues with long T2s (ie, those that dephase very slowly) have enough residual phase coherence available so that when the 180° pulse is applied, they can be brought back into phase. Because of phase losses incurred from non-static magnetic field inhomogeneities, only a fraction of the initial magnetization vector can be recovered. By necessity, less and less signal is acquired as TEs are lengthened and images become noisier. Fig. 30 illustrates this pulse sequence.

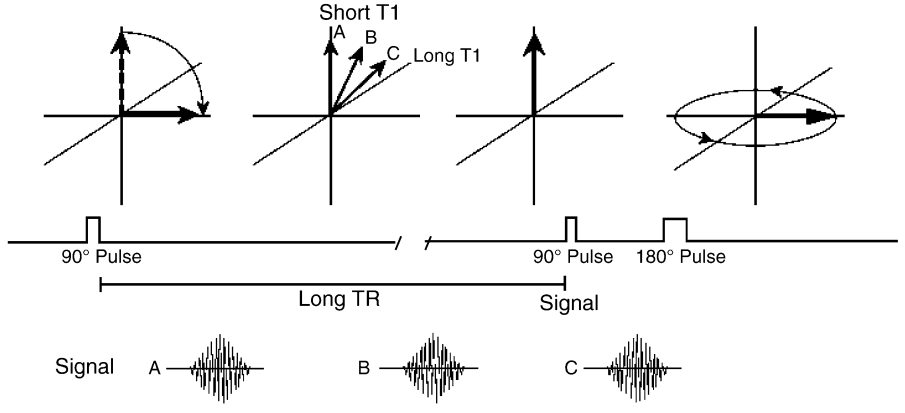

Fig. 27. Proton-weighted sequence. A 90° radiofrequency pulse is given. A long time (repetition time [TR]) elapses, and all the tissues (A, B, and C) relax to the ground state. When the next 90° pulse is given, 100% of the magnetization is available to tip again into the *x*-*y* plane. Therefore, maximum signal is achieved. Only if the materials have a different proton density (ie, quantity of available mobile hydrogen) is there a difference in signal between the three tissues.

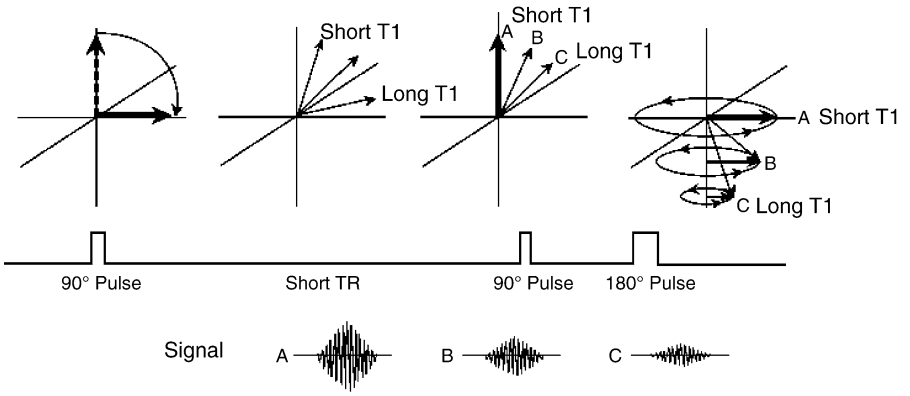

Fig. 28. T1-weighted pulse sequence. A 90° radiofrequency pulse is given, and a short time elapses before repeating the process. Tissue A with a short T1 has relaxed to the ground state, giving a maximum vector when reflipped into the *x-y* plane. Tissue C with a long T1 has not relaxed to the ground state, however. When the tissue is given a new 90° pulse, only a small vector is produced, creating substantially less signal intensity. In this pulse sequence, tissues with a short T1 relaxation time (TR) are the brightest.

Substances that have prolonged T2 values include free water, such as CSF, edema, cysts, and most pathologic processes in which tissue injury has occurred. T2W images, although having a lower signal-to-noise ratio than T1W images, are still the most useful for diagnostic neuroimaging [36].

Carr-Purcell-Meiboom-Gill sequence

The CPMG sequence [38,39] is a commonly used variation of the SE pulse sequence. In fact, most T2W SE sequences use this technique to acquire proton and T2W images simultaneously. The first part of this pulse sequence is exactly like

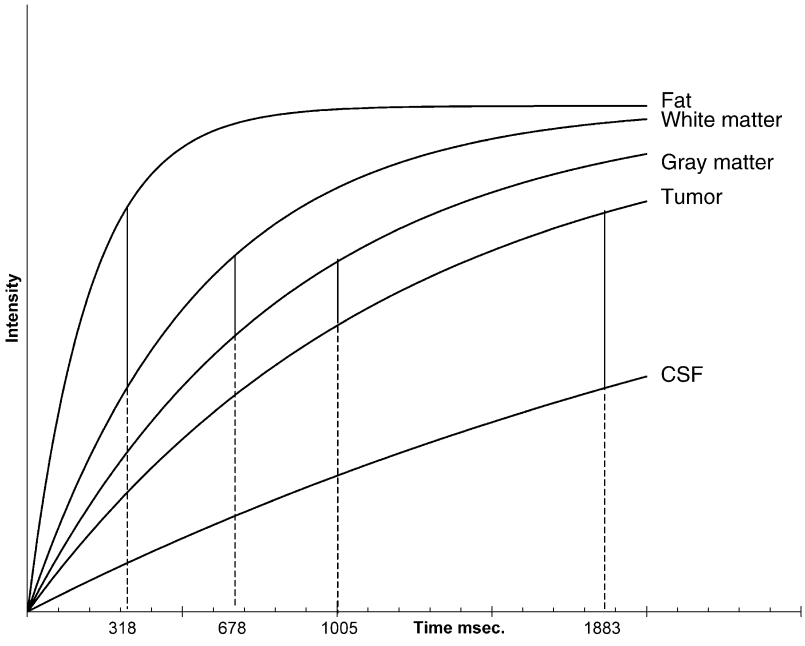

Fig. 29. Relaxation curves for different tissues, A through E. The optimal time to discriminate between fat and white matter would be at 318 milliseconds. In other words, a short repetition time (TR) is best to discriminate between tissues of short T1 values. A longer TR would be better to discriminate between tissues of longer T1 values, such as tumor and cerebrospinal fluid; in this case, 1883 milliseconds at 1.5-T field strength. CSF, cerebrospinal fluid.

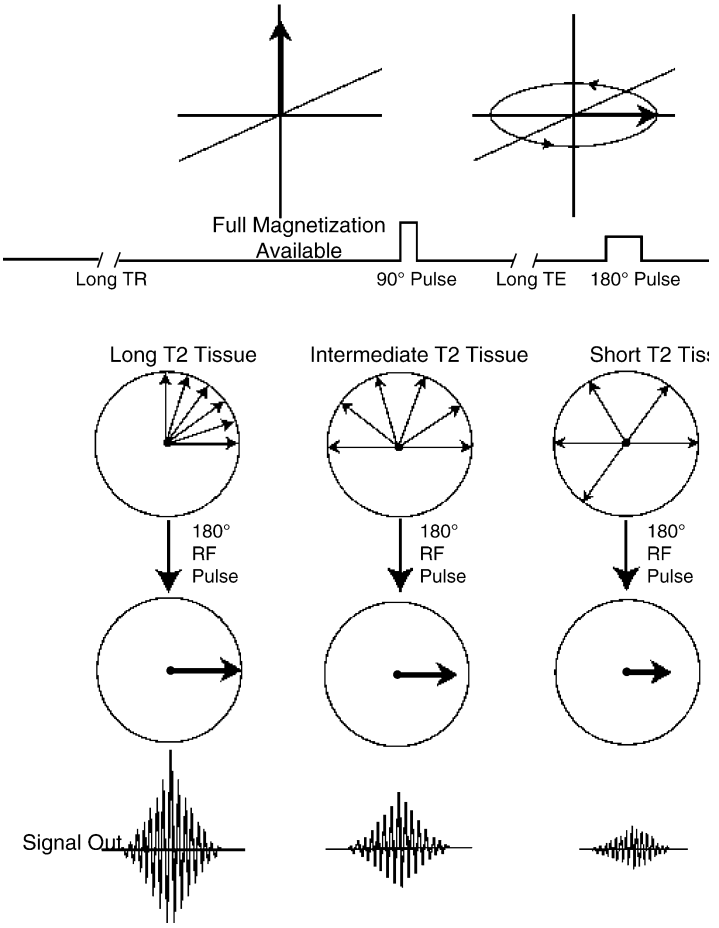

Fig. 30. T2-weighted spin echo pulse. A long repetition time is used such that all the magnetization is available before tipping into the *x*-*y* plane. The time before the 180° refocusing pulse is relatively long (ie, a long echo time [TE] is used). For tissues with long T2 relaxation, most of the signal remains coherent. For those with a short T2 relaxation time (TR), only a small amount of the signal is recovered with the 180° radiofrequency (RF) pulse.

the SE sequence that we have previously described. Soon after the first echo is produced, there is rapid dephasing of the proton spins and signal is lost. A second or third 180° RF pulse can then be applied, which reverses the spinning vectors and brings them back into phase. Because of T2 relaxation caused signal loss in the tissue, all of the signal cannot be rephased. Thus, our signal progressively gets smaller and smaller with each echo. This echo train, as illustrated in Fig. 31, is a curve fitted by plotting the maximum signal intensities at each echo and represents the true T2 relaxation curve for the tissue. The rapid T2 decay for the FID of each echo is the result of true tissue T2 and dephasing from static magnetic field inhomogeneity. Together, these are called T2*.

Inversion recovery

There are several types of inversion recovery (IR) pulses, which are variations on a theme but have significantly different appearances in terms of image contrast [40] and can be used for a wide variety of clinical applications. These are discussed separately as conventional IR, short-time inversion recovery (STIR), and fluid-attenuated inversion recovery (FLAIR).

Conventional inversion recovery

In the usual IR pulse sequence [34], a 180° pulse is given, which rotates the magnetization vector into the negative *z*-direction, as shown in Fig. 32. Note that this requires twice the RF power

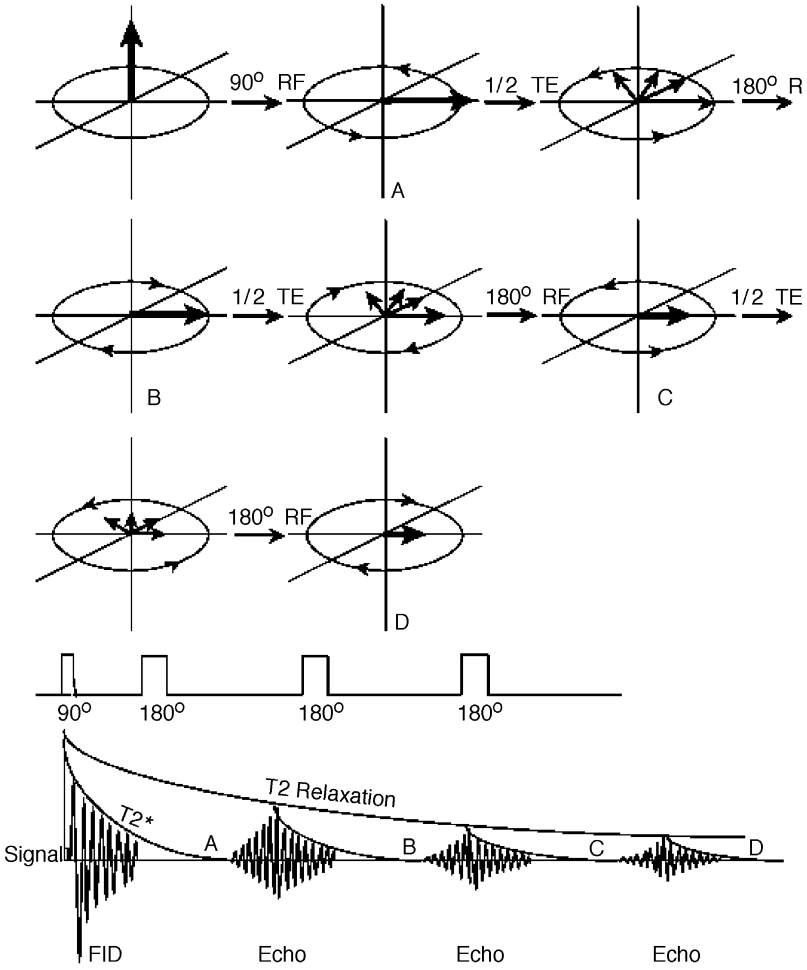

Fig. 31. Carr-Purcell-Meiboom-Gill sequence. This sequence applies a series of refocusing 180° radiofrequency (RF) pulses with repeated echoes. A curve of signal decay can be traced, giving the T2 relaxation of the substance. FID, free induction decay; TE, echo time.

and that it also requires a longer time to recover to the steady-state positive *z*-direction. This is governed by the exponential decay time constant, T1. If TR is assumed to be extremely long relative to T1, the equation describing T1 relaxation can be shown to be: Signal = $S_o\,(1 - 2e^{TI/T1})$, where S_o is the total *z*-component of the magnetic vector, TI is the time to inversion, T1 is the familiar relaxation constant (which is tissue dependent) [33], and TR is repetition time.

Fig. 33 shows the typical way in which the signal intensity from an IR pulse sequence is plotted as a function of time. After inversion, as the magnetization vectors begin returning to the *z*-axis, those with short T1s do so first. At a time called TI, a 90° pulse is given. If this is performed

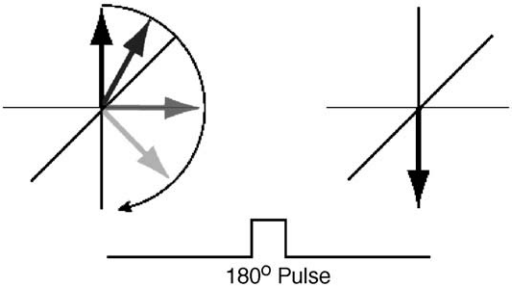

Fig. 32. Inversion recovery pulse sequence. With a 180° radiofrequency pulse, the magnetization vector is rotated 180° to the negative *z*-direction.

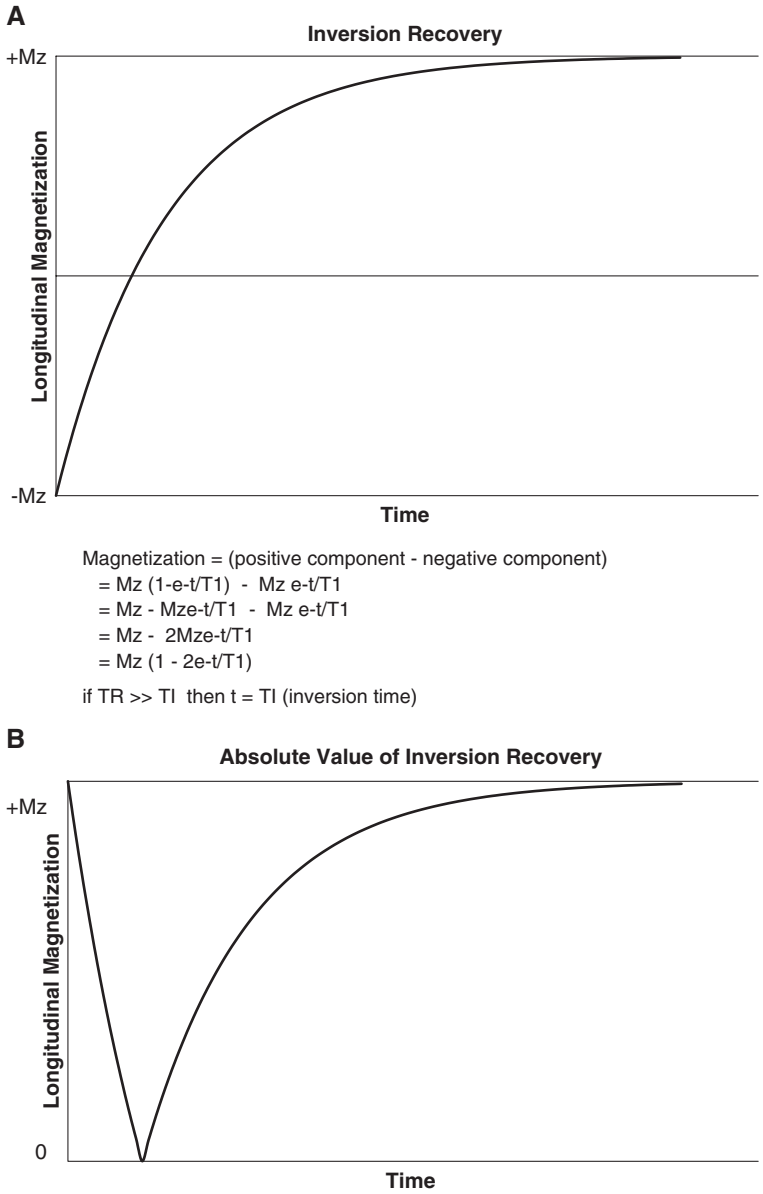

Fig. 33. Inversion recovery (IR) signal reconstruction. (*A*) Exponential recovery of magnetization after IR pulse. IR has a negative and positive signal component. (*B*) Magnitude reconstruction of the IR pulse. When the data are analyzed by the computer, only the absolute value of the signal is usually taken. Thus, signal intensity for a given substance initially decreases, reaches a null point, and then progressively returns to full magnetization when the vector reaches the positive *z*-axis. TR, repetition time.

when the protons with short T1s have recovered to the positive *z*-direction (~500–1000 milliseconds), they are then flipped into the *x*-*y* plane to produce signal. The net vector of the slower relaxing nuclei (which has perhaps only recovered to the *x*-*y* plane at the time of the 90° pulse) is returned to the negative *z*-direction and produces no significant signal in the FID. Thus, only protons with short T1s have recovered and are brought into the *x*-*y* plane to have their signals sampled. Sampling occurs by using another rephasing 180° pulse just like the SE technique, and

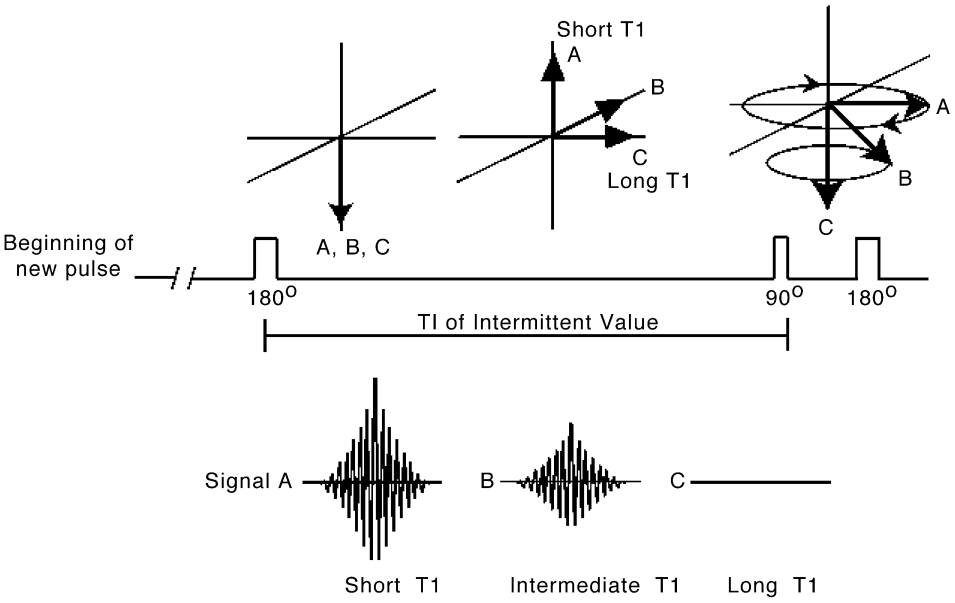

Fig. 34. Conventional T1-weighted inversion recovery pulse sequence. A 180° radiofrequency (RF) pulse is given, inverting the vectors of tissues A, B, and C. After a period called the time to inversion (TI), tissues with short T1s, such as those labeled A, have largely returned to the *z*-axis. Tissues with long T1s, such as those labeled C, are now in the *x-y* plane. A 90° RF pulse is applied, followed in short succession by sampling of the echo with a 180° pulse. The effect of this is to rotate the vectors of tissue A into the *x-y* plane and give maximum signal intensity. Those tissues with longer T1s, such as those labeled C, give little signal intensity.

the echo is then sampled a short time (½ TE) later. This is sometimes called an inversion recovery spin echo pulse sequence [41]. In general, for a T1W sequence, parameters are chosen such that the TI is approximately equal to the T1 of the tissue of interest. This ensures that most of the dipoles have recovered to the *z*-axis; if you wait too long, all the vectors recover, yielding no contrast. For brain, the T1 of white matter is ≈500 to 600 milliseconds at 1.5 T. A minimum TE is used to reduce T2 weighting. This pulse sequence is illustrated in Fig. 34. The second 180° pulse is given to rephase the protons and recover signal lost from static field inhomogeneity. It also facilitates data collection, because the necessary phase-encoding and frequency-encoding gradients needed for two-dimensional (2D) image reconstruction can be applied.

If a long TE is chosen (ie, the sample is allowed to dephase for a significant time before the second 180° pulse is given), the sample becomes T1W and T2W. This has self-negating effects. The tissues are sampled such that only protons that have short T1s are detected; they are then dephased, giving low signal.

Inversion recovery imaging with a repetition time that is short

For T1 contrast to be achieved, a fairly long TR is needed. Consider, for instance, what happens if not enough time is allowed before the process is repeated. Let's assume that after all the pulses, the vectors with short T1s are now beginning to align with the *z*-axis. Those with longer T1s are precessing just above the *x-y* plane, however. If these protons are reirradiated with a 180° pulse, as illustrated in Fig. 35, the vectors with short T1s are inverted to the negative *z*-axis. Those with longer T1s are now precessing in the *x-y* plane. After a period, the short T1 protons will have caught up with the longer T1 protons, they will both be in the *z*-plane at the time the next 90° pulse is given, and both will be inverted into the *x-y* plane and give signal. Thus, no contrast is achieved. With IR, the TR must long.

As discussed in later sections, the TR is a major determinant of total imaging time. Although spectacular T1W images can be obtained using IR, the imaging time required is significantly longer than with SE technique. The T1W IR

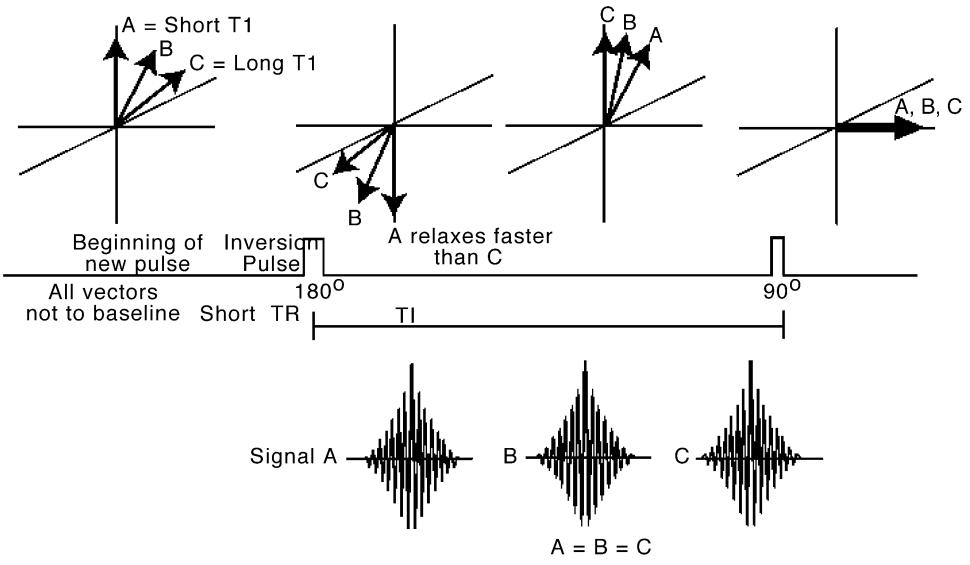

Fig. 35. Inversion recovery (IR) with a short repetition time (TR). What happens if the TR is too short? At the beginning of the sequence, the tissues have not fully relaxed. When they are inverted, the slower relaxing tissues have not fully relaxed. When they are inverted, the slower relaxing tissues, such as those labeled C, are ahead of those with a short T1. When the tissues are sampled at the time to inversion (TI) with a 90° pulse, there is no contrast between them. For this reason, the TR must be long with IR sequences.

image of the brain illustrated in Fig. 36 required 17 minutes, whereas the SE T1W image of the same patient illustrated in Fig. 37A took only 5 minutes for the same NEX. Fig 37B shows an IR fast sequence with a multiecho acquisition that took only 2 minutes. Consequently, IR sequences are rarely used for routine T1W imaging unless they are used in conjunction with newer fast SE technology. They find special application in the imaging of myelination of the brain in young infants and other areas in which optimum T1 contrast is desired. They are useful in evaluating multiple sclerosis plaques for neuronal dropout (holes). No other pulse sequence routinely gives such excellent T1W contrast [42]. The dramatic T1 contrast achieved in IR results from the fact that a full range of 180° is available in which to spread out the longitudinal magnetization rather than just 90° as in SE (ie, there is more dynamic range for T1 contrast) [43].

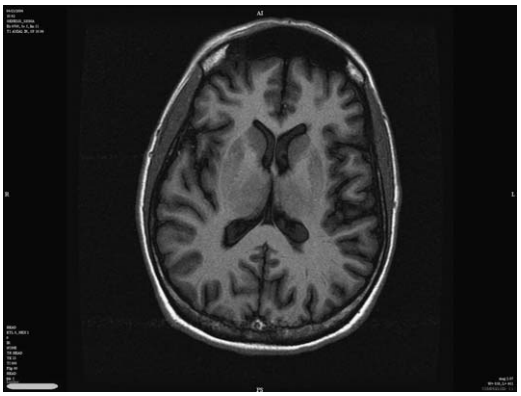

Fig. 36. T1-weighted inversion recovery image of the brain (17 minutes).

Short time inversion recovery imaging

STIR imaging allows only a short time between the 180° pulse and the second 90° pulse. In this variant of IR, the second 90° pulse is applied when a tissue of interest has reached the null point. At short inversion times, all the magnetization vectors precess in the negative z-direction. When the 90° pulse is given, bringing them into the x-y plane, signal is generated. The fact that the vectors are in the positive z- or negative z-direction before the 90° pulse is of no consequence, because the computer registers magnitude only and not the sign of the signal. Note, however, that for a tissue with a given T1, at a certain time

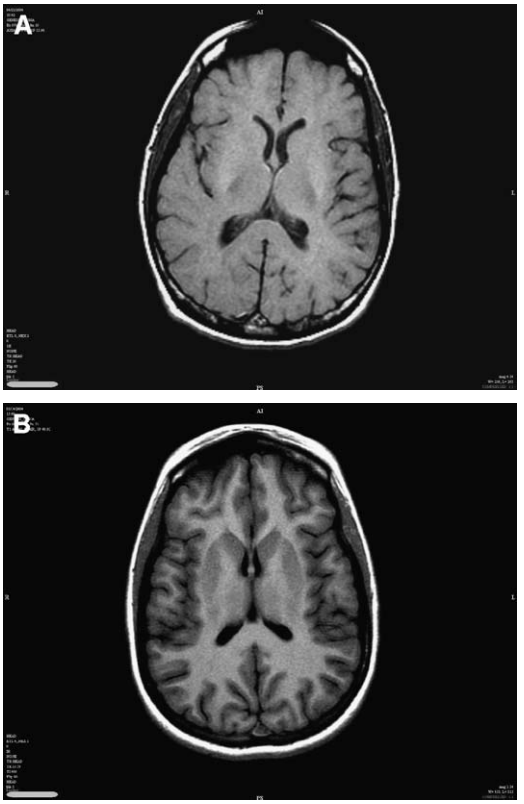

Fig. 37. (*A*) T1-weighted (T1W) spin echo (SE) image of the brain (5 minutes). (*B*) T1W fast inversion recovery image of brain with fast SE technology required only 2 minutes.

(when TI = T1 × 0.693), it will have recovered to the *x-y* plane just as the second 90° pulse is given: Signal = S_o $(1 - 2e^{-TI/T1}) = 0$. This is illustrated in Fig. 38 for the tissue labeled A. When this occurs, it now precesses in the negative *z*-direction without transverse magnetization; hence, no signal is generated. The signal of A is then effectively nulled.

In STIR imaging, the inversion pulse is chosen such that a material with a short T1 is nulled; by this means, the signal from that substance can be suppressed. To suppress fat, for instance, a TI of 173 milliseconds (at 1.5 T) is chosen (0.693 × 250 milliseconds [T1 of fat]). If an appropriate TE is chosen for data collection, the effect of T1 and T2 on lesion detection can be additive. The T1 and T2 of most pathologic lesions are prolonged [44]. A longer TE is used before data collection; therefore, only those substances that have long T1s and long T2s are bright (hence, additive contrast effects). This can be used to significant advantage in areas like the orbit [45–47], where the adjacent bright fat can obscure detection of lesions of the optic nerves. Fig. 39A is a normal STIR image of the orbit demonstrating excellent fat suppression. Notice that the optic nerve is of lower signal intensity than the extraocular muscles. The STIR image of Fig. 39B from a different patient demonstrates the effectiveness of this pulse sequence to show optic neuritis. The bright signal of the conal fat is well suppressed, whereas the edema of the optic nerve is seen. Fig. 39C shows optic nerve enhancement, confirming the diagnosis of optic neuritis. STIR can also effectively suppress fat within the vertebral bodies so as to evaluate bony lesions, such as metastasis (Fig. 40**)**. Newer chemical saturation pulse sequences are also highly effective at suppressing fat [48]. Furthermore, STIR not only suppresses fat but any short T1 substance, such as hemorrhage or gadolinium enhancement [49].

Fluid-attenuated inversion recovery

One of the most exciting pulse sequences to be applied to neuroradiology in the past several years is FLAIR. FLAIR is really a variation of STIR imaging. It might be considered a long time inversion sequence with a long TE. A 180° RF inversion pulse is applied. Before the next 90° pulse is applied, a long time is given to allow substances, such as fluid, with long T1s to recover to the *x-y* plane (Fig. 41). When the 90° pulse is given, substances with long a T1, such as free water, are inverted to the negative *z*-axis. Substances with short a T1 have recovered completely before this pulse and thus give maximum signal when data sampling occurs. As such, this sequence effectively nulls out free water much as a STIR sequence can be used to null out fat.

This sequence can be particularly helpful in evaluating periventricular white matter lesions (Fig. 42). Water bound to complex macromolecules within plaques has a relatively shorter T1 than the free water within the ventricles [50]. The long inversion time effectively suppresses free water; therefore, the CSF is nulled. Lesions that contain complex partially bound water (which is less mobile) have a shorter T1 than free water and are not nulled. These protons are analogous to water bound to proteins. Furthermore, a fairly long TE is used. This results in a heavily T2W sequence. As a result, the sequence becomes additive for contrast effects of tissues with

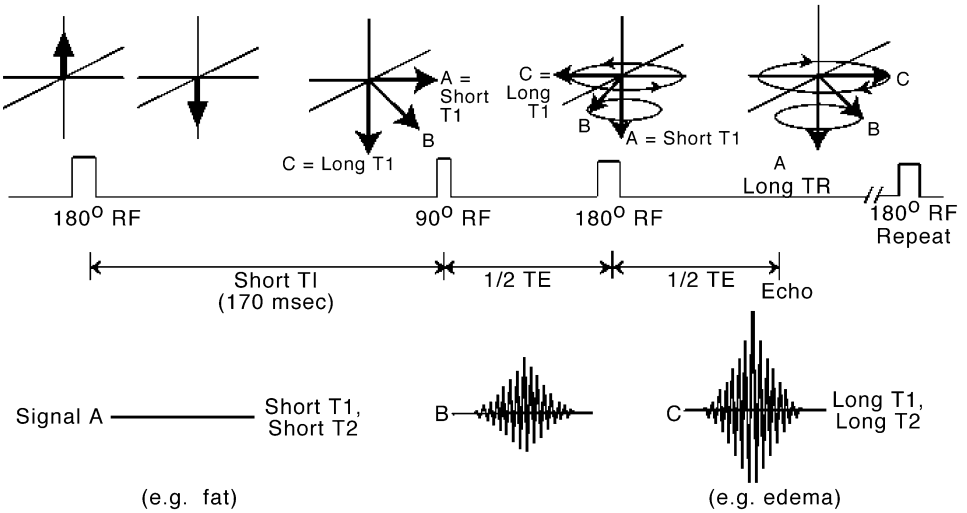

Fig. 38. Short time inversion recovery (STIR) sequence. In this case, a 180° radiofrequency (RF) pulse is given. A relatively short time is allowed for the tissues to relax. At this point, tissues with short T1s, such as those labeled A, are in the *x*-*y* plane. The 90° pulse given at the end of the inversion time now rotates substances with short T1s into the *z*-axis, which gives no signal from tissue A and maximum signal from tissue C when sampled by the 180° refocusing RF pulse. In this sequence, the contrast effects of T1 and T2 are additive. A long T1 and a long T2 produce maximum signal intensity. TE, echo time; TR, repetition time.

prolonged T2 and shortened T1 (eg, white matter lesions). Long inversion times of 2000 milliseconds or greater require long TRs of 6000 milliseconds or greater. This technique is prohibitively long for most conventional imaging; however, coupling this sequence with a fast image acquisition technique [51–53] results in good-quality images in a reasonable period of 2 to 3 minutes.

FLAIR is effective at highlighting lesions like demyelination [54], stroke, ischemic gliosis [55–57], and tumor. It is a highly sensitive technique (more so than SE) [51]; however, it is nonspecific. Even normal partially myelinated white matter tracts are highlighted. The protein-rich pituitary stalk is also normally bright on FLAIR [58]. In Fig. 43, an example of FLAIR in a patient with venous infarcts of the thalami from cerebral vein thrombosis demonstrates its dramatic and positive contrast compared with fast SE T2W images. FLAIR is more sensitive for the detection of acute infarcts. In addition, old infarcts with areas of cystic encephalomalacia can be distinguished from acute infarcts [59]. The suppression of free water greatly augments the ability of the viewer to detect underlying lesions. FLAIR has also been used effectively in evaluating subarachnoid hemorrhage by removing interfering CSF signal.

In an elegant comparative clinical study, Hittmair et al [50] concluded that the fast STIR sequence was clearly superior to other techniques, such as conventional SE, fast SE, and FLAIR, for the detection of cervical cord multiple sclerosis plaques. This is somewhat surprising, given the high sensitivity of FLAIR for evaluation of multiple sclerosis in the brain. In the cervical spine, CSF flow artifacts and incomplete suppression of CSF signal, combined with poor lesion contrast, reduce the utility of FLAIR, however. A STIR study with a TR of 2200 millisecond, effective TE (TEeff) of 50 millisecond, TI of 110 millisecond, echo train length of 8, and NEX of 6 was determined to be the most effective.

Notice that in contradistinction to the STIR sequence, positive contrast is additive for tissues with short T1 and long T2 in this sequence in comparison to STIR, in which long T1 and long T2 tissue contrast is augmented. This means that the FLAIR sequence is more sensitive for lesions in which bound water is highlighted. It might be thought of as a situation in which the cup is half empty or half full. Overall, pathologic tissues have longer T1s than normal tissue; however, a subcomponent of the lesion has T1s that are shorter than the free water within the lesion. When the

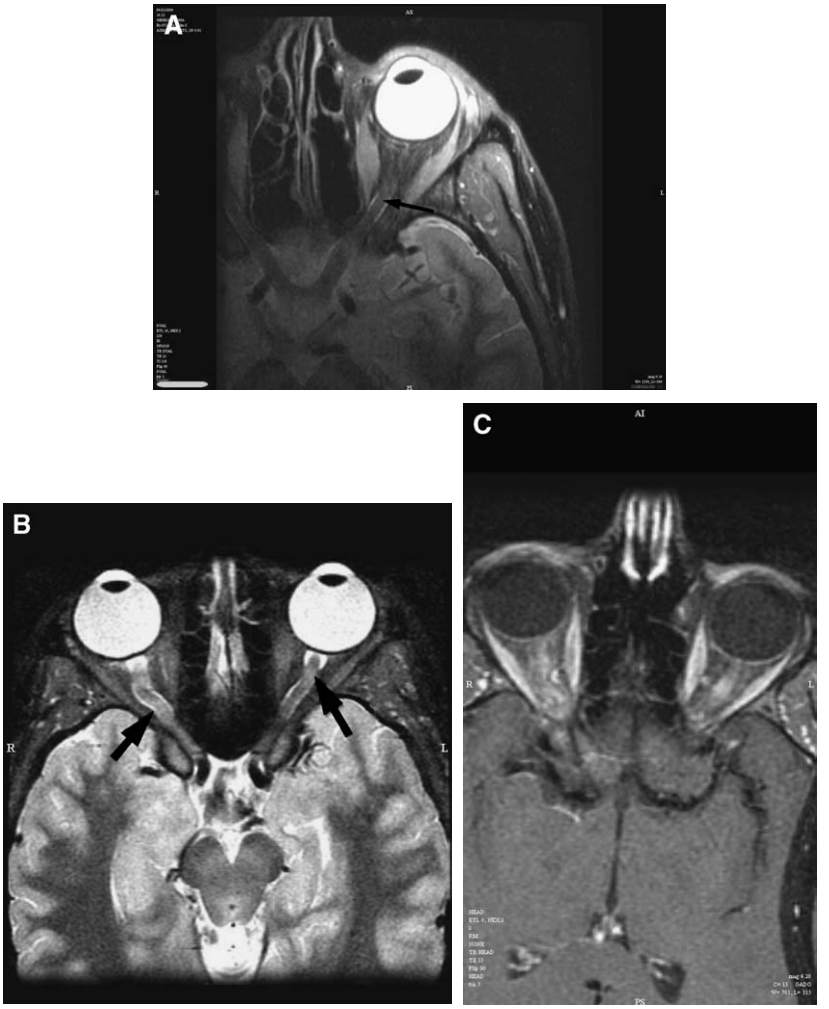

Fig. 39. (*A*) Normal optic nerve (*arrows*) with short time inversion recovery (STIR) has signal intensity less than muscle (*arrowheads*). (*B*) In a different patient with bilateral optic neuritis, there is increased signal intensity in the optic nerves bilaterally. Note that the signal intensity of the optic nerves exceeds that of the extraocular muscles (*arrows*). (*C*) Same patient as in Fig. 39B. Axial T1-weighted, fat-suppressed, gadolinium-enhanced images of the orbits reveal bilateral optic nerve enhancement, confirming the diagnosis of optic neuritis. The STIR images are complimentary, showing edema of the optic nerves. Notice that the STIR images in Fig. 39B give excellent suppression of the orbital fat.

additive effect of T2 contrast is present, highly structured water, such as that in normal brain, rapidly decays, whereas the gliotic lesions remain bright, giving relative high signal intensity. A model of this is given in Fig. 44. A gliotic lesion is represented by an interstitial matrix of loosely associated water and glial cells as well as increased free water content. After application of the long IR sequence, the free water is suppressed, whereas the bound water still has signal. FLAIR sequences give a brighter signal than adjacent brain while suppressing unwanted signal from CSF. FLAIR can be helpful in discriminating dilated perivascular spaces (free water) from white matter lesions (gliosis with bound water) (Fig. 45).

Chemical selective saturation

We have just seen how the pulse sequence can be designed to null the signal of a given tissue based on its relaxation characteristics. There is a second powerful technique that allows

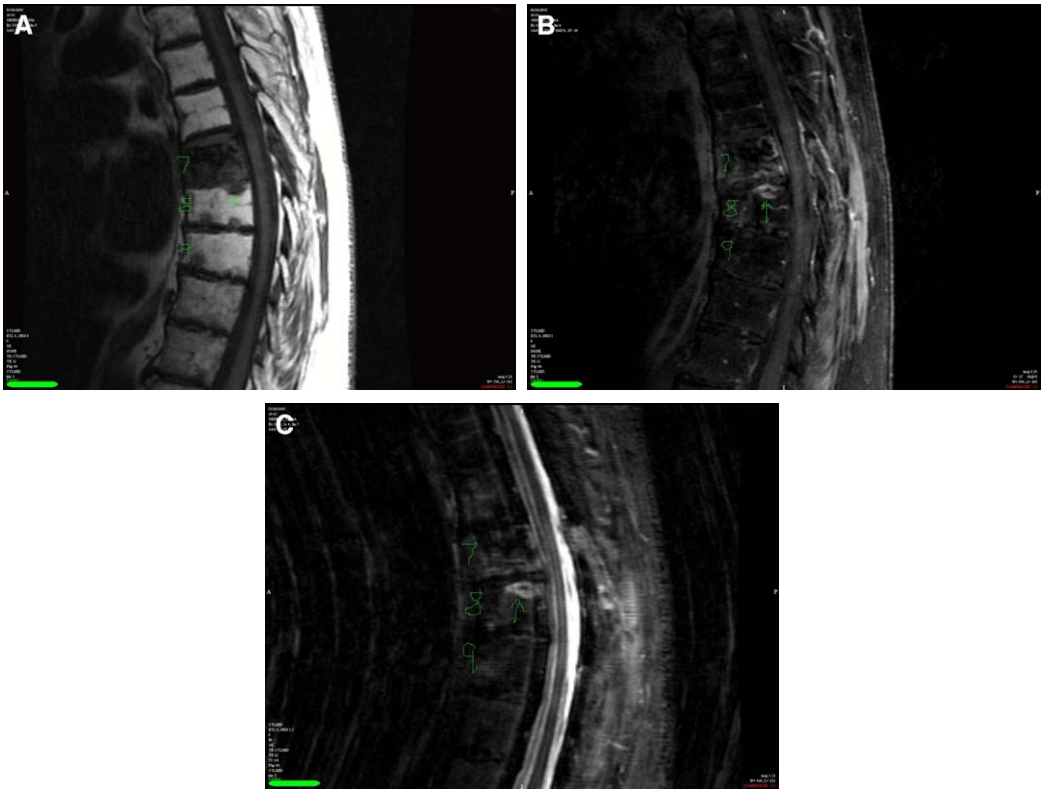

Fig. 40. Comparison of short time inversion recovery (STIR) fat-suppressed images and chemical fat suppression in metastatic disease of the thoracic spine. Sagittal phased-array MRI in a patient with cancer. (*A*) T1-weighted (T1W) spin echo (SE) image without fat suppression demonstrates normal brightness to the subcutaneous and paravertebral fat. The spinal cord is unremarkable. There is diffuse replacement of the normal fatty marrow with low signal intensity in the T7 vertebral body. (*B*) Sagittal T1W, gadolinium-enhanced, fat-suppressed SE image demonstrates pathologic enhancement of a lesion which is T8 (*arrows*) not as well demonstrated on the other pulse sequences. In addition, there is heterogeneous vertebral body involvement of T7. (*C*) Sagittal STIR image of the thoracic spine illustrates the additive effects of contrast with this sequence. Fat is suppressed in the vertebral bodies and the adjacent paravertebral fat. The increased water content of the metastatic lesion in T8 is more conspicuous than on the unenhanced T1W image.

suppression of unwanted tissue signal based on selective chemical saturation [60,61]. If one were to take an NMR spectra of a given voxel of tissue, it is readily apparent that the proton resonances vary slightly depending on the chemical constituencies. A hypothetical and simplified spectrum of several substances is given in Fig. 46. Suppose that a standard SE pulse sequence is used. By applying a narrow frequency pulse and exciting only one of the chemical constituents, such as fat, before the SE sequence is begun, the signal from the fat can be eliminated by saturating it. An example of this is given in Fig. 47. A narrow frequency pulse is applied to the tissue of interest, exciting only fat molecules. Now, when the SE sequence is applied, the proton vectors of the fat molecules are already in the *x*-*y* plane. When the 90° pulse is applied for the SE sequence, they are inverted along the negative *z*-direction and generate no signal during the FID or after the 180° refocusing pulse. A similar strategy may be used to suppress silicone (eg, in the evaluation of silicone breast implant rupture) and to suppress water associated with complex proteins (eg, magnetization transfer).

Fat suppression with chemically selective pulses, although generally a useful technique, must be interpreted with caution at times. The saturation only works in a highly uniform field. This means that tissue situated well away from the isocenter of the magnet, asymmetric anatomy, and areas in which there is distortion of the

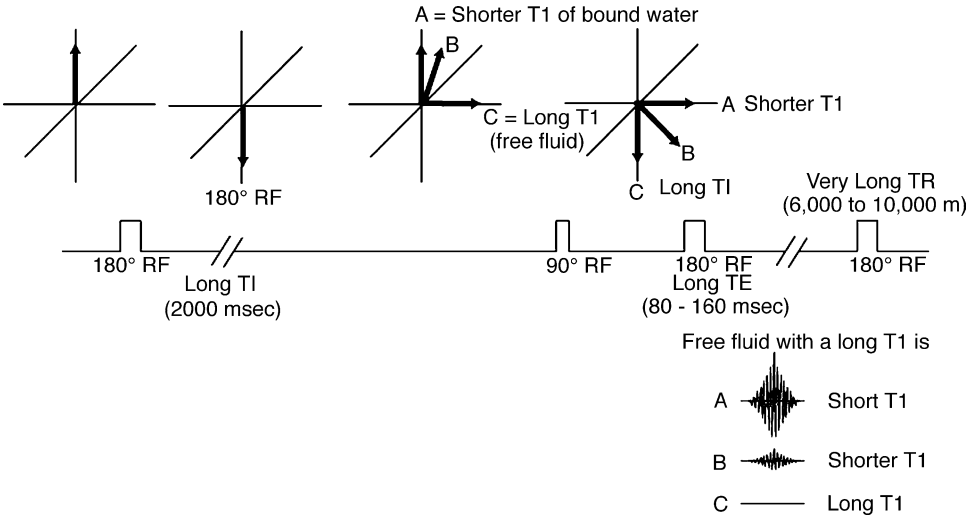

Fig. 41. Fluid-attenuated inversion recovery (FLAIR) sequence. A 180° radiofrequency (RF) inversion pulse is given. A long time to inversion (TI) is allowed before the 90° RF pulse is performed. By this time, substances with a shorter T1, such as bound water, have returned to the *z*-axis. Free fluid represented by tissue C, which has a long T1, is now at the *x*-*y* plane, however. When the second 90° pulse is given, substances, such as tissue C, with a long T1 are inverted into a negative *z*-direction. At the echo, no signal is obtained. Tissues with a relatively shorter T1, such as those with bound water, give maximum signal in the *x*-*y* plane. Note that an extremely long repetition time (TR) is needed (6000–10,000 milliseconds) to allow complete recovery of the tissues with long T1s back to baseline before the pulse sequence is begun again. A fairly long echo time (TE) is then used for data sampling. This sequence therefore highlights substances that have a relatively short T1 and a long T2.

magnetic field from metal artifact, for example, yield poor fat saturation and, at times, confusing signal intensities. Fig. 48 gives an example of how fat suppression can be used to evaluate a brain lesion.

Pulse preparation

The second form of pulse sequence modification seen extensively in MRI is that of a pulse preparation. In this case, various things are done to the proton vectors that affect their later tissue contrast. For example, in diffusion-weighted imaging, strong gradients are applied after tissue excitation to emphasize differences in microscopic motion of protons. Spoiler gradients are commonly applied in conjunction with fast gradient echo imaging techniques to reduce residual and unwanted transverse magnetization between each pulse sequence. Finally, the intrinsic tissue contrast can be altered by applying special preparatory RF pulses before initiation of the main pulse sequence. Examples include magnetization-prepared rapid gradient echo and magnetization-prepared IR sequences.

Gradient echo imaging

Gradient-recalled acquisition schemes (eg, GRASS, fast low-angle shot, fast imaging with steady-state precision) are similar to the SE pulse sequence except that the 180° refocusing RF pulse is not used. Additional gradients may also be added. One of the reasons why the proton spins undergo rapid T2 phase decay is the application of encoding gradients during data acquisition. To obtain phase coherence, these gradients must be reversed in the second half of the pulse sequence so that all the protons are brought back into phase during data acquisition. This reversal of the encoding gradients forms its own natural echo from what little transverse magnetization is remaining. Areas that are dephased by the slice-encoding and frequency-encoding gradients are brought back into phase by reversing the gradient polarity, which makes the faster spinning vectors slower, as shown in Fig. 49. The precessional direction of the vectors does not change as it does with SE, however. Note that in this case, we are working with T2* relaxation, which occurs much more quickly than T2 relaxation. Therefore, TEs used must be much shorter if any signal is to be

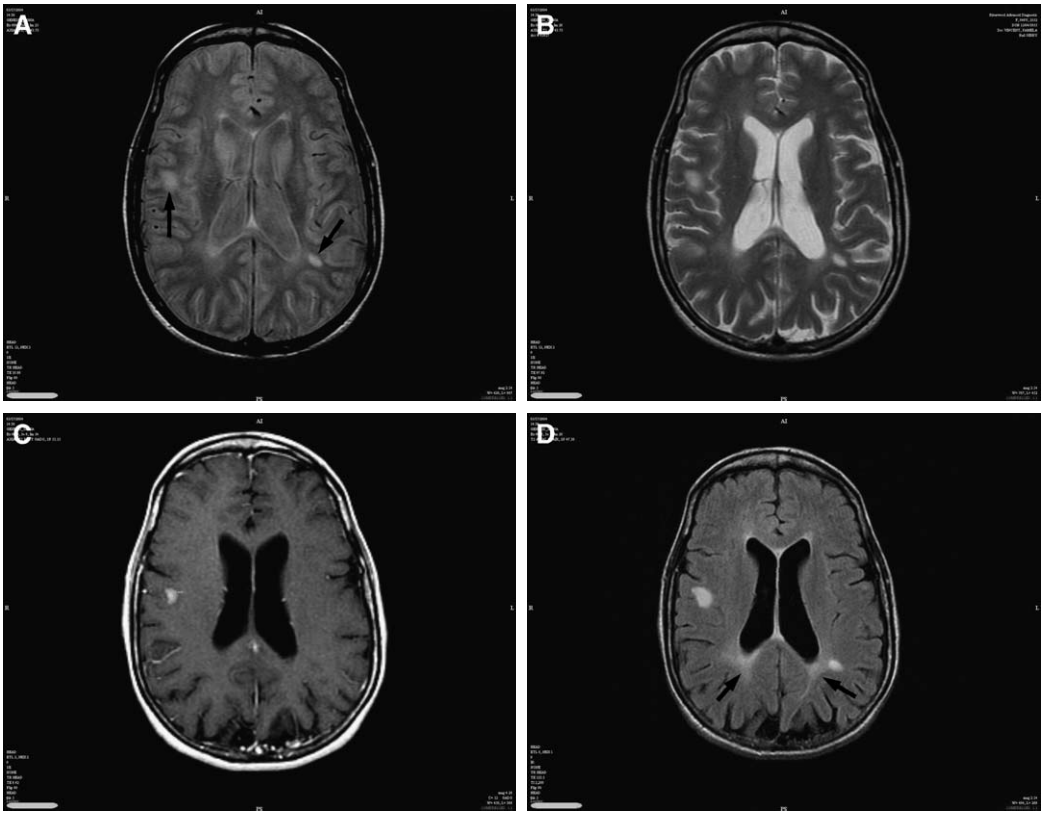

Fig. 42. Imaging in a multiple sclerosis patient demonstrates the utility of fluid-attenuated inversion recovery (FLAIR). (*A*) Proton-weighted T2-weighted (T2W) fast spin echo (FSE) image at the level of the lateral ventricles demonstrates several periventricular white matter lesions (*arrows*). These are fairly well seen, although smaller lesions can be missed (repetition time [TR] = 3150 milliseconds, echo time [TE] = 10.9 milliseconds). (*B*) T2W FSE (TR = 3150 milliseconds, TE = 98 milliseconds). The periventricular demyelination is less observable because of adjacent cerebrospinal fluid in the sulci. (*C*) Axial T1-weighted gadolinium-enhanced (TR = 416 milliseconds, TE = 8.4 milliseconds) spin echo sequence demonstrates an enhancing plaque lesion in the posterior right frontal lobe. Although this sequence is excellent for showing areas of blood-brain barrier breakdown, many of the plaques are not active and hence not visible. (*D*) Axial fast FLAIR images (TR = 8800 milliseconds, TE = 123 milliseconds, time to inversion [TI] = 2200 milliseconds) reveal the plaques previously identified with the proton-weighted sequence with a much greater degree of conspicuity. In addition, the periventricular white matter disease in the periatrial areas is much more evident (*arrows*). Also notice the area of vasogenic edema in the posterior right frontal-temporal cortex. The vasogenic edema is larger than the area of blood-brain barrier breakdown seen on the contrast-enhanced images.

received. Furthermore, because there is not a reversal of the direction of the spinning vectors from a 180° RF pulse, phase loss caused by static field homogeneities cannot be recovered. These images tend to be more artifact prone, particularly at tissue interfaces, where diamagnetic effects are present, and in regions where there is ferromagnetic or paramagnetic material. Fig. 50 demonstrates the differences between SE and gradient echo sequences. They are also prone to chemical shift artifacts. The major advantage to gradient-recalled acquisition imaging is that the second 180° RF pulse need not be used. This means less RF power deposition within the patient over a given time and the ability to image faster. It also means that there is less saturation (ie, loss of the longitudinal magnetization) and less cross-talk from excitation of adjacent slices. As a result, thinner and faster slices can be obtained.

Limited flip angle imaging

This technique is most often used in conjunction with gradient echo imaging [62]; however,

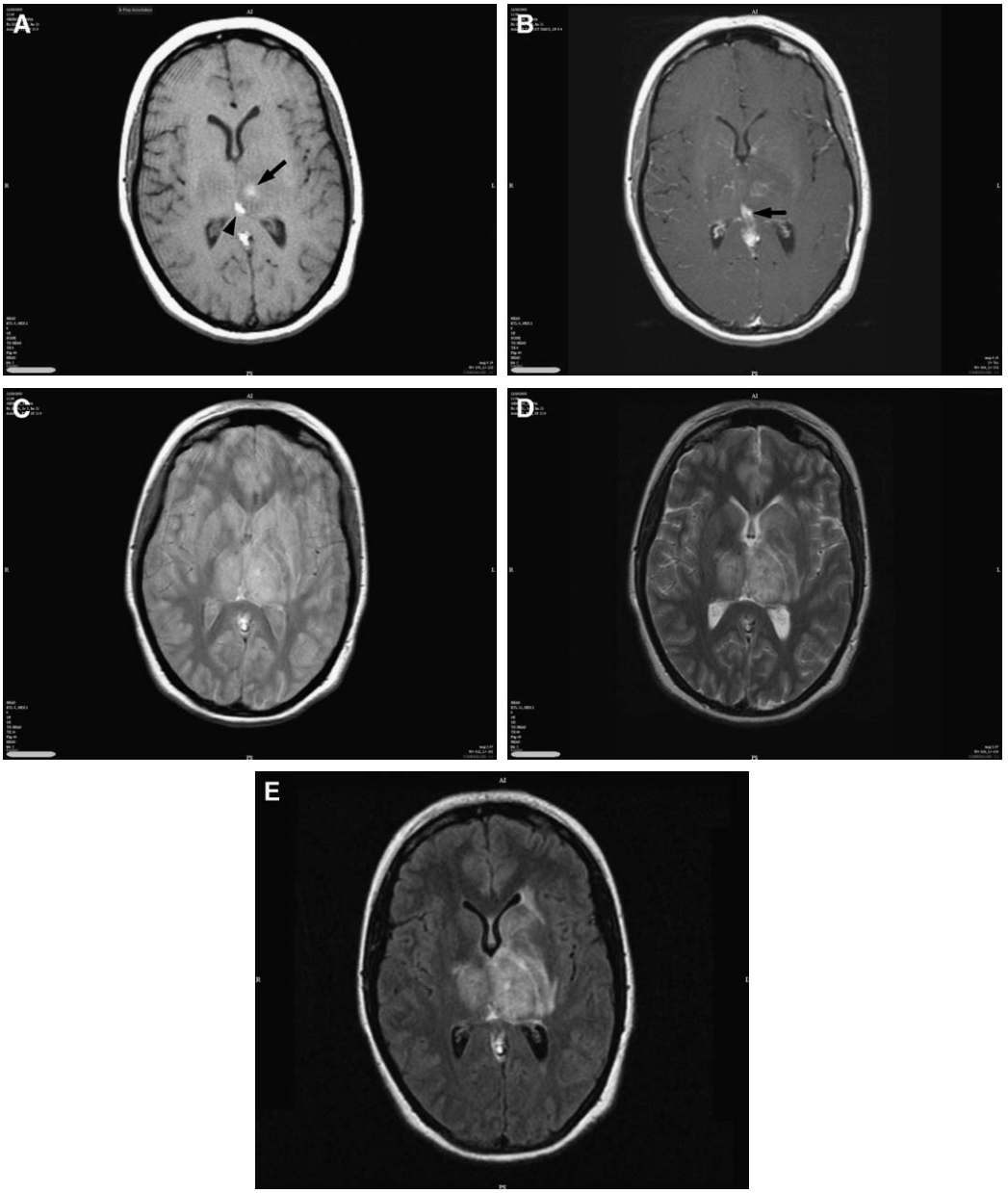

Fig. 43. A 23-year old patient with an internal cerebral vein and straight sinus thrombosis causing recent venous infarcts. The dramatic sensitivity of FLAIR sequences compared with other spin echo (SE) techniques is demonstrated. (*A*) Axial T1-weighted SE image through the level of the thalami demonstrates a small amount of high signal intensity in the left thalamus consistent with a recent hemorrhage in the Met-hemoglobin form (*arrow*). There is also high signal intensity just posterior to this in the great vein of Galen consistent with thrombosed Met-hemoglobin (*arrowhead*). (*B*) After gadolinium enhancement, there is some minimal enhancement of congested veins of the thalami and left basal ganglia as well as slow flow in the vein of Galen (*arrow*). (*C*) Proton-weighted fast SE image yields little contrast between the areas of venous infarction and surrounding brain. (*D*) Axial T2-weighted (T2W) SE image demonstrates swelling of the thalami bilaterally, more so on the left side. (*E*) Axial T2W FLAIR image dramatically highlights the extent of the vasogenic edema in the left caudate nucleus and the thalami bilaterally as well as in the internal capsule on the left.

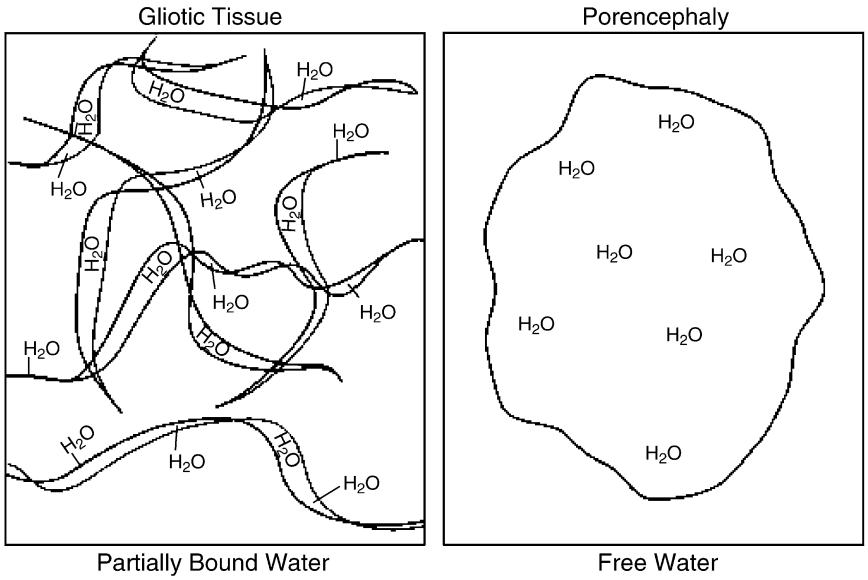

Fig. 44. Gliotic lesion versus porencephaly. Gliotic tissue is represented by a matrix of proteinaceous strands and debris to which water is loosely bound. This slows the molecular motion of the water, shortening its T1. On a fluid-attenuated inversion recovery (FLAIR) image, this water is not suppressed and remains relatively bright. Such a lesion is bright because of the decreased T1 of the water and the relatively long T2 of loosely associated water. Conversely, water in a porencephalic cyst undergoes rapid rotational movement and has poor relaxation efficiency. The water with the long T1 in the FLAIR sequence is effectively suppressed, and signal is not seen.

these are two separate imaging principles. In a limited flip angle pulse sequence, the *z*-magnetization is tipped less than 90°. Typically, values of 5° to 40° are used, depending on the contrast effects desired. In this pulse sequence, there are three pulse parameters, which are operator dependent and can affect tissue contrast: flip angle, TR, and TE. Of course, these are not independent. The flip angle heavily affects the degree of T1 weighting. What happens is that T1 effects are eliminated at small flip angles because you are using only a small amount of the longitudinal magnetization with each pulse. Only spin density and T2* contrast remain. In Fig. 51, an 18° RF pulse has been applied to our system. The *z*-magnetization is tipped only a short distance. Because of this, the net *x*- and *y*-vectors are smaller. These begin to dephase as expected. When the spins are brought back into alignment, an echo is generated. Because limited flip angle sequences use gradient reversal, only those phase losses caused by the earlier applied gradient in the opposite direction can be recovered. Because only a small portion of the longitudinal magnetization is used each time, the tissue is not as saturated as if a 90° or 180° RF pulse had been applied. Unless the TR is extremely short (which saturates the sample), most of the magnetization is still available regardless of whether the substance has a short or long T1. Thus, the contrast of the images does not depend on T1 and becomes dependent on T2* or hydrogen density. Because only a small amount of the longitudinal magnetization is flipped into the *x*-*y* plane, these images tend to be noisy and signal limited. The major reason for wanting to use this pulse sequence is that of speed. Heavily T2*-weighted images can be obtained even at fairly short TRs. In SE imaging, we had to wait 2500 to 4000 milliseconds before applying the next 90° RF pulse. When only a small flip angle is used, T2* weighting can be achieved with TRs as short as 25 to 75 milliseconds. Because this sequence is virtually always used with the gradient reversal acquisition technique rather than being T2W, these are T2* weighted. This means that rather than seeing true T2 decay of a tissue, we see the effects of tissue T2 and static local field inhomogeneity.

Summary of our model to this point

The basic SE pulse sequence and its variants have been introduced. The incoherent spinning nuclei are brought into coherence by a 90° RF

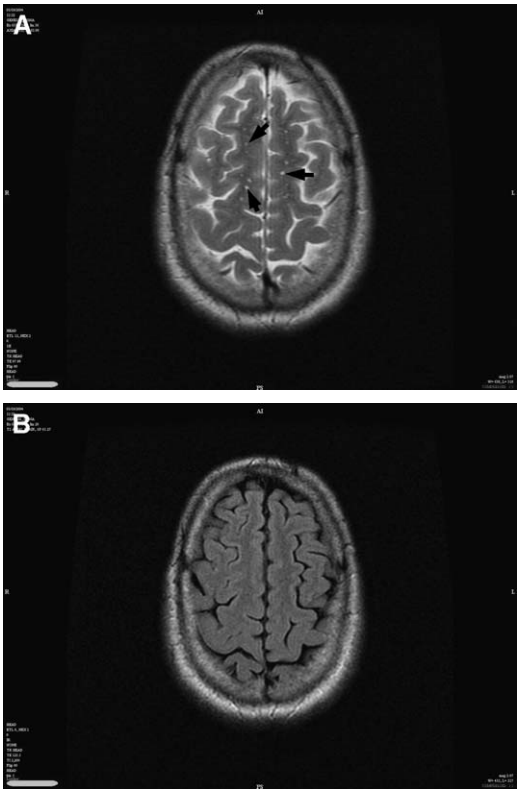

Fig. 45. Fluid-attenuated inversion recovery (FLAIR) sequence demonstrating the difference between état cribblé and white matter lesions. (*A*) Axial heavily T2-weighted (T2W) fast spin echo image over the vertex of the brain demonstrates multiple areas of increased signal abnormality in the subcortical white matter (*arrows*). (*B*) FLAIR image through this same location shows no evidence of signal abnormality. The increased signal in the T2W image is caused by free water in dilated perivascular spaces, which are suppressed by the FLAIR sequence. Therefore, these are not true white matter lesions.

pulse. Time is allowed to elapse, and a second 180° pulse is administered, inverting the spinning vectors and bringing them into phase coherence again. This creates a second signal, or "echo." The echo occurs at time to TE (time to echo). The shorter the TE, the less decay of signal there is; hence, the best signal-to-noise ratio is obtained with short echo sequences. For this reason, most T1W and proton-weighted sequences give the highest anatomic detail. Most pathologic processes exhibit prolonged T2 values, however. By using long TEs, the discrimination of normal versus abnormal tissue is enhanced. The IR family of pulse sequences has been introduced, each with unique capabilities. Traditional IR yields beautiful T1W sequences. STIR images can be used to suppress short T1 substances, such as fat. FLAIR is a unique T2W sequence that suppresses free water, such as CSF, but highlights bound water, such as myelin plaques.

Forming an image: spatial encoding

With a basic understanding of nuclear magnetic relaxation and pulse sequences, we are now ready to tackle some of the most difficult concepts involved in MRI. The concept of spatially encoding the MRI signals was first devised by Lauterbur [63] in 1973. A myriad of different techniques have been devised to localize and acquire the NMR signals spatially point by point [63–65], line by line [66–68], plane by plane [69,70], or even three dimensionally [71,72]. The technique described in this article is essentially that of spin warp imaging, first described by Kumar et al [70] and modified by Edelstein et al [73]. Many investigational groups, such as those headed by Mansfield [69], Lauterbur [63], Crooks [68], Hinshaw [74], and Pykett [66], made substantial contributions to the development of the techniques required for rapid signal acquisition.

Spin echo, single-slice, two-dimensional data acquisition

This technique encompasses most currently used data acquisition schemes for MRI (if one includes the modification of fast SE). At the end of this section, I briefly discuss other techniques, such as gradient echo imaging and three-dimensional (3D) data acquisition.

When the body is placed in a strong homogeneous magnetic field, the protons align for and against the magnetic field. A net vector of magnetism exists, directed along the *z*-axis. Each of the individual nuclei is out of phase, and the net vectors of each voxel are pointed only toward the *z*-direction, as is illustrated in Fig. 52. The task now at hand is to excite and record information from only one voxel. A voxel is a small volume of tissue equal to the pixel size times slice thickness. A pixel is the size of a single point in a slice. In the technique described by Damadian et al [65], the magnetic field was shaped with gradients such that only one point in the center was homogeneous and was thus sensitive to the spinning nuclei of the given frequency. The sensitive point or field-focusing NMR method required the physical movement of the object within the gantry. The

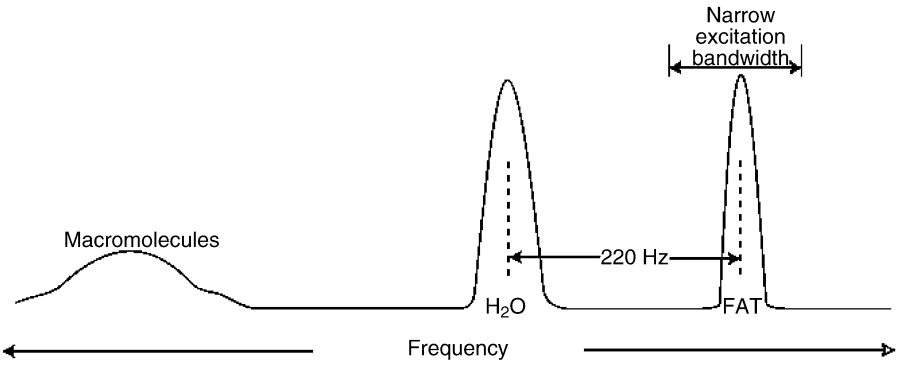

Fig. 46. The protons of fat, water, and macromolecules precess at slightly different frequencies. At 1.5 T, the separation between fat and water is 220 Hz.

data were acquired point by point, with the rather crude image requiring longer than 20 minutes, because each voxel must be recorded independently. The success of current imaging schemes relies on simultaneous acquisition of many of these points; otherwise, imaging times would be far too long for practical use.

Selective excitation

The heart of NMR imaging is the fact that the hydrogen nuclei precess at different frequencies, depending only on the local magnetic field strength. By applying a magnetic field gradient across the static magnetic field, the nuclei at one location can be made to precess at a different frequency than those in another location. This is diagrammatically shown in Fig. 53. The hydrogen nuclei are represented by circles, with the larger circles being those spinning at higher frequencies. We also know that for nuclear excitation to occur (ie, to tip the spins from alignment with the magnetic field to alignment against the magnetic field), an energy input that is exactly equal to that of the Larmour frequency is required. The Larmour frequency is the frequency at which

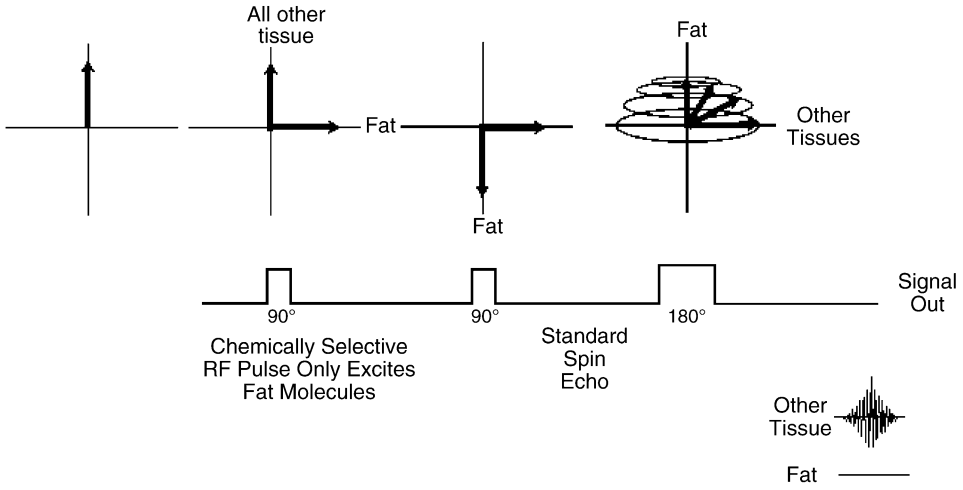

Fig. 47. A chemically selective 90° radiofrequency (RF) pulse (for fat in this case) is applied just before the standard spin echo sequence. This has the effect of rotating the proton vectors for the fat molecules into the *x*-*y* plane. When the next 90° pulse is given, the fat is inverted into the negative *z*-axis and all other tissue precesses within the *x*-*y* plane. A standard 180° refocusing RF pulse is given, which has the effect of returning fat back into the positive *z*-direction. As such, it has no net vector in the *x*-*y* plane and does not yield signal.

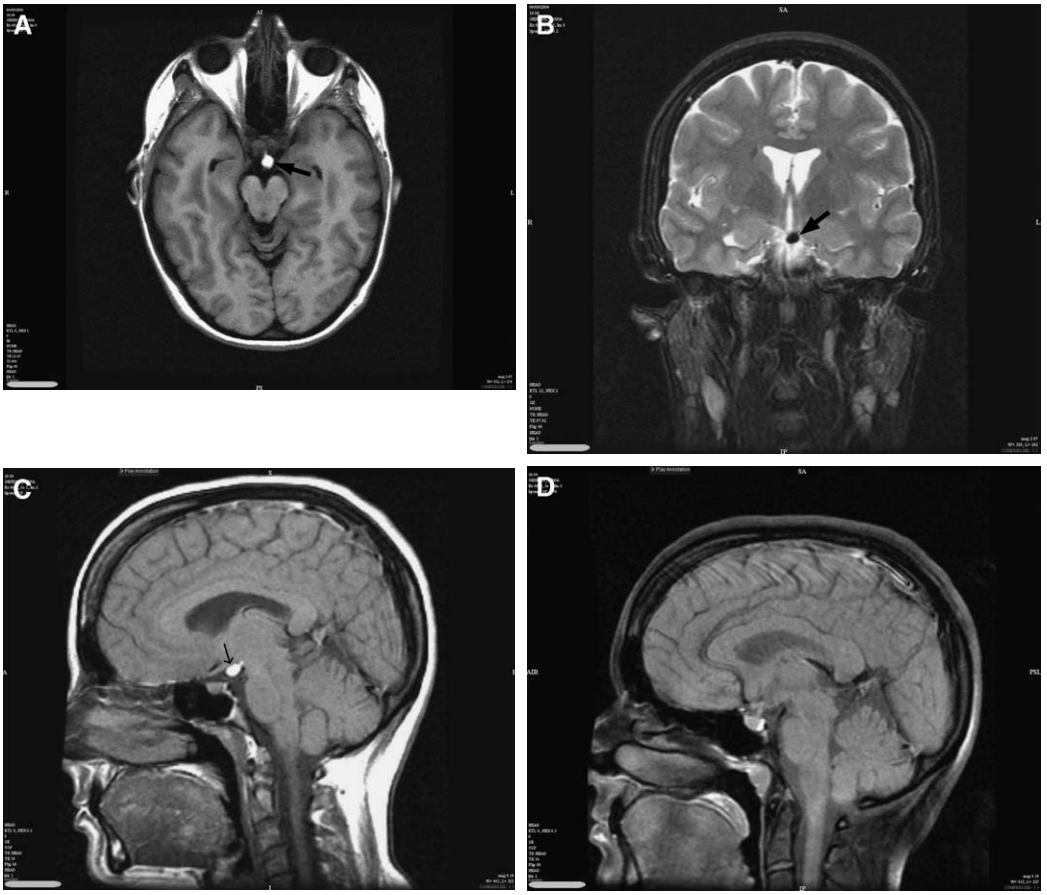

Fig. 48. Small lipoma of the interpeduncular cistern just ventral to the basilar artery. (*A*) Axial T1-weighted (T1W) inversion recovery image reveals a small, round, high signal intensity lesion ventral to the midbrain and behind the pituitary gland in the interpeduncular cistern (*arrow*). (*B*) Coronal spin echo (SE) image demonstrates that the lesion darkens considerably on a heavily T2-weighted image (*arrow*). (*C*) Sagittal T1W SE image also reveals the high signal intensity lesion just above and behind the pituitary fossa in the interpeduncular cistern (*arrow*). (*D*) The key diagnostic images are the sagittal fat-suppressed T1W images, which reveal that the lesion is completely suppressed after the application of a chemically selective saturation pulse. This confirms the diagnosis of benign fat as opposed to tumor, hemorrhage, or other lesion.

the protons precess at a given field strength ($\nu = \gamma \cdot G/2\pi$).

Suppose that our system has a static magnetic field of 1.4565 T, which corresponds to protons spinning at 62 mHz. If a small magnetic gradient is applied (0.0235 mT) on the *z*-axis, those on the left side spin at 62 mHz, whereas those on the right side spin at 62.001 mHz. This difference is 0.001 Hz. Shown diagrammatically in Fig. 54 is a volume of tissue with the gradient applied and the various nuclei spinning at different frequencies depending on their location. If the sample is now irradiated with a 90° RF signal that has a broad bandwidth (ie, 62 mHz ± 1000 Hz), all the protons are excited. If a narrow bandwidth is given, however, corresponding, for example, to 62.0050 mHz ± 10 Hz, a narrow slice of nuclei can be excited. All of the other nuclei on either side of the slab of interest are not excited and thus do not contribute to signal later on in the imaging process. This means that we have reduced a 3D object to a 2D object in terms of spatial localization.

Selective excitation is a first and important step in the process of image formation. Notice that the RF is delivered while the *z*-gradient is turned on for the 90° or 180° pulse. This means that the *z*-gradient must be turned on, time must allowed for

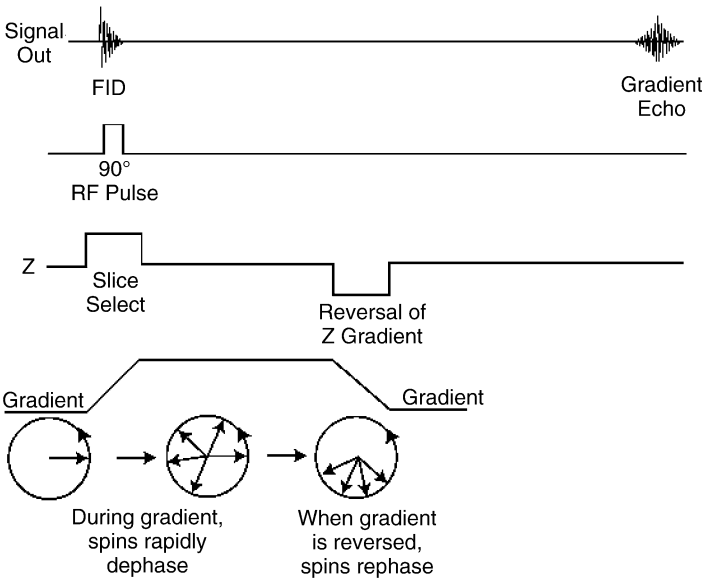

Fig. 49. Gradient echo sequence. A 90° radiofrequency (RF) pulse is given. When the slice selection gradient is turned on, there is rapid dephasing of the spins because of the gradient. Those in the region of higher gradient strength spin more quickly than those in the region of lower gradient strength. When the *z*-slice select gradient is reversed, the spins are rephased. The vectors that were previously spinning in the higher gradient strength are now spinning in the lower gradient strength. This is a simplified diagram showing only the *z*-slice select gradient. A similar reversal of the *x*-gradient must occur simultaneously. Note that a spin echo would not occur in a traditional spin echo sequence unless a gradient echo was also present. FID, free induction decay.

it to stabilize, and the 90° or 180° pulse must then be applied. The *z*-gradient is then switched off.

Prescanning

In SE imaging, a 90° pulse is initially delivered, that is, the average vector of each voxel is rotated into the *x*-*y* plane. How is this accomplished? Depending on the size of the structure the RF permeability is, and the tissue type, there are different amounts of RF absorption. This varies with the slice thickness, patient size, and coil loading, for example. This also changes as a function of field strength. The body is less "permeable" to RF at higher frequencies, resulting in nonuniform RF tip angles as a function of depth from the skin, especially at greater than 30 MHz [75]. How can we know how much RF energy to deposit into the tissues to exactly tip the average vector of each voxel into the *x*-*y* plane to achieve maximum signal return? This is done by prescanning. The prescan is part of the setup for each pulse sequence. During this process, a RF pulse is given to the center slice (or, depending on the system, the entire area) of the region to be imaged. A FID is then measured for amplitude, and the process is repeated with greater or smaller RF energy until a maximum FID is observed. At this point, the "tip angle" is 90°.

Phase encoding

After selective excitation of a single plane, our 3D object has now been reduced to a 2D object. Phase encoding is the next step in uniquely identifying each voxel of information. Immediately after the application of the 90° RF pulse with the *z*-gradient turned off, all the spins in the selected plane are precessing at the same angular velocity and each has an identical phase. This plane of spins precessing in the *x*-*y* plane is diagrammed in Fig. 55. These spins rapidly become out of phase, and the FID signal generated is quickly lost. For the sake of simplicity, however, let us assume that the spins remain precessing in phase. If a gradient is now applied along the *x*- or *y*-direction for a brief period, the *y*-axis in this example, the following events occur.

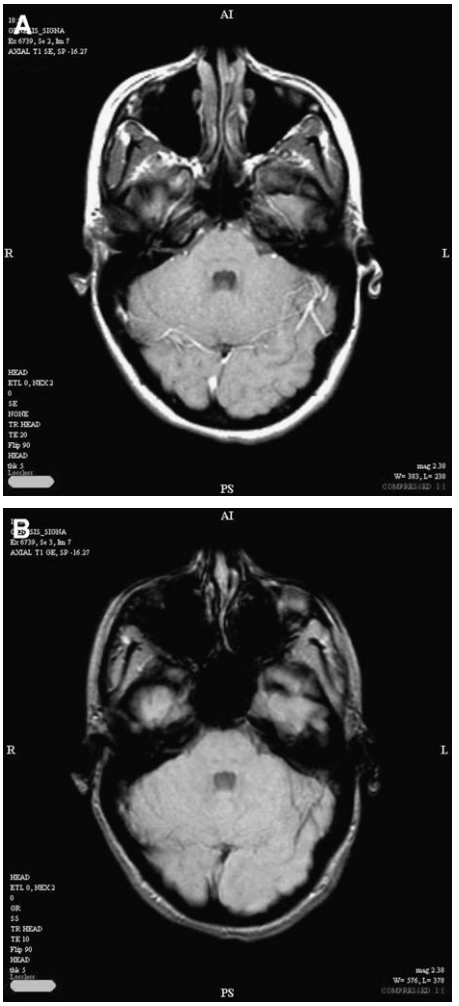

Fig. 50. (*A*) A standard T1-weighted (T1W) spin echo image was obtained through the posterior fossa and paranasal sinuses in the axial plane. (*B*) A T1W gradient echo image of the same location demonstrates somewhat comparable contrast of the cerebellar tissues. Notice the extensive diamagnetic artifact (*arrows*) in the region of the paranasal sinuses, nasal septum, and complex structures adjacent to the petrous bones. In both cases, the flip angle was 90°, the repetition time was approximately 600 milliseconds, and the echo time was 10 milliseconds.

Those spins in the higher magnetic field strength immediately begin precessing faster than those in the lower magnetic field strength, as illustrated in Fig. 56. Again, the faster spins are represented by the larger circles.

As a consequence of the difference in spin velocity, the individual alignment of spins becomes out of phase. Note that the phase change is uniform along the applied gradient. A given row of spins in the *x*-direction has an identical phase. The gradient is then shut off, and the spins return to precessing at the same frequency as they were in the same homogeneous magnetic field. The spins retain a "memory" of their relative phase position, however, as shown in Fig. 57.

Unfortunately, it is not possible to extract phase and frequency information simultaneously from a single echo. Data acquisition begins at the same time in each cycle. Suppose that a different strength of phase-encoding gradient is applied on the next cycle. When data collection occurs, the spinning protons are in a slightly different phase than in the preceding cycle. As they spin within the coil, they induce a sinusoidal oscillation of induced current within the coil. If they are in a different phase, the voltage induced is slightly different. Each time this process is repeated, the spins along a given row on the *x*-axis are given a different phase. When the echo occurs from the 180° pulse, signal is generated from all the spins lying within the excited plane. Each time, however, the process is repeated with a different strength of phase-encoding gradient. The antenna hears a slightly different signal from the protons with a different phase. Later, I show how these data can be combined with frequency encoding to describe the signal of each voxel uniquely.

Changing the phase angle in phase encoding is analogous to different rotational increments of the x-ray beam in computed tomography. The smaller the angle of increment, that is, the greater the number of phase-encoding steps over the 2π radian distance, the more accurate is the representation of the object. If the object is undersampled, the reconstruction is less accurate, giving rise to various artifacts. The price of more accurate information is increased data acquisition time. Each time a new phase-encoding gradient is applied, the entire cycle must be repeated. Thus, if our TR between cycles is 3 seconds and a single average (1 NEX) and 128 phase-encoding steps are obtained, the time of data acquisition is 6.4 minutes. If 256 steps are obtained, the time is doubled to 12.8 minutes.

Echo time

At this point, because of the inhomogeneity in the static magnetic fields, the sample rapidly dephases. Even those in the rows dephase with respect to each other. The FID signal ceases. As

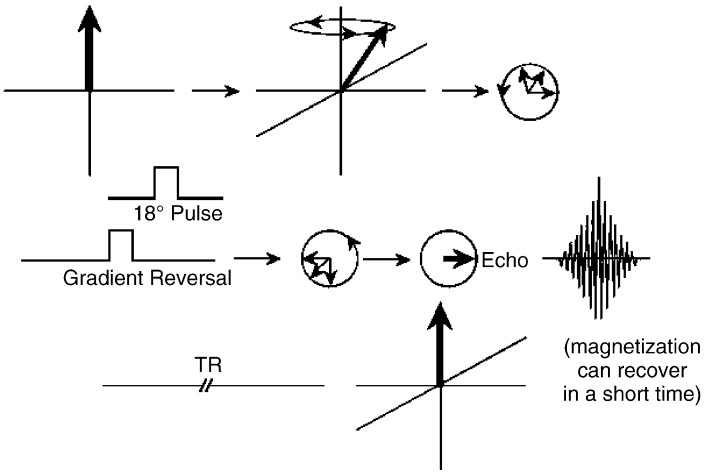

Fig. 51. Limited flip angle. An 18° radiofrequency pulse has been applied to our system. A limited flip angle sequence tips the magnetization vector only a few degrees (less than 90°). By reversing the gradients, the signal lost from gradient effects is recovered and an echo is sampled. Only a small percentage of the available magnetization is sampled for any given pulse. TR, repetition time.

explained previously, a 180° RF pulse is now applied. The time between the 90° pulse and the 180° RF pulse is TE/2, that is, the echo occurs equally spaced from when the 180° pulse occurs. This is one of the important operator-dependent parameters available with SE techniques. The longer we wait before applying the 180° RF pulse, the more "T2W" the sample is. Only those protons with sufficiently long T2 values have signal remaining when the echo is generated. At TE, the vectors in each of the *y*-columns come back into phase; however, they remember the earlier phase change brought about by the phase-encoding gradient as illustrated in Fig. 58.

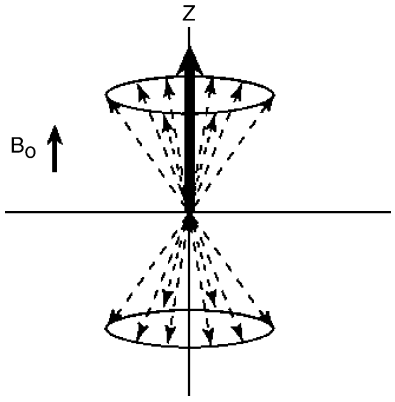

Fig. 52. Precessing vectors for and against the magnetic field, with a net magnetic vector directed toward *z*.

Frequency encoding

The final step in uniquely describing each of the voxels involves the introduction of another gradient that is present while the data are sampled. In this case, it is applied along the *x*-axis. Because the gradient is on during data acquisition, each of the different rows along the *x*-direction is spinning at a different frequency, as illustrated in Fig. 59. If a gradient is applied during data acquisition, do the spins rotate at different frequencies and thus become out of phase again? This is correct. For this reason, a negative lobe is given initially to the frequency gradient to "unwind" the spins, after which the positive gradient is applied, such that at the exact time of the

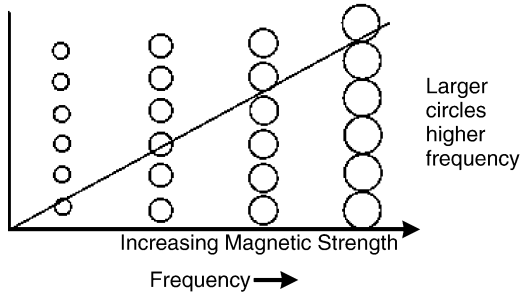

Fig. 53. Magnetic field gradient represented by a sloped line. Increasing precessional frequencies of the protons are indicated by larger circles.

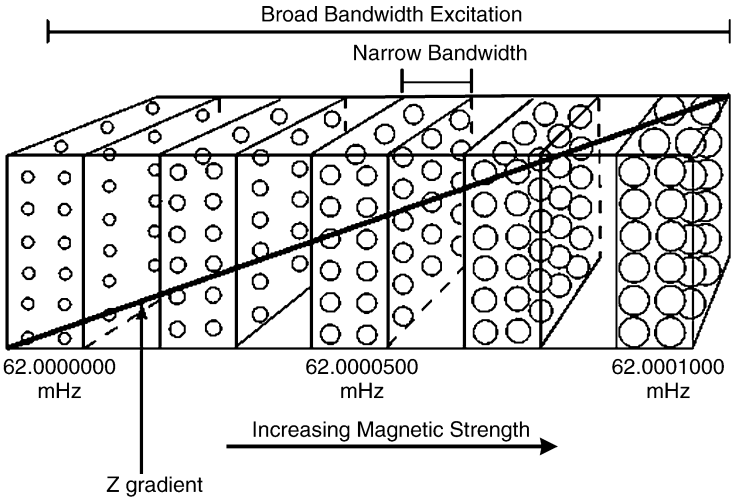

Fig. 54. A gradient across a volume of tissue along the *z*-axis. With a narrow bandwidth excitation, only the center slab of hydrogen nuclei interacts with the incoming radiofrequency pulse and is thus excited.

maximum echo, all the protons in each voxel are in phase and a coherent signal can be produced. Fig. 59 illustrates that each voxel can be uniquely described in terms of its phase and frequency during data acquisition. In Fig. 60, the entire SE pulse sequence with the appropriate gradients is diagrammatically expressed.

Image reconstruction

The signal detected, amplified, and received by the NMR machine is a group of periodic sine waves of different phases and frequencies. The fact that the signal is already present as sine waves makes the data set ideal for reconstruction by the Fourier transform method. The basis of the Fourier transform is that an object can be represented by an infinite number of sine and cosine waves. The Fourier transform is a mathematic filter that allows conversion of time domain (frequency) to spatial (x, y) coordinates.

Multislice acquisition

To this point, we have discussed the techniques for selective excitation, phase, and frequency encoding for a single slice. The imaging time for a single slice is given by the equation: Time = TR × NEX × Phase-Encoding Steps. Thus, a T2W image with a TR of 3 seconds, 128 matrix, and 1 NEX requires approximately 6 minutes. Were it not possible to acquire multiple images simultaneously, the total imaging time for a 15-slice brain study would be on the order of 90 minutes or longer for a single pulse sequence. An effective method of acquiring multiple slices at once was introduced by Kramer et al [76]. This technique is as follows: an initial slice is excited, the

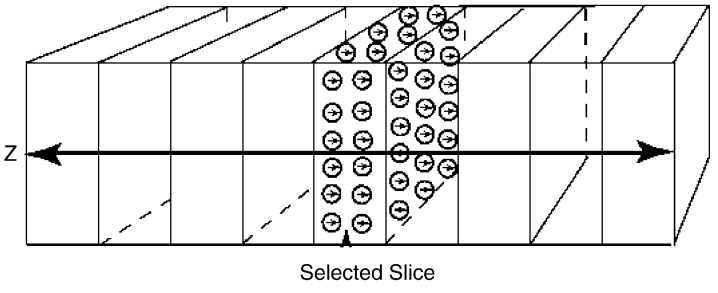

Fig. 55. A slab of selectively excited spins precessing in the *x*-*y* plane.

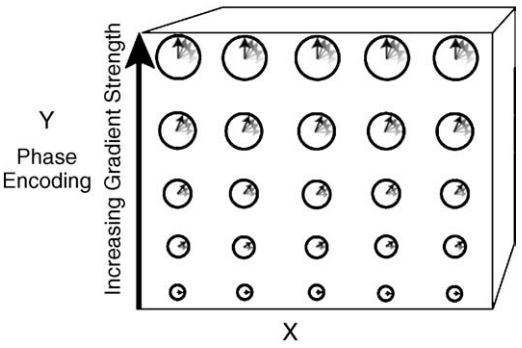

Fig. 56. Phase-encoding gradient causes spins in the stronger part of the gradient to spin faster. The faster spinning protons acquire different phases relative to other lines of precessing nuclei.

appropriate encoding gradients are applied, and the echo is recorded. Note, however, that an additional 2800 milliseconds remain after the echo within the TR before we can re-excite the slice for a different phase-encoding step in the T2W sequence with a TR of 3000 milliseconds as shown in Fig. 61. During this time, the adjacent slice can be excited, encoded, and recorded for a given phase increment, as shown in Fig. 60. After this, there are 2600 milliseconds left during the TR; the process is repeated for the next slice and so on until we have run out of time in our repetition interval and must again return to our initial slice. The first slice is then re-excited, a different strength of phase-encoding gradient is applied, the frequency encoding is performed, and data are

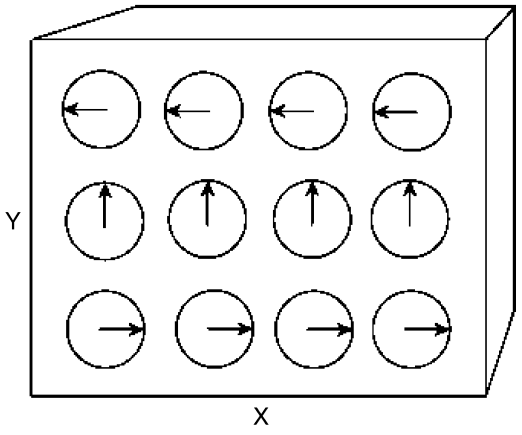

Fig. 57. At the end of the phase-encoding gradient, the phases of the spinning vectors are now uniquely encoded along the *y*-axis.

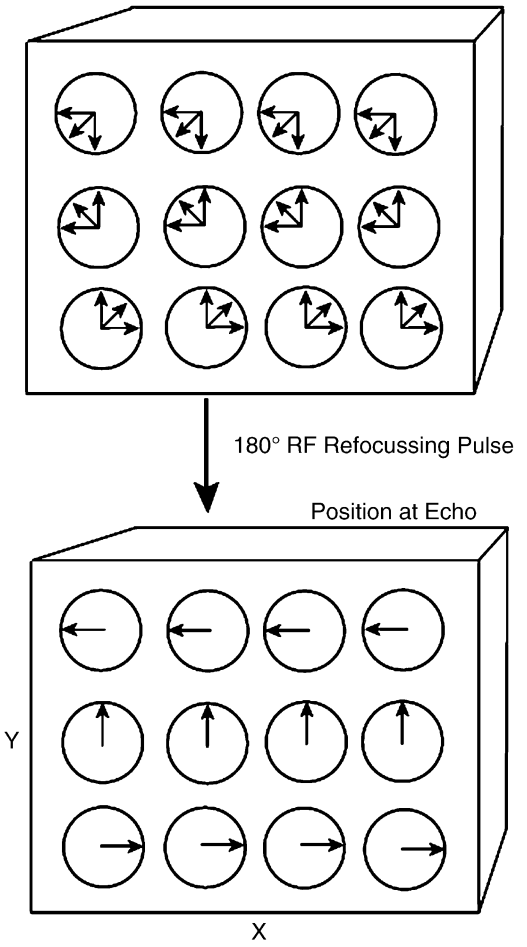

Fig. 58. Rows of spinning protons that begin to dephase are then inverted and resampled by a 180° radio-frequency (RF) pulse. Nevertheless, they "remember" the phase change brought about by the phase-encoding gradient, resulting in a predictable and measurable difference in phase between each of the lines.

sampled again. By the time that we have acquired all the necessary phase-encoding gradients for one slice, information from all the slices has been obtained. From the diagram in Fig. 62, it is easy to understand why the number of slices is limited by the TR. If the TR is increased to 4000 milliseconds, more slices can be sampled during the same acquisition. It is also limited by the TE, which is, in part, limited by the turnaround time of the machine. This duty cycle is the necessary time to excite, encode, and record images selectively from a single slice. For this reason, T1W images that have a short TR are still able to have a relatively similar number of slices compared

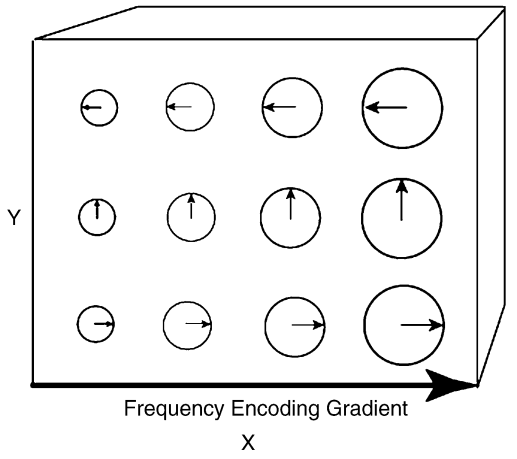

Fig. 59. A frequency-encoding gradient is now applied. The precessing nuclei in the stronger part of the gradient spin at a higher frequency. Each point or voxel within the slice is now defined by a unique phase and frequency.

with T2W sequences (T2W images have a longer TR, but the turnaround time of the machine is also greater as the TE is lengthened).

Single-slice mode

With gradient echo imaging, extremely short TRs and low flip angles may be used. When the TR is so short (on the order of 20–50 milliseconds), only one or two slices can be obtained in a multislice acquisition mode. Therefore, the multislice mode is not time-efficient. Rather, these slices are acquired individually. As shown in Fig. 63, all the phase-encoding steps are acquired for each slice before continuing on to the next slice. The total imaging time for this data acquisition scheme is: Time = TR × NEX × Matrix × Number of Slices.

Gradient echo

The unique feature separating gradient echo pulse schemes from SE is that the 180° RF pulse is omitted. In reality, a gradient echo is performed with each SE pulse sequence; however, data acquisition times and contrast phenomenology are somewhat different. Fig. 64 outlines the timing sequence for gradients and RF pulses for a typical gradient echo data acquisition scheme.

Tissue contrast that can be similar to that in SE imaging is achieved. T1 decay is unchanged. Often, gradient echo acquisition schemes are used in conjunction with low flip angles, which reduces T1 weighting; therefore, the sequence is either proton or T2* weighted. The transverse magnetization rapidly decays with the time constant of T2* as opposed to T2 in SE imaging.

The lack of a 180° refocusing pulse causes several key differences in the appearance of

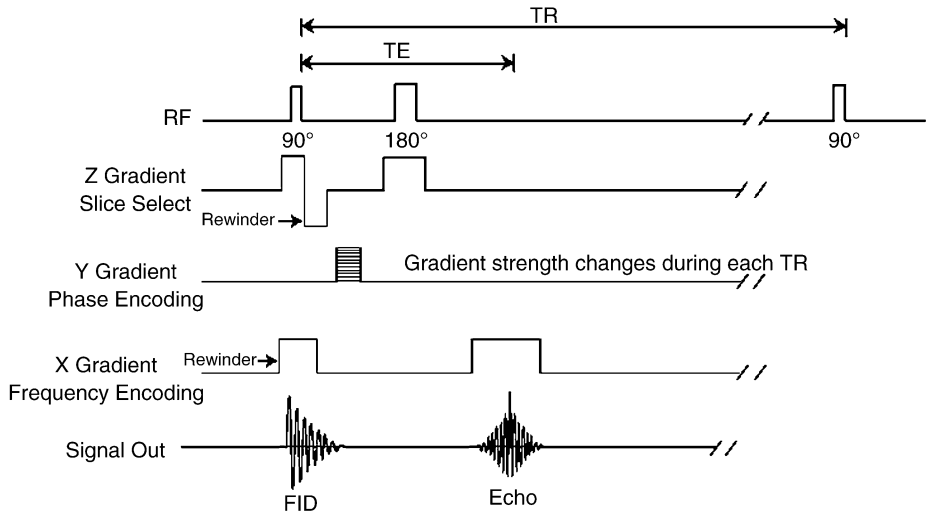

Fig. 60. This spin echo pulse sequence diagram is a bit more complex than the one diagrammed earlier in this article. In this case, the slice-encoding gradients have been added, demonstrating *z*-slice selection with the 90° and 180° pulses. An increasing phase-encoding gradient with each repetition time (TR) and a frequency-encoding gradient that is turned on during the sampling of data at the echo are also present. Rewinder lobes on the slice select and frequency gradients are also present. FID, free induction decay; RF, radiofrequency; TE, echo time.

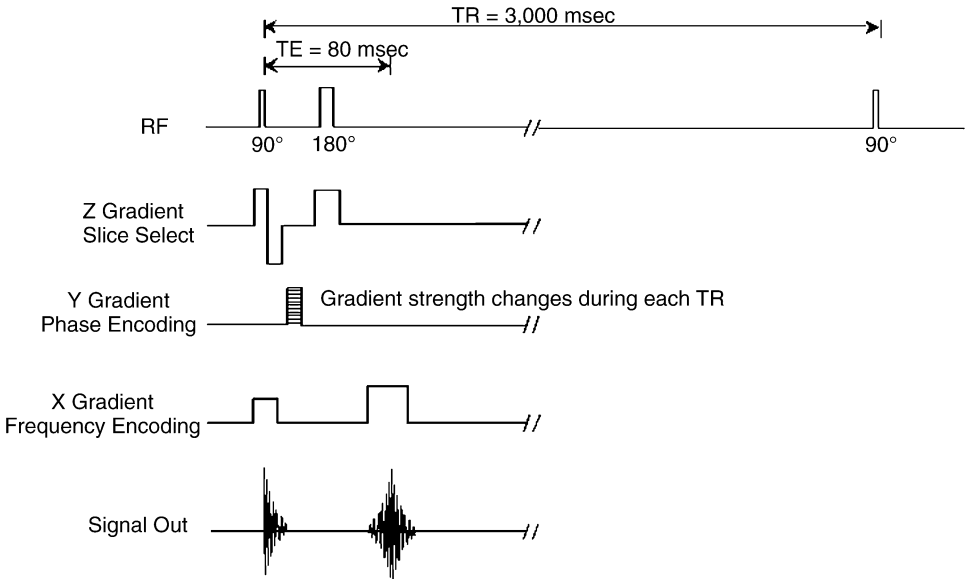

Fig. 61. T2-weighted spin echo pulse diagram with an echo time (TE) of 80 milliseconds. There is a large amount of time still remaining in the repetition cycle (3000 − 80 = 2920 milliseconds) before the next 90° pulse can be applied to that slice of tissue. RF, radiofrequency; TR, repetition time.

gradient echo images as opposed to conventional SE techniques. Phase loss caused by static magnetic field inhomogeneity cannot be recuperated. If a static magnetic field aberration is present, the phase discrepancy induced in these spinning protons is not compensated for by a simple gradient reversal. This means that the images are grainier than SE images, because there is a lower signal-to-noise ratio in some areas. To compensate for this, multiple acquisitions (or NEXs) are required. This can also be used to advantage, however, because gradient echo images are extremely susceptible to local field aberrations caused by hemorrhage, calcification, and paramagnetic or ferromagnetic substances.

A second consequence is that because a 180° RF pulse is not given, there is reduced cross-talk (saturation of the protons of adjacent slices). Serial thin sections can be obtained, as shown by the excellent-quality T1W gradient echo images of the cervical spine in Fig. 65.

Finally, flow effects are different for gradient echo images. In part, this is evident, because many data acquisition schemes used with gradient echo imaging are acquired in the single-slice mode. Each slice acts as an entry slice. Therefore,

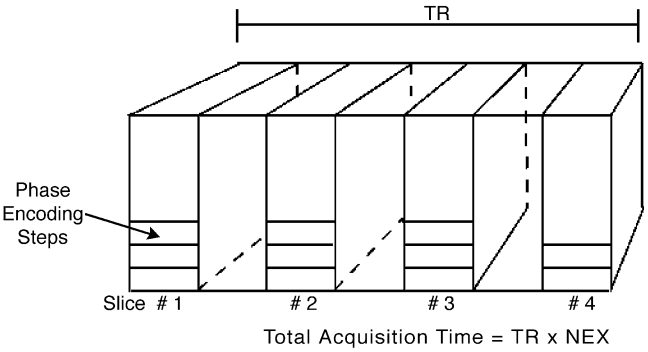

Fig. 62. Multislice acquisition. During each repetition time (TR), phase encoding of multiple slices is performed. Thus, rather than acquiring each slice sequentially, multiple slices are acquired simultaneously using dead time during the TR interval. NEX, number of excitations.

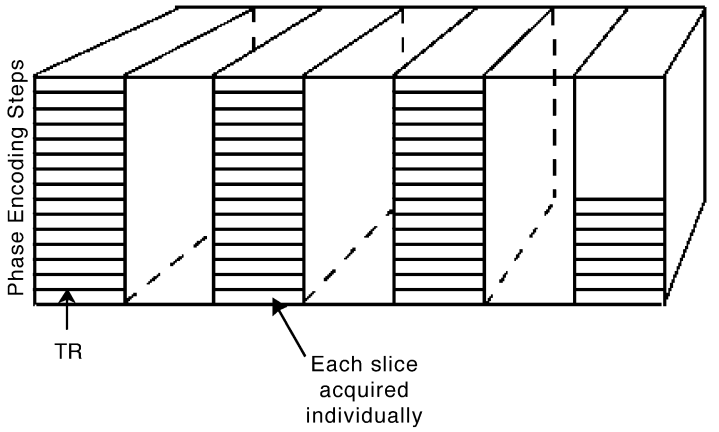

Fig. 63. Single-slice acquisition. If an extremely short repetition time (TR) is used, it is more efficient to acquire each slice individually. In this case, one line of data is acquired during each TR and an entire slice is acquired before moving to the next one. NEX, number of excitations.

flow-related enhancement is more prominent. The second reason why flow effects occur is related to the nonselective nature of gradient refocusing. A selective 90° pulse is given. If the blood flows out of the region of the slice during the time between excitation and data acquisition in SE techniques, this signal is lost. With gradient echo techniques, however, these excited protons are rephased even though they have moved out of the area of interest, and therefore contribute to signal. Gradient echo pulses are often combined with a limited flip angle to achieve extremely short TRs. Imaging time for a slice can be reduced an order of magnitude less than conventional SE.

Gradient echo data acquisition schemes are becoming more popular in clinical use for evaluation of joints, cardiac imaging, and flow studies and are a more sensitive method for detecting

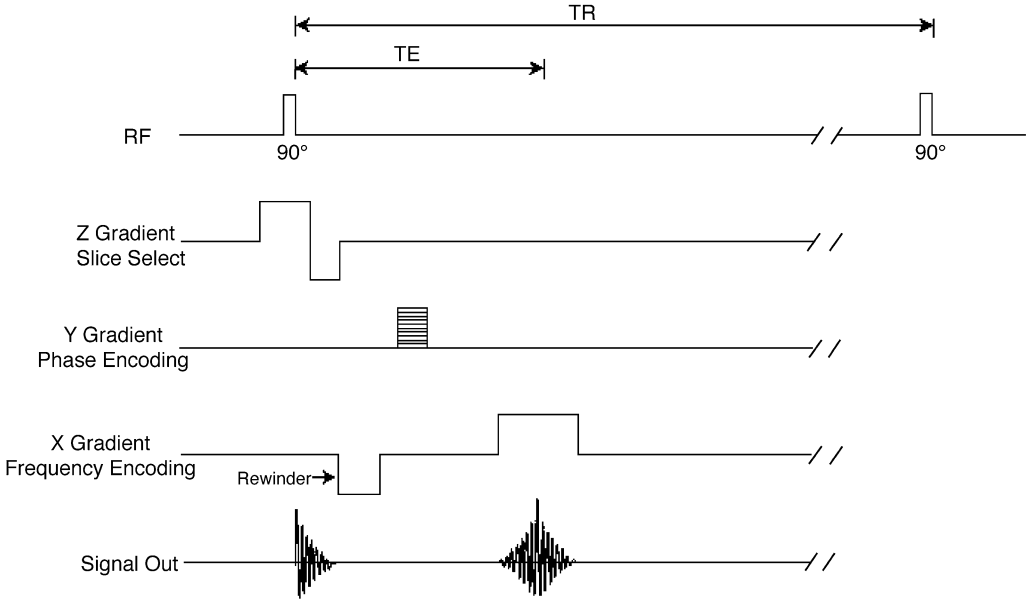

Fig. 64. Gradient echo data acquisition scheme. A simple gradient echo acquisition scheme is presented, where a 90° radiofrequency (RF) pulse is given. The reversal of the slice selection gradients in the *z*-direction and the frequency-encoding gradients in the *x*-direction give an echo as the spins are rephased. TE, echo time; TR, repetition time.

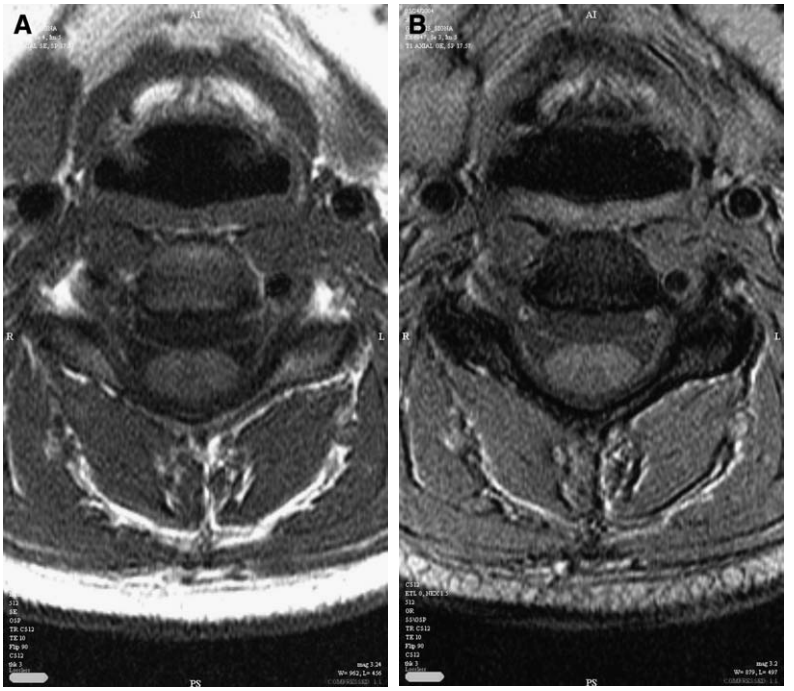

Fig. 65. Thin-section, 3-mm, T1-weighted (T1W), spin echo (SE) versus gradient echo images of cervical spine. (*A*) Thin-section, T1W, SE axial images of cervical spine are fuzzy, and it is difficult to see the nerve roots. (*B*) Same anatomy acquired with the thin-section T1W gradient echo technique. Notice improved contrast and less cross-talk between slices. For thin slices, image quality is visibly better.

hemorrhage and calcification. With extremely short TEs, excellent T1W images with contrast phenomenology similar to SE can be obtained quickly. They are my favorite for imaging the cervical spine in the axial plane.

Three-dimensional data acquisition

Until now, all the data acquisition schemes we have discussed have acquired a single slice at a time. In 3D Fourier transform volume imaging, data from the entire volume of interest is acquired during each TR. Initially, a broadband RF pulse (anywhere from 0°–90°) is applied. Instead of selecting a slice, this excites tissue in a large volume, as shown in Fig. 66. The frequency-encoding gradient can only be applied once, and that is during data acquisition. How can our 3D object be reduced to individual points? The trick is to use two phase-encoding gradients. An

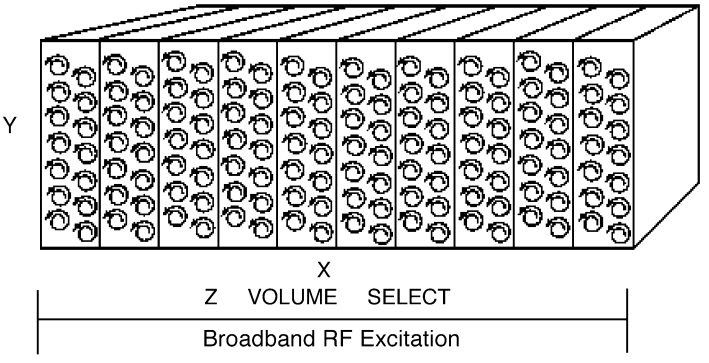

Fig. 66. Three-dimensional imaging. A broadband radiofrequency (RF) excitation excites a large volume of tissue.

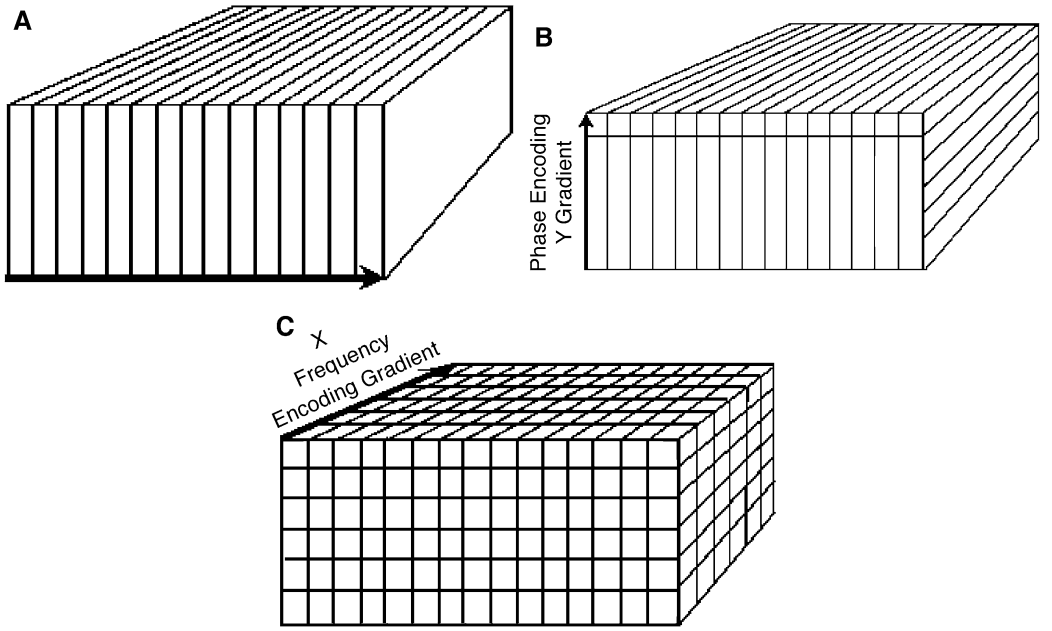

Fig. 67. Three-dimensional (3D) imaging. (*A*) Phase encoding along the *z*-axis establishes uniform phase modulation in our excited box along *z* with unique slabs. (*B*) Phase encoding along the *y*-gradient reduces our 3D object to a series of lines. (*C*) Finally, applying the frequency-encoding gradient during data sampling reduces each individual voxel to unique data.

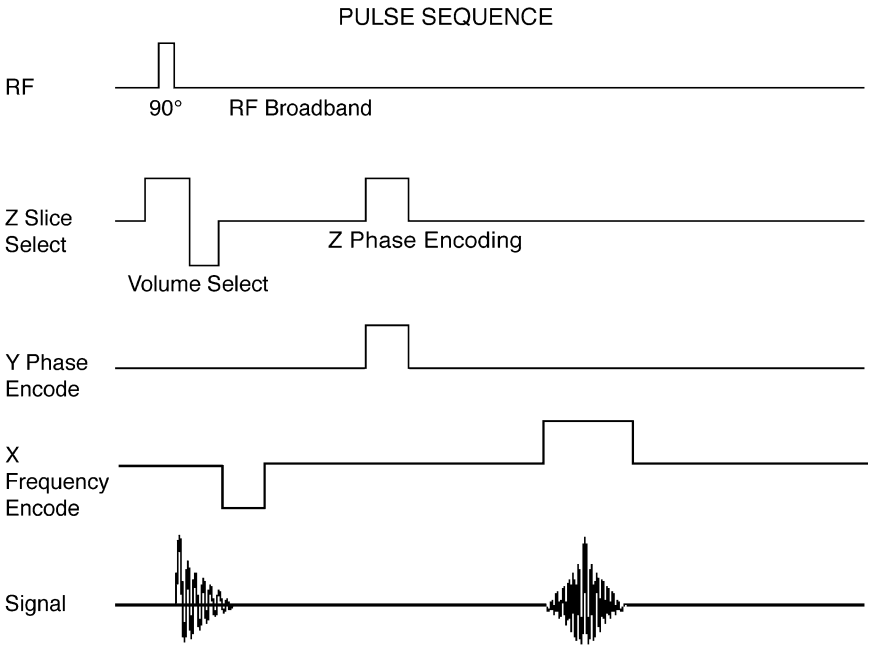

Fig. 68. Pulse sequence diagram for three-dimensional data acquisition incorporating an additional phase-encoding gradient on the *z*-axis.

additional z-phase encoding gradient is applied, which chops our box into small slices. After this, y-phase encoding and then x-frequency encoding are performed taking our 3D object from a slice to a line and to a point, respectively. This process is shown diagrammatically in Fig. 67. The pulse sequence is given in Fig. 68. A double-Fourier transform of the acquired data is performed, giving a 3D reconstruction of our object of interest. The pixel size and resolution are a function of two factors: the field of view and the number of phase-encoding steps. Suppose our box is a 10-cm cube. If we frequency and phase encode 256 steps, the voxel size in our box will be 100 mm/256 or (0.4 mm^3) = 0.064 mm^3 (Fig. 69A) resolution. If our field of view is increased to 30 cm and the number of phase-encoding and frequency-encoding steps remains the same, our voxel size increases to (1.2 mm^3) = 1.7 mm^3, a 27-fold increase in volume.

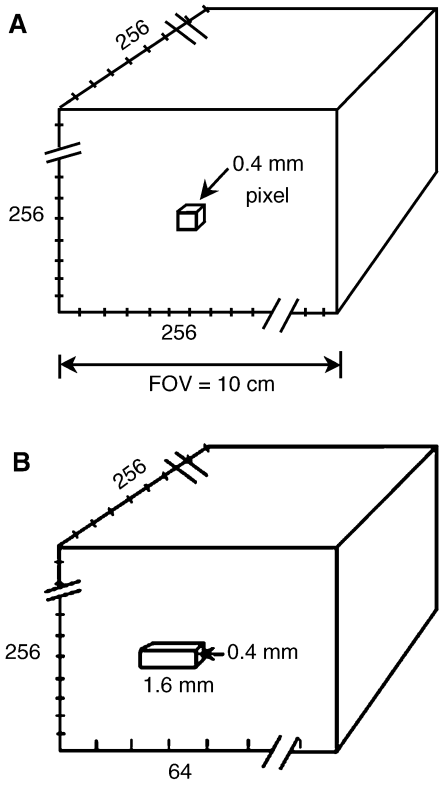

Fig. 69. (*A*) A 10-cm field of view with a 256 matrix on each side yields dimensions of 0.4 mm to each of the pixels or a 0.064 mm^3 voxel size. (*B*) Obtaining a 256 × 256 field of view by 64 yields anisotropic voxels measuring 1.6 mm × 0.4 mm × 0.4 mm, or 0.256 mm^3.

Thus, our resolution is best when a small field of view is selected.

The imaging time in 3D acquisitions is dependent on TR and number of phase-encoding steps. Because we are phase encoding in two directions, the total acquisition time is equal to TR times the number of phase-encoding steps in the z-direction times the number of phase-encoding steps in the y-direction. For a 256 × 256 × 256 matrix and a TR of 50 milliseconds, the total acquisition time is 55 minutes. Clearly, even at such a short TR, total acquisition times can be prohibitive if high-resolution work is desired. It is not even practical to think about using this technique for SE imaging in which TRs are 10 to 50 times this length. 3D image acquisition is only feasible when used with a limited flip angle and ultrashort TR techniques [76]. It is also only practical for small volumes. To achieve high resolution over a large field of view, many more phase-encoding steps must be performed.

One of the advantages of 3D imaging is that all the pixels in the matrix can be made isotropic, that is, of equal size. The data can then be reconstructed in any desired plane, not only in the three orthogonal axes but with the oblique slices reconstructed as well. This is a useful feature, because the data for a given pulse sequence need only be acquired once and any desired plane can then be reconstructed from this information. If one wishes to alter the pulse sequence to change tissue contrast or to administer a paramagnetic agent, however, the pulse sequence must be repeated.

Suppose that we want to decrease acquisition time by decreasing the number of phase-encoding steps, for example, in the z-axis. In Fig. 69B, the number of phase-encoding steps along the z-axis has been reduced to 64. Our pixel size for a 10-cm field of view is then 0.4 mm × 0.4 mm × 1.6 mm. The data are now anisotropic. Data acquisition time has been reduced by a factor of 4; however, the resulting data set cannot be reconstructed with equal resolution in any plane. Notice that the in-plane resolution along x and y still has a 256 × 256 matrix. For this plane, resolution compared with SE imaging is excellent. If the data are reconstructed in the y-z plane, however, a 256 × 64 matrix is present, which is much worse than that achievable with a routine SE sequence. Because of the use of gradient-recalled echo acquisition, these images are T2* weighted and are prone to magnetic susceptibility artifacts.

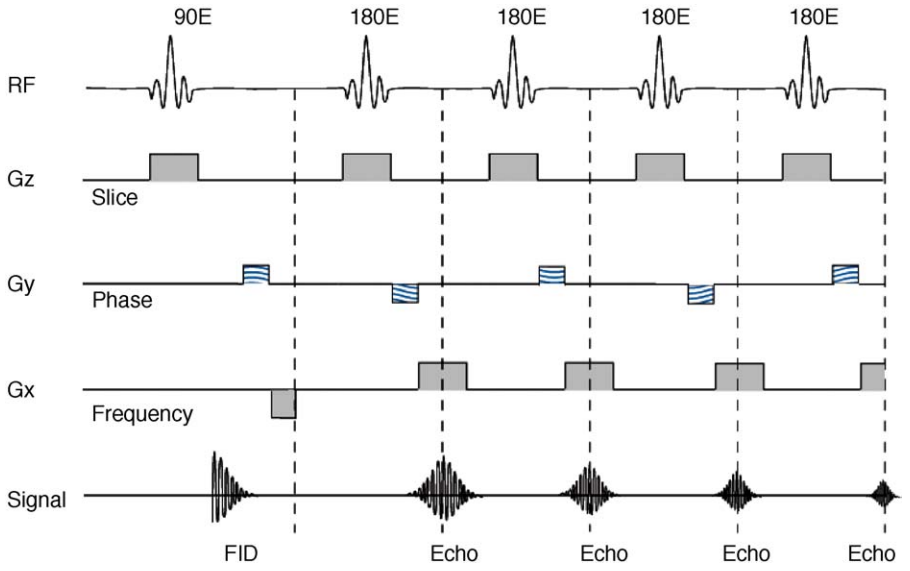

Fig. 70. Fast spin echo pulse sequence diagram. The first part of the sequence is identical to the spin echo sequence. A 90° pulse is given, followed by 180° radiofrequency (RF) refocusing pulse. The difference lies in the fact that multiple 180° RF refocusing pulses are applied, resulting in a stream of echoes after a single excitation pulse. FID, free induction decay.

Because of these limitations, 3D imaging is most suitable in areas in which a small field of view is desirable and multiplanar reconstruction is necessary. These areas include the pituitary gland, the knee and other small joints, and the neuroforamina of the cervical spine.

Fast spin echo technique

Fast spin echo (FSE), or rapid acquisition relaxation enhanced, initially described by Hennig and Friedburg [78] and developed by others [79], is probably the single most important advance in faster imaging within the past decade. FSE is really a hybrid of the multislice SE and echoplanar techniques. Any long TR or long TE pulse sequence (especially with newer and faster gradient technology) has substantial dead time. Rather than acquire one line at a time in a multislice mode, multiple 180° pulses with incremental phase encoding are performed during a single TE (Fig. 70). Instead of acquiring one line of k-space during an echo, four or more lines are acquired. This is shown diagrammatically in Fig. 71. Eight lines of k-space are acquired per single echo within a given repetition cycle, and data from many slices can be obtained during each TR. This makes FSE one of the most efficient available methods for acquiring MRI data. This is especially true for T2W images. Because the TRs are long, many slices can be obtained. The TEs are also long, allowing multiple lines of k-space to be sampled during one TE, more than 100 (ie, single-shot FSE) with some machines. FSE imaging adds another dimension to MRI parameters that can affect image quality and speed (ie, echo train length). In a study by Tien et al [80] of FSE imaging parameters using a 16-kHz bandwidth, an echo train length of 8 and TRs between 3000 and 4000 milliseconds were determined to be optimal.

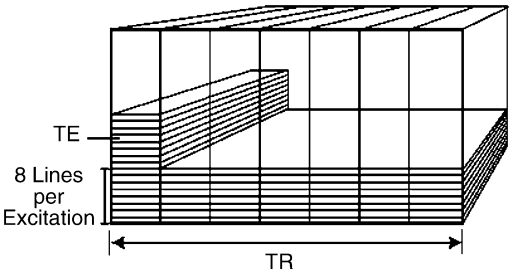

Fig. 71. Fast spin echo multislice acquisition. In this case, multiple lines are obtained using multiple echoes from a single excitation. This vastly increases the acquisition efficiency, particularly on long repetition time (TR) sequences. The k-space can be filled much faster. In this case, eight lines are obtained during each echo. TE, echo time.

FSE can be compared with the revolutionary advance of multislice imaging. Unlike gradient echo images, FSE images are true RF-induced echoes and are much less susceptible to magnetic field inhomogeneities. Because of the dramatic increase in efficiency of image acquisition, multiple averages can be acquired. Alternatively, the number of phase-encoding steps can be increased, yielding much higher resolution images. The bottom line is extremely fast images or superb image quality for an equal amount of time investment compared with conventional SE. FSE imaging can improve the signal-to-noise ratio per unit time by a factor of 8 compared with conventional SE if an echo train length of 16 echoes is used [81]. Looked at another way, the efficiency of signal acquisition is proportional to how much time is devoted purely to reading the signal. In FSE with an echo train length of 33, a calculated efficiency of 50% is obtained. By

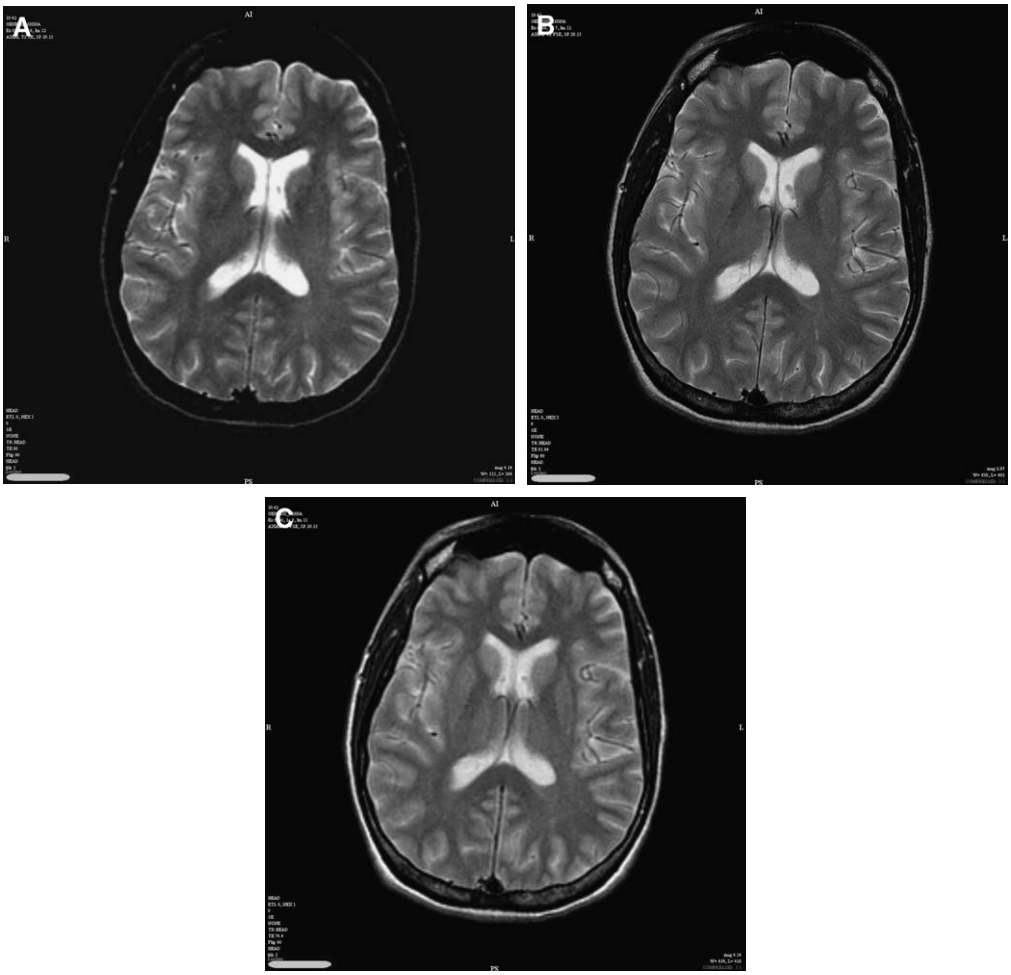

Fig. 72. Comparison of conventional spin echo (SE) and fast spin echo (FSE). (*A*) SE (repetition time [TR] = 3000 milliseconds, echo time [TE] = 80 milliseconds, 5-mm thick slices, 18 images in 7 minutes and 48 seconds, 256 × 192 matrix, number of excitations [NEX] = 1). (*B*) FSE (TR = 3000 milliseconds, effective TE = 84 milliseconds, 5-mm slice thickness, echo train length = 8, 12 images in 7 minutes and 18 seconds, 512 × 512 matrix, NEX = 3). In this case, the imaging time is comparable to that of Fig. 72A. With FSE, however, there is a dramatic improvement in the signal-to-noise ratio and resolution. (*C*) Alternatively, one can use the benefits of FSE to decrease the acquisition time. In this case (TR = 3000 milliseconds, TE = 80 milliseconds, echo train length = 8 milliseconds, 5-mm slice thickness, 256 × 192 matrix, NEX = 1), FSE yielded 18 images in 1 minute. The image quality is comparable to that of the conventional SE image, which required nearly 8 minutes, representing an eight-fold improvement in efficiency.

comparison, SE imaging has approximately 20% efficiency [82]. Thus, FSE imaging not only acquires images faster but acquires more signal per unit time. A series of images comparing a conventional SE sequence and a FSE sequence is shown in Fig. 72. From this series of images, we can see that with FSE images, tradeoffs can be made between image quality and speed [83].

Image contrast in fast spin echo imaging

The central region of k-space corresponding to low frequencies (low gradient strength) is primarily responsible for image contrast. The more peripheral high-frequency components are responsible for edge detail [84]. FSE requires strong gradients, because phase encoding must be performed quickly. Strong gradients dephase signal. The central part of k-space, near the gradient isocenter, receives the least dephasing. Therefore, measurable signal differences between tissues are greatest and produce most of the contrast in the image for echoes sampled near the center of k-space. Whether the center of k-space is sampled early or late determines in part whether an image is T1W or T2W. If the periphery of k-space is sampled first, followed by the central echoes, it is T2W.

T1-weighted fast spin echo

For T1W imaging, the first echoes (ie, those at the beginning of the phase encoding) are used to sample the central k-space to achieve T1W contrast. This has the undesirable effect of

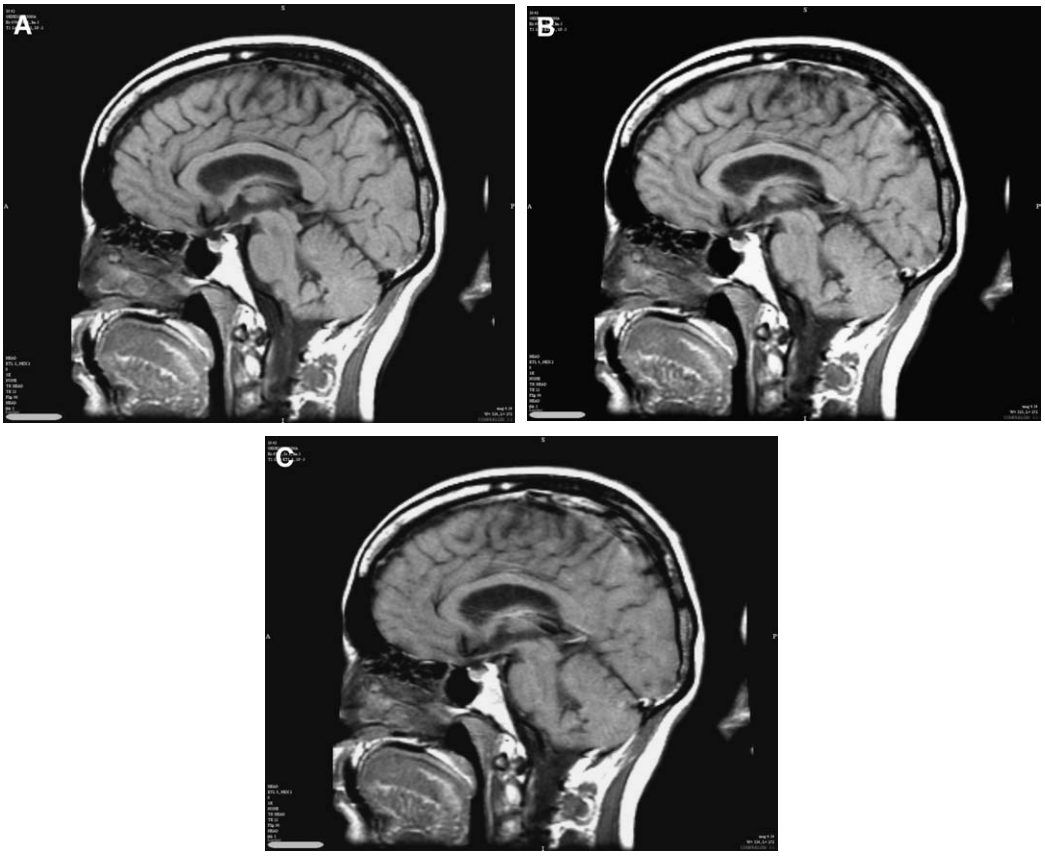

Fig. 73. This is a comparison of T1-weighted fast spin echo (FSE) images showing loss of edge detail with increasing echo train length. A series of FSE (TR = 600 milliseconds, TE = 15eff milliseconds, 5-mm slice thickness, 2.5-mm spacing, 256 × 192 matrix, NEX = 2, 22-cm field of view images). (*A*) Echo train length of 2. (*B*) Echo train length of 4. (*C*) Echo train length of 8. Notice how the gyral detail is obscured with increasing echo train length. The corpus callosum and adjacent cerebrospinal fluid are not as sharply defined. The pons appears fuzzy. The cerebellar folia are not as well delineated.

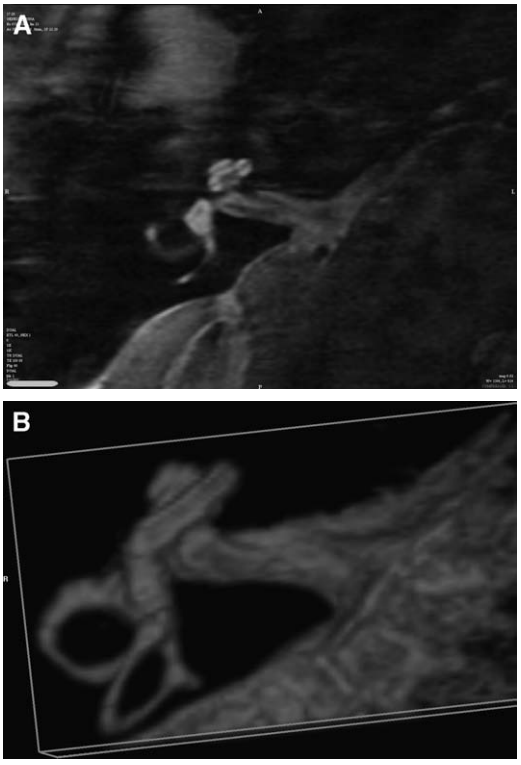

Fig. 74. Axial fast spin echo images through the internal auditory canals and petrous bones (TR = 4400 milliseconds, TE = 109 milliseconds, echo train length = 48 milliseconds, 512 × 256 matrix, three-dimensional [3D] axial 0.8-mm slice thickness). The individual seventh and eighth nerves can be identified in the internal auditory canal. (*A*) Collapsed region reconstruction of the 3D data. (*B*) 3D reconstruction of the 3D FSE data set on a Novarad (American Fork, Utah) workstation.

relegating later echoes to acquire the more peripheral lines of k-space that correspond to high frequencies. These echoes show progressive loss of signal intensity. Therefore, T1W FSE images suffer from loss of edge detail compared with conventional SE images (Fig. 73). Increasing the echo train length causes progressive loss of image sharpness. Furthermore, because the TR of T1W images is relatively short (500–1000 milliseconds), the introduction of multiple additional echo trains prolongs the acquisition time and drastically reduces the number of slices available. For example, an eight–echo train, T1W, FSE pulse sequence requires approximately 160 milliseconds. Only 4 slices can be acquired compared with a conventional SE sequence, in which 35 slices can be acquired. Therefore, FSE imaging is not highly efficient for T1W imaging.

When sampling a longer echo train, there is progressive T2 decay of all tissues in an exponential fashion. Those echoes sampling high-frequency data are performed last and have the lowest intensity and the highest noise. Furthermore, those tissues that have the shortest T2 suffer the most in loss of spatial information. Therefore, areas such as bone interfaces show poor edge detail with adjacent tissues as CSF. The longer the echo train length, the greater signal intensity difference there is between the first and last echoes.

FSE imaging can be acquired in a 3D mode. As such, the edge blurring found on T1W images can be directed out of the image plane and into the *z*-slice select direction by reordering the *x*- and *y*-directions of phase encoding. This technique was used by Weinberger et al [85] to acquire 3D T1W images of the pediatric spine, acquiring 28 images at 1-mm thickness in a period of 8.5 minutes.

T2-weighted fast spin echo

FSE T2W images, conversely, acquire central k-space much later in the echo train. This has the advantage of acquiring the high-frequency data first. Edge clarity and image sharpness seem to be slightly better than with conventional SE imaging. There is an accentuation of T2 contrast because of the late acquisition of image contrast-producing echoes in central k-space. T2W FSE can also be obtained in a 3D mode, which becomes efficient if

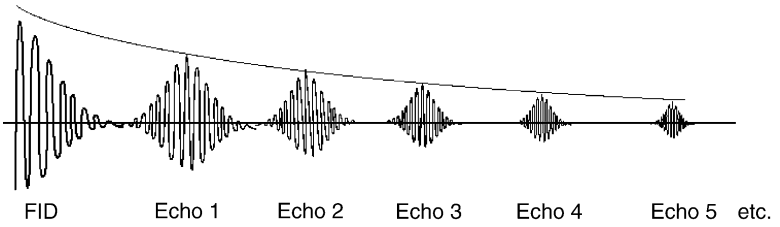

Fig. 75. With each echo, the signal intensity drops. Thus, lines of data acquired at echo 8 suffer degradation and distortion compared with those acquired at echo 1. FID, free induction decay.

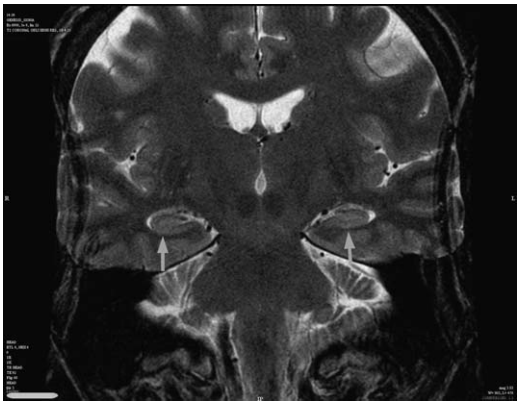

Fig. 76. Fast spin echo (TR = 4000 milliseconds, TE = 92 milliseconds, echo train length = 8, 18-cm × 14-cm field of view, 3-mm slice thickness, 512 × 384 matrix, NEX = 4) images through the temporal lobe allow excellent delineation of the hippocampal formations (*arrows*). This technique is useful for screening of mesiotemporal sclerosis.

a long echo train length is used. Such a sequence is useful for high-resolution images of structures that have long T2, such as the semicircular canals of the inner ear (Fig. 74) [86].

Disadvantages

Nothing is completely free. FSE has a few disadvantages. It is not particularly well suited for T1W images because of the short TEs required for T1 weighting. Traditional T2 contrast as seen on brain imaging is a little different from FSE imaging. To begin with, each of the echoes is not identical. There is gradual loss of signal with the refocusing of each echo (Fig. 75). The more echoes that are attempted for each TE, the more distortion there is between each line. FSE also suffers from a number of artifacts, which include blurring of images with T1W images (see Fig. 71) and edge enhancement artifacts found with T2W images [87]. Furthermore, because more echoes are sampled for each TE, the gradients are driven harder. This, in turn, induces more eddy currents and magnetic field inhomogeneities. With the large number of 180° RF pulses (some of which are off-resonant) and because multislice imaging is being performed, a significant amount of magnetization transfer occurs. Magnetization transfer is the most important reason for signal loss in comparison with SE [88]. FSE imaging can acquire single- or double-echo sequences [89]. The TE is really a false TE time; the TE is determined by when the central phase-encoding data are obtained. Most systems describe this as the TEeff.

Clinical applications

Early results predicted (and these have largely been borne out in practice) that FSE imaging would replace conventional SE imaging for most

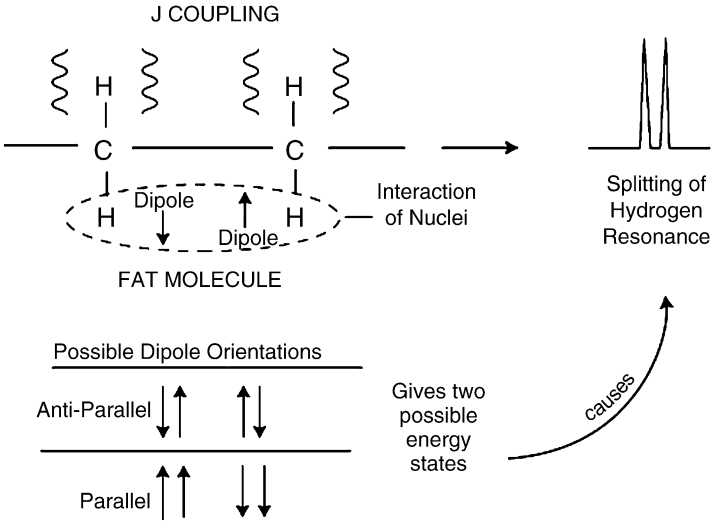

Fig. 77. J coupling. Hydrogen nuclei on adjacent carbon atoms have their own small magnetic field, which interacts with adjacent atoms. As a result of this interaction, the spectrum of the hydrogen nuclei is altered—a phenomenon known as splitting. The dipoles can exist in one of two orientations, parallel or antiparallel. When the dipoles are parallel, they tend to repel each other, altering the magnetic field, and thus altering the resonant frequency of the hydrogen nuclei.

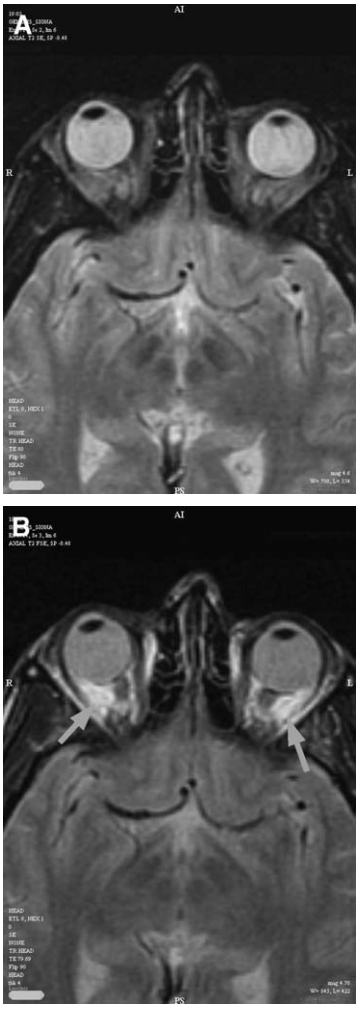

Fig. 78. Comparison of fast spin echo (FSE) and conventional spin echo (SE) for fat brightness. (*A*) Conventional SE (TR = 3000 milliseconds, TE = 80 milliseconds, 5-mm slice thickness, 256 × 192 matrix, NEX = 1) image at the level of the orbits reveals that the intraorbital fat is dark. The scalp fat is also relatively dark. This is secondary to the dephasing that occurs within fat molecules as a result of the J coupling phenomenon. (*B*) FSE (TR = 3000 milliseconds, TE = 80 milliseconds, echo train length = 8 milliseconds, 256 × 192 matrix, NEX = 1) image at the level of the orbits reveals that the intraconal fat of the orbits (*arrows*) and the scalp fat remain bright. The multiple echo train of the FSE sequence helps to average out the micromolecular magnetic perturbations within the fat molecule.

brain [90] and spine imaging [91] for intradural [92] and extradural disease [93] of the spine. Heavily T2W images can be sampled, creating myelographic-like visualization of the spine. Numerous clinical studies comparing the efficacy of FSE with conventional SE have demonstrated it to be comparable or superior in the detection of multiple sclerosis lesions [94], in the evaluation of infarcts [95], for the pelvis [96], and for the evaluation of intracranial neoplasms [97]. The improved resolution is also helpful for evaluation of the temporal lobes (Fig. 76).

Hemorrhagic lesions do not show quite as much susceptibility effect, although lesion conspicuity is similar in actual practice [98]. Additionally, FSE imaging is less sensitive for the diagnosis of meniscal tears compared with conventional SE imaging at comparable image resolution [99]. Susceptibility effects decrease with increasing echo train length, which may account for its lowered sensitivity in these conditions [100].

J coupling

Fat signal also tends to have different characteristics on T2W FSE images from conventional SE images [101–103]. This has been attributed to a phenomenon known as J coupling (Fig. 77). J coupling is commonly found in NMR spectra in which hydrogen nuclei interact with one another across a carbon-carbon or other bond. The net effect is splitting of the resonance of the hydrogen atoms. In essence, this might be thought of as a micromagnetic field perturbation at the molecular level. The exact mechanism remains controversial [104]. On traditional SE images, this local field perturbation causes dephasing of the nuclei and the fat darkens. With FSE imaging, there are multiple repetitive 180° refocusing pulses, often eight or more in a typical sequence, before the central k-space echoes are collected. This repetitive refocusing of the magnetic field tends to mitigate the dephasing ordinarily caused by J coupling, and the fat remains bright (Fig. 78).

Summary

We have come full circle from spinning quarks to 3D medical images. The bulk of MRI is now performed using slice-selective gradients, during which RF energy is applied to excite the hydrogen nuclei. By stepping a phase-encoding gradient during each TR and using a frequency-encoding

gradient as the data are sampled, the 3D human object can be reduced to many individual points or voxels. By acquiring multiple slices at once, the time efficiency of imaging can be vastly improved. Many newer strategies use variations of this technique to acquire multiple lines of data during a single echo, enshrining spin warp imaging as the most important method of signal acquisition for MRI.

References

[1] Purcell EM, Torrey HC, Pound RV. Nuclear induction experiment. Phys Rev 1946;70:474–85.

[2] Bloch F, Hansen WW, Packard M. Resonance absorption by nuclear magnetic moment in a solid. Phys Rev 1946;69:37–8.

[3] Williams WSC. Nuclear and particle physics. Oxford (NY): Oxford University Press; 1991.

[4] Fullerton GD. Basic concepts for nuclear magnetic resonance imaging. Magn Reson Imaging 1982; 1(1):39–53.

[5] Levin I. Nuclear-magnetic-resonance spectroscopy. Phys Chemistry 1978;671–80.

[6] Gordon RE. Magnets, molecules and medicine. Phys Med Biol 1985;30:741–69.

[7] Lerski RA. Principles of nuclear magnetic resonance (NMR)—current state-of-the art. J Med Eng Technol 1985;9(3):112–6.

[8] Pykett SL, Newhouse JH, Buonanno BS, Brady TJ, et al. Principles of nuclear magnetic resonance imaging. Radiology 1982;143:157–68.

[9] Pykett IL. NMR imaging in medicine. Sci Am 1982;246:78–88.

[10] Gore JC, Emery EW, Orr JS, Doyle FH. Medical nuclear magnetic resonance imaging: I. Physical principles. Invest Radiol 1981;18(4):269–74.

[11] Hennel JW, Klinowski J. Fundamentals of nuclear magnetic resonance. Essex: Longman Sci Tech; 1993. p. 61–7.

[12] Dwek RA. Nuclear magnetic resonance (NMR) in biochemistry: applications to enzyme systems. Oxford: Clarendon Press; 1973. p. 15.

[13] Hallick D, Resnick R, et al. Fundamentals of physics. New York: John Wiley & Sons; 1974.

[14] Dwek RA. Relaxation, chemical shifts, spin-spin coupling constants and chemical exchange. NMR Biochem 1973;11–47.

[15] Koenig SH, Brown RD, Spiller M, Lundbom N. Relaxometry of brain: why white matter appears bright in MRI. Magn Reson Med 1990;14:482–95.

[16] Mitchell DG, Burk DL, Vinitski S, Rifkin MD. The biophysical basis of tissue contrast in extracranial MR imaging. AJR Am J Roentgenol 1987;149: 831–7.

[17] Boyko OB, Burger PC, Shelburne D, Ingram P. Non-heme mechanisms for T1 shortening: pathologic, CT and MR elucidation. AJNR Am J Neuroradiol 1992;13(5):1439–45.

[18] Fullerton GD, Cameron IL, Ord VA. Frequency dependence of magnetic resonance spin-lattice relaxation of protons in biological materials. Radiology 1984;151(1):135–8.

[19] Koenig SH, Brown RD, Adams D, Emerson D, Harrison CG. Magnetic field dependence of $1/T_1$ of protons in tissue. Invest Radiol 1984;19:76–81.

[20] Wehrli FW, MacFall JR, Shutts D, Breger R, Herfkens RJ. Mechanisms of contrast in NMR imaging. J Comput Assist Tomogr 1984;8(3):369–80.

[21] Kj?r L, Henriksen O. Comparison of different pulse sequences for in vivo determination of T1 relaxation times in the human brain. Acta Radiol 1988; 29(Fasc 2):231–6.

[22] Young IR. Considerations affecting signal and contrast in NMR imaging. Br Med Bull 1984;40(2): 139–47.

[23] Breger RK, Rimm AA, Fischer ME, Papke RA, Haughton VM. T1 and T2 measurements on a 1.5-T commercial MR imager. Radiology 1989; 171:263–76.

[24] Damadian R. Tumor detection by nuclear magnetic resonance. Science 1971;171:1151–3.

[25] Cameron IL, Ord VA, Fullerton GD. Characterization of proton NMR relaxation times in normal and pathological tissues by correlation with other tissue parameters. Magn Reson Imaging 1984; 2(2):97–106.

[26] LeBas JF, Benabid AL, et al. NMR of brain tumors. J Comput Assist Tomogr 1984;8(6):1048–57.

[27] Jackson JA, Schneiders NJ, Ford JJ, Bryan RN. Improvements in the clinical utility of calculated T_2 images of the human brain. Magn Reson Imaging 1985;3(2):131–43.

[28] Just M, Thelan M. Tissue characterization with T1, T2 and proton density values: results in 160 patients with brain tumors. Radiology 1988;169:779–85.

[29] Hoehn-Berlage M, Tolxdorff T, Bockhorst K, Okada Y, Ernestus R-I. In vivo NMR T_2 relaxation of experimental brain tumors in the cat: a multiparameter tissue characterization. Magn Reson Imaging 1992;10:935–47.

[30] Jackson EF, Ginsberg LE, Schomer DF, Leeds NE. A review of MRI pulse sequences and techniques in neuroimaging. Surg Neurol 1997;47:185–99.

[31] Zimmerman R, Gibby WA, Carmody RF. Neuroimaging, clinical and physical principles. New York (NY): Springer-Verlag; 2000.

[32] Hahn EL. Spin-echoes. Phys Rev 1955;80:580–94.

[33] Wehrli FW, MacFall JR, Glover GH, Grigsby N, et al. The dependence of nuclear magnetic resonance (NMR) image contrast on intrinsic and pulse sequence timing parameters. Magn Reson Imaging 1984;2(1):3–16.

[34] Perman WH, Hilar SK, Simon HE, Maudsley AA. Contrast manipulation in NMR imaging. Magn Reson Imaging 1984;2(1):23–32.

[35] Plewes DB. The AAPM/RSNA physics tutorial for residents: contrast mechanisms in spin-echo MR imaging. Radiographics 1994;14(6):1389–404.
[36] Wehrli FW, Breger RK, MacFall JR, Daniels DL, et al. Quantification of contrast in clinical MR brain imaging at high magnetic field: original investigations. Invest Radiol 1985;20(4):360–9.
[37] Nelson TR, Hendrick RE, Hendee WR. Selection of pulse sequences producing maximum tissue contrast in magnetic resonance imaging. Magn Reson Imaging 1984;2(4):285–94.
[38] Carr HY, Purcell EM. Effects of diffusion on free precession in nuclear magnetic resonance experiments. Phys Rev 1954;94:630–8.
[39] Meiboom S, Gill D. Carr-Purcell-Meiboom-Gill sequence (CPMG). Rev Sci Instrum 1959;29:688–91.
[40] Bydder GM, Young IR. MR imaging: clinical use of the inversion recovery sequence. J Comput Assist Tomogr 1985;9(4):659–75.
[41] Wehrli FW, MacFall JR, Shutts D, et al. Mechanisms of contrast in NMR imaging. J Comput Assist Tomogr 1984;8(3):369–80.
[42] Edelstein WA, Bottomley PA, Hart HR, Smith LS. Signal, noise and contrast in nuclear magnetic resonance (NMR) imaging. J Comput Assist Tomogr 1983;7(3):391–401.
[43] Moran PR, Kumar NG, Karstaedt N, Jackels SC. Tissue contrast enhancement: image reconstruction algorithm and selection of TI in inversion recovery MRI. Magn Reson Imaging 1986;4:229–35.
[44] Huk W, Heindel W, Deimling M, Stetter E. Nuclear magnetic resonance (NMR) tomography of the central nervous system: comparison of two imaging sequences. J Comput Assist Tomogr 1983;7(3): 468–75.
[45] Atlas SW, Grossman RI, Hackney DB, Goldberg HI, Bilaniuk LT, Zimmerman RA. STIR MR imaging of the orbit. AJNR Am J Neuroradiol 1988;9:969–74.
[46] Takehara S, Tanaka T, Uemura K, Shinora Y, et al. Optic nerve injury demonstrated by MRI with STIR sequences. Neuroradiology 1994;36: 512–4.
[47] Johnson G, Miller DH, MacManus D, Tofts PS, et al. STIR sequences in NMR imaging of the optic nerve. Neuroradiology 1987;29(13):238–45.
[48] Tien RD. Fat suppression MR imaging and neuroradiology: techniques and clinical application. AJR Am J Roentgenol 1992;158(2):369–79.
[49] Krinsky G, Rofsky NM, Weinreb JC. Non-specificity of short inversion time inversion recovery (STIR) as a technique of fat suppression: pitfalls in image interpretation. AJR Am J Roentgenol 1996;166:523–6.
[50] Hittmair K, Mallek R, Prayer D, Schindler EG, Kollegger H. Spinal cord lesions in patients with multiple sclerosis: comparison of MR pulse sequences. AJNR Am J Neuroradiol 1996;17:1555–65.
[51] Rydberg JN. Fast FLAIR. Radiology 1993;193: 173–80.
[52] Rydberg JN. FLAIR. Magn Reson Med 1995;34: 868–77.
[53] Alexander JA, Sheppard S, Davis PC, Salverda P. Adult cerebrovascular disease: role of modified rapid fluid-attenuated inversion-recovery sequences. AJNR Am J Neuroradiol 1996;17:1507–13.
[54] Filippi M, Yousry T, Baratti C, Hounsfield HA, et al. Quantitative assessment of MRI lesion load in multiple sclerosis: a comparison of conventional spin-echo with fast fluid-attenuated inversion recovery. Brain 1996;119:1349–55.
[55] Hajnal JV, Bryant DJ, Kasuboski L, Pattany PM, et al. Use of fluid attenuated inversion recovery (FLAIR) pulse sequences in MRI of the brain. J Comput Assist Tomogr 1992;16(6):841–4.
[56] Murata T, Itoh S, Koshino Y, Sakamoto K, et al. Serial cerebral MRI with FLAIR sequences in acute carbon monoxide poisoning. J Comput Assist Tomogr 1995;19(4):631–4.
[57] DeCoene B. MR of brain FLAIR. AJNR Am J Neuroradiol 1992;13:1555–64.
[58] Araki Y, Ashikaga R, Takahashi S, Ueda J, Ishida O. High signal intensity of the infundibular stalk on fluid-attenuated inversion recovery MR. AJNR Am J Neuroradiol 1997;18:89–93.
[59] Brant-Zawadzki M, Atkinson D, Detrick M, Bradley WG, Scidmore G. Fluid-attenuated inversion recovery (FLAIR) for assessment of cerebral infarction: initial clinical experience in 50 patients. Stroke 1996;27(7):1187–91.
[60] Rosen BR, Wedeen VJ, Brady TJ. Selective saturation NMR. J Comput Assist Tomogr 1984;8(5): 813–8.
[61] Simon JH, Szumowski J. Proton (fat/water) chemical shift imaging in medical magnetic resonance imaging. Current status. Invest Radiol 1992; 27(10):865–73.
[62] Mills TC, Ortendahl DA, Hylton NM, Crooks LE, Carlson JW, Kaufman L. Partial flip angle MR imaging. Radiology 1987;162:531–9.
[63] Lauterbur PC. Image formation by induced local interactions; examples employing nuclear magnetic resonance. Nature 1973;242:190–1.
[64] Hinshaw WS, Andre ER, Bottomley PA, et al. NMR images by the multiple sensitive point method; application to larger biological systems. Phys Med Biol 1977;22(5):971–4.
[65] Damadian R, Minkoff I, Goldsmith M. NMR in cancer XXI. FONAR scan of the live human abdomen. Physiol Chem Phys 1978;10(6):561–3.
[66] Pykett IL. NMR imaging in medicine. Sci Am 1982;246(5):78–88.
[67] Hinshaw WS, Bottomley PA, Holland GN. A demonstration of the resolution of NMR imaging in biological systems. Experentia 1979;35(a): 1268–76.

[68] Crooks L, Hoenninger J, Arakawa M, et al. Tomography of hydrogen with nuclear magnetic resonance. Radiology 1980;136:701–6.
[69] Mansfield P, Maudsley AA. Medical imaging by NMR. Br J Radiol 1977;50(591):188–94.
[70] Kumar A, Welti D, Ernst RR. NMR Fourier zeugmatography. J Magn Reson Imaging 1975;18: 69–83.
[71] Lauterbur PC, Lai C-M. IEEE Trans Nucl Sci 1980;27:1227–31.
[72] den Boef JH, van Uijen CMJ, Holzcherer CD. Multiple-slice NMR imaging by three-dimensional Fourier zeugmatography. Phys Med Biol 1984; 29(7):857–67.
[73] Edelstein WA, Hutchison JMS, Johnson G, Redpath T. Spin warp NMR imaging and applications to human whole-body imaging [letter to the editor]. Phys Med Biol 1980;25:751–6.
[74] Hinshaw WS, Andrew ER, Bottomley PA, Holland GN, et al. An in vivo study of the forearm and hand by thin section NMR imaging. Br J Radiol 1979;52:36–43.
[75] Bottomley PA, Andrew ER. RF magnetic field penetration, phase shift and power dissipation in biological tissue: implications of NMR imaging. Phys Med Biol 1978;23(4):630–43.
[76] Kramer DM, Guzman RJ, Carlson JW, Crooks LE, Kaufman L. Physics of thin-section MR imaging at low field strength. Radiology 1989; 173(2):541–4.
[77] Jezzard P, Duewell S, Balaban RA. MR relaxation times in human brain: measurement at 4 T1. Radiology 1996;199:773–9.
[78] Hennig J, Friedburg H. RARE imaging: a fast imaging method for clinical MR. Magn Reson Med 1986;3(6):823–33.
[79] Jolesz FA. Fast spin-echo technique extends versatility of MR. Diagn Imaging 1992;14:78–86.
[80] Tien RD, Felsberg GJ, MacFall J. Practical choices of fast spin-echo pulse sequence parameters: clinically useful proton density and T2-weighted contrasts. Neuroradiology 1992;35:38–41.
[81] Constable RT, Smith RC, Gore JC. Signal-to-noise and contrast in fast spin-echo (FSE) and inversion recovery FSE imaging. J Comput Assist Tomogr 1992;16(1):41–7.
[82] Feinberg DA, Keifer B, Litt AW. High resolution GRASE MRI of the brain and spine: 512 and 1024 matrix imaging. J Comput Assist Tomogr 1995;19(1):1–7.
[83] Melki PS, Mulkern RV, Panych LP, Joesz FA. Comparing the FAISE method with conventional dual-echo sequences. J Magn Reson Imaging 1991; 1(3):319–26.
[84] Choen MS, Weisskoff RM. Ultra-fast imaging. Magn Reson Imaging 1991;9(1):1–37.
[85] Weinberger E, Murakami JW, Shaw DW, et al. Three dimensional fast spin-echo T1 weighted imaging of the pediatric spine. J Comput Assist Tomogr 1995;19(5):721–5.
[86] Tien RD, Felsberg GJ, MacFall J. Fast spin-echo high resolution MR imaging of the inner ear. AJR Am J Roentgenol 1992;159:395–8.
[87] Melki PS, Jolesz FA, Mulkern RV. Partial RF echo-planar imaging with the FAISE method. I. Experimental and theoretical assessment of artifact. Magn Reson Med 1992;26:328–41.
[88] Constable RT, Anderson AW, Zhong J, Gore JC. Factors influencing contrast and fast spin echo MR imaging. Magn Reson Imaging 1992;10: 497–511.
[89] Noll DC. Variable averaging RARe. Magn Reson Med 1994;31:323–7.
[90] Norbash AM, Glover GH, Enzmann DR. Intracerebral legion contrast with spin echo and fast spin-echo pulse sequences. Radiology 1992;185(3): 661–5.
[91] Jones KM, Mulkern RV, Schwartz RB, et al. Fast spin-echo MR imaging of the brain and spine: current concepts. AJR Am J Roentgenol 1992;158: 1313–20.
[92] Sze G, Merriam M, Oshio K, Jolesz FA. Fast spin-echo imaging in the evaluation of intradural disease of the spine. AJNR Am J Neuroradiol 1992;13: 1383–92.
[93] Chappell PM, Glover GH, Enzmann DR. Contrast on T2-weighted images of the lumbar spine using fast spin-echo and gated conventional spin-echo sequences. Neuroradiology 1995;37:183–6.
[94] Thorpe JW, Halpin SF, MacManus DG, et al. A comparison between fast and conventional spin-echo in the detection of multiple sclerosis lesions. Neurology 1994;36(5):388–92.
[95] Susuki T, Kakiuchi H, Sugiki S, et al. Detection of cortical infarcts in brain MR imaging; feasibility of short-TR-T2-weighted imaging using a fast spin-echo sequence. Nippon Igaku Hoshasen Gakkai Zasshi 1995;55(4):260–2.
[96] Smith RC, Reinhold C, Lange RC, et al. Fast spin-echo MR imaging of the female pelvis. Part I. Use of a whole volume coil. Radiology 1992; 184:665–9.
[97] Tice HM, Jones KM, Mulkern RV, et al. Fast spin-echo imaging of intracranial neoplasms. J Comput Assist Tomogr 1993;17(3):425–31.
[98] Jones KM, Mulkern RV, Mantello MT, et al. Brain hemorrhage: evaluation with fast spin-echo images. Radiology 1992;182(1):53–8.
[99] Rubin DA, Kneeland JB, Listerud, et al. MR diagnosis of meniscal tears of the knee: value of fat spin-echo vs. conventional spin-echo pulse sequences. AJR Am J Roentgenol 1994;162:1131–5.
[100] Reimer P, Allkemper T, Schuierer G, Peters PE. Brain imaging: reduced sensitivity of RARE-derived techniques to susceptibility effects. J Comput Assist Tomogr 1996;20(2):201–5.

[101] Nghiem HV, Herfkens RJ, Franscis IR, et al. The pelvis: T2-weighted fast spin-echo MR imaging. Radiology 1992;185(1):213–7.
[102] Wright G.A. Lipid signal enhancement in spin echo trains. In: Proceedings of the Mtg Soc Magn Reson. 1992. p. 437.
[103] Henkelman RM, Hardy PA, Bishop JE, et al. Why fat is bright in RARE and fast spin-echo imaging. J Magn Reson Imaging 1992;2:533–40.
[104] Williamson DS, Mulkern RV, Jakab PD, Josesz FA. Coherence transfer by isotropic mixing in Carr-Purcell-Meiboom-Gill imaging: implications for the bright fat phenomenon in fast spin-echo imaging. Magn Reson Med 1996;35:506–13.
[105] Ling CR, Foster MA, Hutchison JMS. Comparison of NMR water proton T1 relaxation times of rabbit tissues at 24 mHZ and 2.5 mHZ. Phys Med Biol 1980;25:748–51.
[106] Bottomley PA, Foster TH, Argersinger RE, Pfeifer LM. A review of normal tissue hydrogen NMR relaxation times and relaxation mechanisms from 1–100 MHz: dependence on tissue type, NMR frequency, temperature, species, excision and age. Med Physic 1984;11(4):425–48.
[107] Hopkins AL, Yeung HN, Barton CB. Multiple field strength in vivo T1 and T2 for cerebrospinal fluid protons. Magn Reson Med 1986;3: 303–11.